

CMS Draft Analysis Note

The content of this note is intended for CMS internal use and distribution only

2020/05/31

Archive Hash: f310227

Archive Date: 2020/05/31

Fragmentation of jets into J/ψ mesons in PbPb and pp collisions

Batoul Diab¹, Guillaume Falmagne¹, Inna Kucher¹, Matthew Nguyen¹, and Lizardo Valencia Palomo²

¹ Laboratoire Leprince-Ringuet, Centre National de la Recherche Scientifique

² Universidad de Sonora

Abstract

This note describes a measurement of prompt J/ψ mesons in jets, looking at the distribution of z , the fraction of the jet momentum taken by the J/ψ . Prompt J/ψ are separated from the nonprompt background via bidimensional fits to the invariant mass and lifetime distributions. Jets are studied in the range of p_T of 30 – 40 GeV, and within $|\eta| < 2$. The data are unfolded to correct the effect of the jet p_T resolution, as a function of both jet p_T and z . The differential yield with respect to z is compared between PbPb and pp data. The analysis uses pp data recorded in 2017 and PbPb data recorded in 2018, both at $\sqrt{s_{NN}} = 5.02$ TeV.

This box is only visible in draft mode. Please make sure the values below make sense.

PDFAuthor: Batoul Diab, Guillaume Falmagne, Inna Kucher, Matthew Nguyen, Lizardo Valencia Palomo
PDFTitle: J/ψ in jets in PbPb collisions
PDFSubject: CMS
PDFKeywords: CMS, PbPb, J/ψ , Jets

Please also verify that the abstract does not use any user defined symbols

1 Contents

2	1	Introduction	2
3	2	Analysis Workflow	4
4	3	Selection	6
5	3.1	Location of the code, and data and MC samples	6
6	3.2	Event selection	6
7	3.3	Single muon kinematic cuts	6
8	3.4	Muon identification	7
9	3.5	Jet clustering and selections	7
10	4	J/ ψ signal extraction	8
11	4.1	Invariant mass parameterisation	9
12	4.2	Pseudo-proper decay length parameterisation	12
13	4.3	Bidimensional fitting of invariant mass and pseudo-proper decay length	17
14	5	Acceptance and Efficiency	21
15	6	Jet energy corrections and resolution	25
16	6.1	Jet energy corrections	25
17	6.2	Jet energy resolution	29
18	7	J/ ψ signal extraction systematic uncertainties	32
19	7.1	Invariant mass parameterisation uncertainty	32
20	7.2	Pseudo-proper decay length parameterisation uncertainty	39
21	7.3	Summary of signal extraction systematics	42
22	7.4	Acceptance times efficiency uncertainty	43
23	7.5	Summary plots of systematic uncertainties on bidimensional fits	45
24	8	Raw quarkonia yields	46
25	8.1	Raw prompt J/ ψ yields	46
26	8.2	unfolding input	47
27	9	Unfolding bin migration effects	50
28	10	Jet-related uncertainties	62
29	11	Summary of systematic uncertainties	66
30	12	Results	68
31	A	Determination of the invariant mass parameters from MC	71
32	A.1	Background subtraction from MC samples	71
33	A.2	Tail parameters study of the two components of the double Crystal Ball .	72
34	A.3	Choice of the Chebychev polynomial order for the background model: LLR tests	74
35	B	The 2D fit projections in all analysis bins	79

37 1 Introduction

38 Dissociation of the quarkonia states in AA collisions is one of the best-studied signatures of
39 quark-gluon plasma (QGP) formation. Although other nuclear effects have been identified, it
40 is widely believed that at least part of the suppression of the various quarkonia states in central
41 PbPb collisions at LHC energies is indeed coming from Debye screening of heavy quark pairs
42 in the QGP, as envisioned by Matsui and Satz [1]. This picture is most conveniently probed
43 with quarkonia produced essentially at rest. With the emergence of competing mechanisms,
44 however, it becomes interesting to study the momentum dependence of the nuclear suppres-
45 sion. This is true in particular for regeneration [2], which is thought to explain the relatively
46 modest low p_T suppression factor observed at RHIC [3, 4] and the LHC compared to lower
47 energy collisions at the CERN-SPS [5]. Independent of these nuclear modifications, the inter-
48 pretation of quarkonia results, and heavy flavor results in general, typically is based on the
49 assumption that quarkonia (or at least a pre-resonant state) are formed at early time compared
50 to the formation time of the QGP (order 1 fm/c).

51 This being said, the formation time estimate of quarkonia is based on rather general arguments,
52 rather than on a detailed calculation. Despite its discovery nearly half a century ago, theoretical
53 models generally are not able to describe the entirety of the quarkonia data. In particular, they
54 are not able to simultaneously describe both the p_T -differential cross of quarkonia and its polar-
55 ization. The situation evolved recently with a study by the LHCb Collaboration, which looked
56 at the near-angle hadroproduction associated to J/ψ in pp collisions [6]. The observable is the
57 z distribution, sometimes referred to as the jet fragmentation function, of the J/ψ compared
58 to the jet into which it is clustered. For jets in their kinematic range (forward and fairly low
59 p_T), they observe that prompt J/ψ are far jettier than predicted by models. Models of J/ψ pro-
60 duction typically couple fixed order pQCD calculations with non-perturbative matrix elements
61 that describe hadronization of the charm quark pair to a color neutral state. A solution to this
62 discrepancy was proposed by Bain et al [7], who evolve the parton shower via DGLAP evolu-
63 tion prior to the formation of the J/ψ . By including this parton shower contribution, which is
64 not described in hadronization generators such as PYTHIA, the authors were able to successfully
65 describe the data.

66 Assuming this explanation of the LHCb data is correct, this paradigm shift in our understand-
67 ing of J/ψ production has important implications for the interpretation of J/ψ data in AA col-
68 lisions. It implies that J/ψ are not exclusively produced at short times, but may also be produced
69 in the course of the interaction of a hard scattered parton with the QGP. Hence the nuclear
70 modification may be sensitive to parton energy loss, the same phenomenon that gives rise to
71 jet quenching. We already have some hints in this direction. First, as observed in Ref. [8], the
72 nuclear modification factor of J/ψ in PbPb collisions [9], although statistically limited, appears
73 to exhibit the same rise with p_T as light hadrons show [10], which for the case of light hadrons
74 is well-described by parton energy loss models. Second, the J/ψ shows a significant v_2 value in
75 mid-central collisions at large p_T [11], where the flow effects of the bulk are expected to die out.
76 We know of no other explanation for this high $p_T v_2$ other than path-length dependent parton
77 energy loss.

78 Our investigations began in HIN-18-012 where we reproduced the LHCb measurement, but for
79 pp collisions at mid-rapidity instead of forward rapidity. We observed the same effect, namely
80 that J/ψ are jettier than predicted by generators such as PYTHIA. The goal of the current study
81 is investigate the nuclear modification of J/ψ jets by comparing PbPb to pp. For the first time
82 we will study the modification of J/ψ inside jets, by requiring that the J/ψ is a constituent of
83 a jet in the range $30 < p_T < 40$ GeV. J/ψ candidates are used directly as constituents within

84 the jet clustering algorithm (anti- k_T with $R=0.3$), replacing their decay muons. Jets are required
85 to be with $\eta < 2$, with no explicit requirement on the J/ψ pseudorapidity. Over the full η
86 range, we are able to measure J/ψ down to a p_T of 6.5 GeV. This gives a range of z of about
87 0.2 – 1. We investigate to what extent the nuclear modification varies with z , and, indirectly,
88 the formation time of the J/ψ . These data potentially constrain the roles of the different QGP
89 interaction mechanisms potentially at play, namely parton energy loss and Debye screening.

DRAFT

90 2 Analysis Workflow

91 In this section we describe the general strategy used in the analysis in order to study the distri-
 92 butions of prompt and nonprompt J/ψ mesons as a function of z .

93 The analysis workflow is summarised in the schema in Fig. 1.

94 The jets are originally reconstructed by running the anti- k_t algorithm ($R=0.3$) using the stable particles provided by particle flow. Particularly at lower values of $J/\psi p_T$, however, the two decay muons tend to have an opening angle with is comparable to the size of the jet. As a consequence, the J/ψ may be reconstructed in more than one jet. To rectify this we recluster the jets, replacing the decay muons with the J/ψ candidate, after applying the full J/ψ analysis selection. The analogous procedure is applied at generator level to recluster generator-level jets. The underlying event is subtracted using the so-called constituent subtraction method (C_s) [12]. To avoid the unphysical case of $z > 1$, no energy is subtracted from the J/ψ itself, which we define as coming from the primary hard-scattering. Rather the subtracted energy is distributed amongst the other particles in the jet, which may originate from other nucleon-nucleon scatterings.

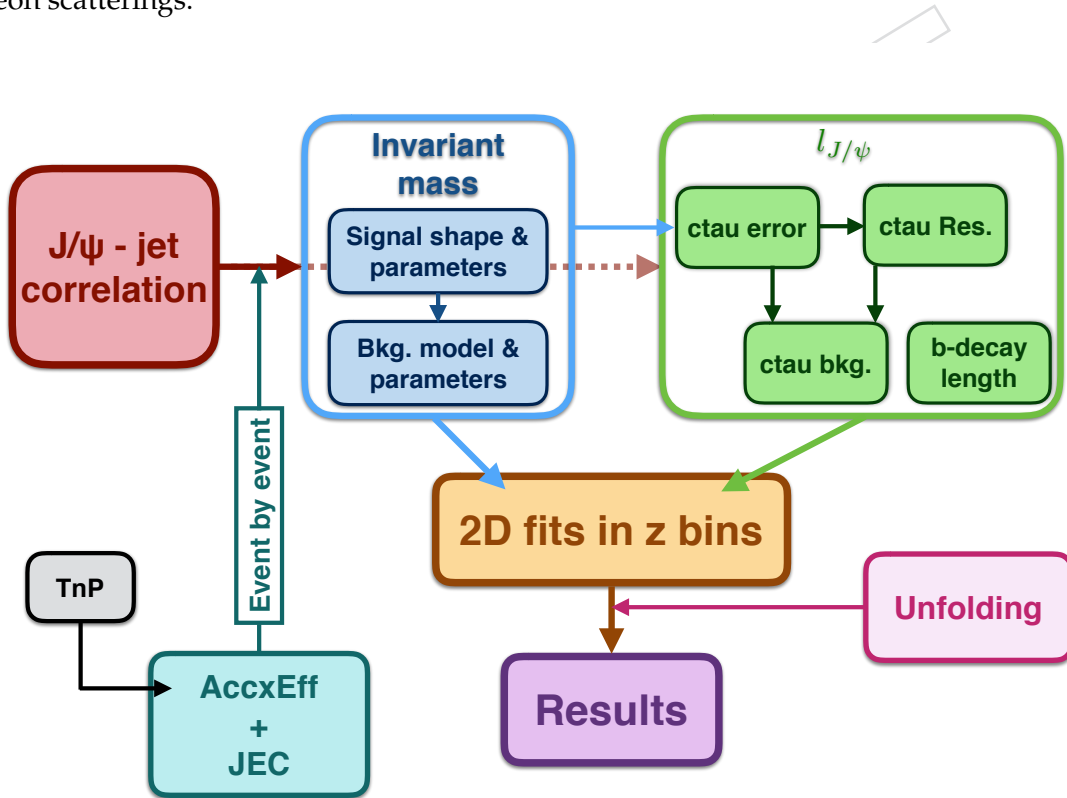


Figure 1: The different steps of the analysis

105 For all the events that pass our selections, we apply the acceptance and efficiency corrections
 106 described in Section 5 and the jet energy corrections described in Section 6.

107 The next step is to use two-dimensional fitting of the dimuon ($\mu^+ \mu^-$) invariant mass and
 108 pseudo-proper decay length distributions to get the yields of prompt and nonprompt J/ψ . This
 109 is done in the same way as HIN-16-025 analysis [9]. The fitting is done in multiple steps. First,
 110 we fit the invariant mass distributions in MC simulations then we use the results to fix certain
 111 parameters when fitting in data. Then comes the pseudo-proper decay length part, where we

112 have four contributions: the $\ell_{J/\psi}$ error distributions, the lifetime resolution, the b hadron decay
113 length and the $\ell_{J/\psi}$ distributions of the the background dimuons. The 2D fits are the final step
114 on the prompt/nonprompt yield extraction. We use as input the parametrisation of the invari-
115 ant mass and pseudo-proper decay length distributions obtained in the previous steps. This is
116 described in section on signal extraction (Section 4).

117 Before obtaining the final results we apply an unfolding procedure to correct for bin migration,
118 due to the finite jet p_T resolution. This procedure is carried out in two dimensions, jet p_T and z ,
119 and is described in Section 9.

120 The results are extracted as a function of z over the entire rapidity coverage of the CMS detector
121 ($|y| < 2.4$ for the J/ψ and $|\eta| < 2$ for the jet). The nominal jet p_T range of the measurement is 30
122 – 40 GeV, although jets in lower and higher p_T ranges are measured as input into the unfolding,
123 as discussed in Section 9.



124 3 Selection

125 3.1 Location of the code, and data and MC samples

126 The analysis code is available in a git repository: <https://github.com/batoul-d/JpsiInJetsPbPb>.
 127 Some documentation on the fitter code is provided in <https://twiki.cern.ch/twiki/bin/view/CMS/HiCharm2015Fitter>. The analysis twiki page is <https://twiki.cern.ch/twiki/bin/view/CMS/JPsiJetsPbPb5TeV>.

130 This analysis uses PbPb and pp data taken at $\sqrt{s_{\text{NN}}} = 5.02 \text{ TeV}$ in 2018 and 2017, respectively.
 131 For pp collisions we used the DoubleMu primary dataset, requiring the HIL1DoubleMu0 trigger,
 132 which was unprescaled both at L1 and HLT throughout the run. In PbPb collisions the we
 133 used a more elaborate trigger with the name HLT_HIL3Mu0NHitQ10_L2Mu0_MAXdR3p5_M1to5,
 134 which was streamed to the DoubleMuon primary dataset for the first part of the run, and sub-
 135 sequently redirected to the PsiPeri primary dataset. The trigger was only prescaled for a short
 136 period towards the beginning of the run, resulting in a reduction of around 5% in the integrated
 137 luminosity compared to an unprescaled trigger.

138 The integrated luminosities corresponding to the data samples used in this analysis are given
 139 in Table 1. In all cases the golden json file was used.

Table 1: Integrated luminosity of the datasets used in this analysis.

System	Primary dataset	Trigger	Luminosity
pp	DoubleMu0	HLT_HIL1DoubleMu0_v1	311 pb^{-1}
PbPb	DoubleMu	HLT_HIL3Mu0NHitQ10_L2Mu0_MAXdR3p5_M1to5	0.53 nb^{-1}
PbPb	PsiPeri	HLT_HIL3Mu0NHitQ10_L2Mu0_MAXdR3p5_M1to5	1.11 nb^{-1}

140 All MC samples used for this analysis were centrally produced (official samples). We use sam-
 141 ples for prompt and nonprompt J/ψ mesons, for both pp and PbPb collisions. They were all
 142 produced using PYTHIA 8.212 [13]. A \hat{p}_T bias was used to sample events more evenly out to
 143 large p_T , which is then corrected for a weight factor. In PbPb collisions, the underlying event is
 144 produced with HYDJET (Drum tune).

145 3.2 Event selection

146 Events from pp data are required to fire the HLT_HIL1DoubleMu0_v1 trigger. This trigger
 147 requires a bunch crossing in coincidence with two muons reconstructed in the muon detectors
 148 with no p_T requirement. The dimuons used in the analysis are required to be matched (by
 149 filter) to the primitives of this trigger. Besides, events are required to pass the official HIN PAG
 150 offline selection, as defined in AN-15-080 [14].

151 These cuts include loose cuts on the primary vertex position and quality for both pp and PbPb,
 152 a scraping filter for pp, and a coincidence filter with the Hadron Forward (HF) calorimeter and
 153 a cluster compatibility filter for PbPb.

154 3.3 Single muon kinematic cuts

155 The single muon acceptance cuts were revised for the 2018 PbPb data, and are documented in
 156 AN-18-036 [15]. For convenience we reproduce these selections here:

$$\begin{aligned}
 p_T^\mu &> 3.5 \text{ GeV}/c & \text{for } |\eta^\mu| < 1.2 \\
 p_T^\mu &> (5.47 - 1.89 \times |\eta^\mu|) \text{ GeV}/c & \text{for } 1.2 \leq |\eta^\mu| < 2.1 \\
 p_T^\mu &> 1.5 \text{ GeV}/c & \text{for } 2.1 \leq |\eta^\mu| < 2.4
 \end{aligned} \tag{1}$$

157 3.4 Muon identification

158 This analysis uses hybrid-soft muon ID cuts, as first documented in AN-16-048 [16], and up-
 159 dated in Ref. [15]. They differ from the standard "soft" muon ID cuts proposed by the muon
 160 POG in two ingredients: added `isGlobalMuon` and removed the `highPurity` condition on
 161 the inner track, as well as the `TMOnStationTight` condition.

162 Hence these cuts are the following:

- 163 • `isTrackerMuon && isGlobalMuon`
- 164 • `nPixWMea>0` (at least one pixel layer with hits),
- 165 • `nTrkWMea>5` (at least 6 inner tracker layers with hits),
- 166 • `dxy<0.3` (absolute distance from the muon to the primary vertex in the transverse
 167 plane smaller than 0.3 cm),
- 168 • `abs(dz)<20` (absolute distance from the muon to the primary vertex in the longi-
 169 tudinal plane smaller than 20 cm),
- 170 • dimuon vertex χ^2 probability > 0.01 .

171 3.5 Jet clustering and selections

172 Jets are clustered from particle flow candidates using the anti- k_T algorithm with an radius pa-
 173 rameter of $R = 0.3$. Selected pairs of muons whose invariant mass is the J/ψ region ($2.6 <$
 174 $m_{\mu^+\mu^-} < 3.5 \text{ GeV}$) are removed from the list of particle candidates and replaced by the recon-
 175 structed J/ψ candidate. We selecton jets in the range $\eta < 2$, in order to require that they are
 176 fully contained in the tracker region. No explicit selection is applied on the J/ψ rapidity. The
 177 jet measurement is performed for the range $30 < p_T < 40 \text{ GeV}$. In order to capture bin migra-
 178 tion effects, we measure jets in a large range of $10 < p_T < 50 \text{ GeV}$, as input to the unfolding.
 179 The wider p_T selection is found to be around 99% efficient for jets in the nominal p_T range in
 180 simulation, for both the prompt and nonprompt J/ψ samples.

181 Jet energy and resolution corrections are discussed in Section 6.1. In PbPb events, we use the
 182 constituent subtraction (Cs) method to subtract the contribution from the underlying event [12].
 183 The jet corrections and underlying subtraction are only applied to the non- J/ψ part of the jet.

184 4 J/ψ signal extraction

185 In this section we describe the main steps to extract the number of prompt and non-prompt J/ψ
 186 mesons in the different analysis bins, similarly to what was done in previous analyses [17, 18].

187 The J/ψ mesons coming from b hadron decays are identified by the measurement of a sec-
 188 ondary $\mu^+ \mu^-$ vertex displaced from the primary collision vertex. The most probable transverse
 189 b hadron decay length in the laboratory frame is calculated as:

$$L_{xyz} = \frac{\hat{u}^T S^{-1} \vec{r}}{\hat{u}^T S^{-1} \hat{u}} , \quad (2)$$

190 where \hat{u} is the unit vector in the direction of the J/ψ meson momentum p , \vec{r} is the displacement
 191 vector between the $\mu^+ \mu^-$ vertex and the primary vertex and S^{-1} is the inverse of the sum of the
 192 primary and secondary vertex covariance matrices. From this, the pseudo-proper decay length
 193 ($\ell_{\text{J}/\psi} = L_{xyz} m_{\text{J}/\psi} / p$) is computed as an estimate of the b hadron decay length. The pseudo-
 194 proper decay length is measured with a resolution of 35 μm .

195 The signal extraction procedure is based on a two-dimensional extended unbinned maximum
 196 likelihood fitting (2D fits) of the dimuon ($\mu^+ \mu^-$) invariant mass and pseudo-proper decay
 197 length distributions for each analysis bin. In these fits the fraction of nonprompt J/ψ mesons
 198 (the so called *b fraction*) is a free fit parameter. The 2D fits are the final step on the prompt/nonprompt
 199 signal extraction. The 2D fitting procedure has as input the parameterisations of the different
 200 components of the invariant mass and pseudo-proper decay length distributions, which are
 201 obtained in previous steps. Some of these input parameterisations are fixed in the 2D fits and
 202 others are only used for initialisation.

203 The expression for the total Probability Density Function (PDF) $F(\ell_{\text{J}/\psi}, m_{\mu\mu})$, the functional
 204 form used for the 2D fit, without per-event errors (i.e. the uncertainty on the pseudo-proper
 205 decay length, as determined event by event from the covariance matrices of the primary and
 206 secondary vertex), is given by:

$$F(\ell_{\text{J}/\psi}, m_{\mu\mu}) = N_{\text{Sig}} \cdot F_{\text{Sig}}(\ell_{\text{J}/\psi}) \cdot M_{\text{Sig}}(m_{\mu\mu}) + N_{\text{Bkg}} \cdot F_{\text{Bkg}}(\ell_{\text{J}/\psi}) \cdot M_{\text{Bkg}}(m_{\mu\mu}) , \quad (3)$$

207 where:

- 208 1. N_{Sig} is the number of signal dimuons (prompt and nonprompt J/ψ)
- 209 2. N_{Bkg} is the number of background dimuons
- 210 3. $F_{\text{Sig}}(\ell_{\text{J}/\psi})$ and $M_{\text{Sig}}(m_{\mu\mu})$ are the functional forms that describe the signal $\ell_{\text{J}/\psi}$ and mass
 211 shapes respectively
- 212 4. $F_{\text{Bkg}}(\ell_{\text{J}/\psi})$ and $M_{\text{Bkg}}(m_{\mu\mu})$ are the functional forms that describe the background $\ell_{\text{J}/\psi}$ and
 213 mass shapes respectively

214 Furthermore, $F_{\text{Sig,Bkg}}(\ell_{\text{J}/\psi})$ is given by

$$F_{\text{Sig,Bkg}}(\ell_{\text{J}/\psi,i}) = F_{\text{Sig,Bkg}}^{\text{true}}(\ell'_{\text{J}/\psi,i}) \otimes R(\ell_{\text{J}/\psi,i} - \ell'_{\text{J}/\psi,i} | \mu, s \cdot \sigma_{\ell,i}). \quad (4)$$

215 for each dimuon i , and with $\ell'_{\text{J}/\psi,i}$ is the true pseudo-proper decay length and $\ell_{\text{J}/\psi,i}$ the measured
 216 one. The different terms in eq. 4 are:

217 1. $R(\ell_{\text{J}/\psi,i} - \ell'_{\text{J}/\psi,i} | \mu, s \cdot \sigma_{\ell,i})$ is the resolution function for a given dimuon i with mean μ and
 218 width $s \cdot \sigma_{\ell,i}$ (the resolution depends on p_T and y thus is different for each dimuon). $\sigma_{\ell,i}$ is
 219 the error on $\ell_{\text{J}/\psi}$ estimated by the reconstruction algorithms, and s is a scale factor (close
 220 to 1) correcting this estimation¹. For prompt J/ψ , we have $\ell'_{\text{J}/\psi,i} = 0$, so the resolution
 221 function can be determined with the prompt J/ψ MC sample, or from data as explained
 222 in Sec. 4.2.2. This function is convolved with $F_{\text{Sig}}^{\text{true}}(\ell'_{\text{J}/\psi,i})$ and $F_{\text{Bkg}}^{\text{true}}(\ell'_{\text{J}/\psi,i})$ to obtain the
 223 measured $F_{\text{Sig,Bkg}}(\ell_{\text{J}/\psi,i})$ distributions that include detector resolution effects.

224 2. $F_{\text{Sig}}^{\text{true}}(\ell'_{\text{J}/\psi})$ is given by the sum of prompt and nonprompt components:

$$F_{\text{Sig}}^{\text{true}}(\ell'_{\text{J}/\psi}) = b F_{\text{NonPrompt}}^{\text{true}}(\ell'_{\text{J}/\psi}) + (1 - b) F_{\text{Prompt}}^{\text{true}}(\ell'_{\text{J}/\psi}) , \quad (5)$$

225 where b is the fraction of J/ψ from b hadron decays. By definition, $F_{\text{Prompt}}^{\text{true}}(\ell'_{\text{J}/\psi})$ is simply
 226 the Dirac distribution $\delta(0)$, while $F_{\text{NonPrompt}}^{\text{true}}(\ell'_{\text{J}/\psi})$ is an exponential decay.

227 3. $F_{\text{Bkg}}^{\text{true}}(\ell'_{\text{J}/\psi})$ is determined from fits on the data background $\ell_{\text{J}/\psi}$ distributions. The back-
 228 ground and signal distributions are unfolded as explained in Sec. 4.2.1.

229 More information about the parametrisation of the $\ell_{\text{J}/\psi}^{3\text{D}}$ distribution is given in Section 4.2.

230 When **per-event-uncertainties are included**, we need to add so-called Punzi-terms [17] to ac-
 231 count for distribution of the error on the lifetime, $\sigma_{\ell,i}$:

$$F_{\text{Sig,Bkg}}^{\mathcal{P}}(\ell_{\text{J}/\psi,i}, \sigma_{\ell,i}) = F_{\text{Sig,Bkg}}(\ell_{\text{J}/\psi,i}) \cdot \mathcal{P}_{\text{Sig,Bkg}}(\sigma_{\ell,i}) \quad (6)$$

232 where $\mathcal{P}_{\text{Sig,Bkg}}(\sigma_{\ell,i})$ is the probability distribution of $\sigma_{\ell,i}$ in signal or background.

233 The procedure to obtain the inputs needed for the 2D fits can be divided in two main parts,
 234 the invariant mass and pseudo-proper decay length parameterisations. These procedures are
 235 detailed in Sections 4.1 and 4.2 respectively. The final settings for the 2D fits and the results are
 236 given in Section 4.3

236 4.1 Invariant mass parameterisation

237 In this section we describe the procedure to obtain the $M_{\text{Sig}}(m_{\mu\mu})$ and $M_{\text{Bkg}}(m_{\mu\mu})$ invariant
 238 mass parameterisations in eq. 3. The invariant mass parameterisation procedure and analysis
 239 code is the same as the one used in HIN-16-025 analysis [9]. The J/ψ yield (inclusive, e.g.
 240 combined prompt and nonprompt J/ψ), $N_{\text{J}/\psi}$, is extracted separately by fitting the invariant
 241 $\mu^+\mu^-$ mass spectra (the projection of the 2D distribution). The invariant mass fits are done in
 242 the region $2.6 < m_{\mu^+\mu^-} < 3.5 \text{ GeV}/c^2$. These fits are unbinned maximum extended likelihood
 243 fits, performed using the RooFit [19] package.

244 The best model describing the signal has been determined based on MC simulations. The
 245 shape that gives the best χ^2 value for most of the bins is chosen as the nominal shape. The J/ψ
 246 nominal signal shape is defined by the weighted sum of two Crystal Ball functions $g_{2\text{CB}}(m_{\mu^+\mu^-})$
 247 ($f \cdot g_{\text{CB}_1}(m_{\mu^+\mu^-}) + (1 - f) \cdot g_{\text{CB}_2}(m_{\mu^+\mu^-})$), with common mean m_0 and tail parameters α and n .
 248 The Crystal Ball shape, g_{CB} , is defined in eq. 7. The Crystal Ball function $g_{\text{CB}}(m)$ combines a

¹If the estimated $\ell_{\text{J}/\psi}$ errors are correct, the distribution of $(\ell_{\text{J}/\psi} - \ell'_{\text{J}/\psi})/\sigma_{\ell}$ would have width $s = 1$.

249 Gaussian core and a power-law tail with an exponent n to account for energy loss due to final-
 250 state photon radiation, and a parameter α which defines the transition between the Gaussian
 251 and the power-law functions,

$$g_{\text{CB}}(m) = \begin{cases} \frac{N}{\sqrt{2\pi}\sigma_{\text{CB}}} \exp\left(-\frac{(m-m_0)^2}{2\sigma_{\text{CB}}^2}\right), & \text{for } \frac{m-m_0}{\sigma_{\text{CB}}} > -\alpha; \\ \frac{N}{\sqrt{2\pi}\sigma_{\text{CB}}} \left(\frac{n}{|\alpha|}\right)^n \exp\left(-\frac{|\alpha|^2}{2}\right) \left(\frac{n}{|\alpha|} - |\alpha| - \frac{m-m_0}{\sigma_{\text{CB}}}\right)^{-n}, & \text{for } \frac{m-m_0}{\sigma_{\text{CB}}} \leq -\alpha. \end{cases} \quad (7)$$

252 The study of the signal parameters is performed in MC on the different analysis bins. In pp α
 253 and n are fixed to the values extracted from MC. In PbPb, in addition to the tail parameters, the
 254 ratio of the sigmas is also fixed.

255 It was observed that α and the ratio of sigmas are independent of z , but this is not the case for
 256 n . Figs. 2 shows the dependence of α and n on z in pp and PbPb.

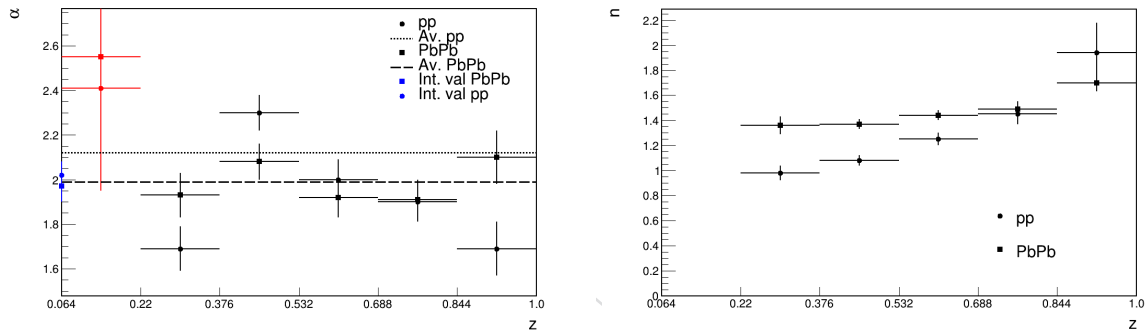


Figure 2: Evolution of α (left) and n (right) as a function of z in the rapidity range $|y| < 2.4$ for the double Crystal Ball, obtained from J/ψ fits in MC. In addition the values obtained in the z -average (dashed lines) over the different bins and z -integrated (blue points) values are reported.

256

257 So α and the ratio of sigmas are fixed to the z -integrated fit while n is extracted for each z bin.
 258 More details on the evolution of the parameters as a function of z are discussed in Appendix A.

259 Since it was shown in HIN-16-004 [20] that n and α do not depend on p_T , the increase of n could
 260 be caused by the clustering of the photon emitted by the muons in the jet, which means that
 261 at high z , where the J/ψ mesons are more isolated, the probability of having an extra photon
 262 would be low.

263 During the fitting procedure in data the following parameters are left free: f (the weight of the
 264 components of the double CB), m_0 (the J/ψ mass), $\sigma_{\text{CB}}, \sigma_{\text{CB}_2}/\sigma_{\text{CB}_1}$ and $N_{J/\psi}$ (the J/ψ yield). All
 265 other parameters are constrained or fixed to values from the simulation, as explained above.
 266 Alternative fitting procedures have been tried for the systematic uncertainty computation (see
 267 Sec. 7.1).

268 The background is described by a Chebychev polynomial of order N . The order N is deter-
 269 mined by performing a log-likelihood ratio (LLR) test separately for each analysis bin. This
 270 test compares the resulting minimised negative log-likelihood (NLL) of a fit with order N to
 271 the NLL with orders $N + 1$ and $N + 2$ (the second one is necessary to account for the change
 272 between odd and even parity as the order is increased).

273 In particular, 2 times the differences between the NLL values from the fits with polynomials of

274 orders N and $M > N$ follow a χ^2 distribution with $M - N$ degrees of freedom. The variables

$$\begin{aligned}\chi_{N \rightarrow N+1}^2 &:= 2(NLL_N - NLL_{N+1}) \\ \chi_{N \rightarrow N+2}^2 &:= 2(NLL_N - NLL_{N+2})\end{aligned}\quad (8)$$

275 can thus be used to decide whether or not the increase of order allows for the function fit the
276 data *significantly* better, where significantly better is defined to be the case as long as

$$\begin{aligned}p(\chi^2 \geq \chi_{N \rightarrow N+1}^2) &< 0.05 \\ p(\chi^2 \geq \chi_{N \rightarrow N+2}^2) &< 0.05.\end{aligned}\quad (9)$$

277 In Figure 3 an example of invariant mass fits in data, performed in two different analysis bins
278 following the above procedure is given as illustration.

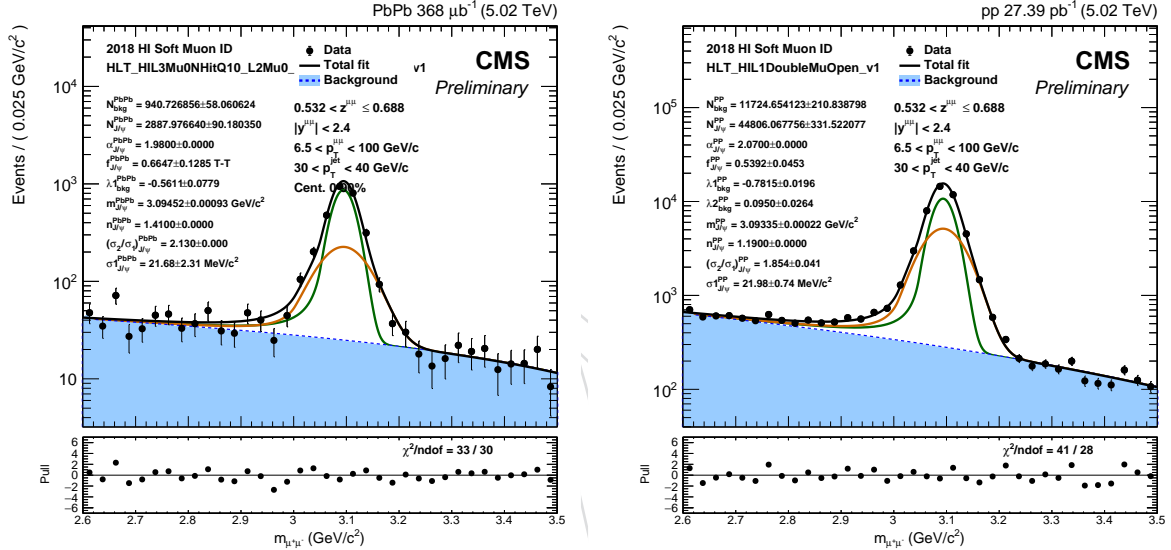


Figure 3: Example of nominal invariant mass fits for PbPb(left) and pp(right). The orange and green curves represent the two components of the double Crystal Ball function used for the fit.

279 **4.2 Pseudo-proper decay length parameterisation**

280 This section is dedicated to the description of the procedure employed to determine the $F_{Sig}(\ell_{J/\psi})$
 281 and $F_{Bkg}(\ell_{J/\psi})$ parameterisations of the pseudo-proper decay length in eq. 3. This is performed
 282 in 4 steps as listed below:

- 283 • Parameterisation of $\ell_{J/\psi}$ error distribution
- 284 • Parameterisation of lifetime resolution
- 285 • Parameterisation of b hadron decay length
- 286 • Parameterisation of $\ell_{J/\psi}$ distribution of background dimuons

287 The nominal procedure followed for each step is described in the corresponding sections below.

288 The studies made to estimate systematic uncertainties for each step are detailed in Sec. 7.2.

289 **4.2.1 Parameterisation of $\ell_{J/\psi}$ error distribution**

290 In this section we describe the procedure to obtain the parameterisation of the σ_ℓ distributions
 291 from data, the so-called Punzi terms $\mathcal{P}_{Sig,Bkg}(\sigma_{\ell,i})$ in eq.6. Since these distributions are different
 292 for signal and background, we need to disentangle them from the total distribution when using
 293 the per-event error technique. In addition, the σ_ℓ distributions are needed as input to obtain the
 294 parameterisations of the lifetime resolution and the $\ell_{J/\psi}$ distribution of background dimuons,
 295 in order to use the data σ_ℓ distribution both in data and MC fits. To separate the signal and
 296 background contributions we use the so-called $_sPlot$ technique [21]. This is fully integrated in
 297 the *RooStats* [22] package.

298 This technique applies for a data sample of events described by a multidimensional space of
 299 discriminating variables, where there are several sources of events (*i.e.* signal and background,
 300 prompt and nonprompt particles...). The basic concept of the $_sPlot$ technique consist of con-
 301 structing the so-called $_sWeights$ of the different categories of events, using the fit information on
 302 a discriminating variable. Then, the data sample can be weighted according to a given category
 303 of events, and plot the dataset for another variable.

304 In our specific case, we want to separate signal and background in the σ_ℓ distribution, so the
 305 discriminating variable is $m_{\mu\mu}$. The $_sWeights$ of signal and background can be constructed from
 306 the mass PDFs obtained in Sec. 4.1 in the following way:

$$\begin{aligned}
 {}_sW_{sig}(m_{\mu\mu}) &= \frac{V_{sig,bkg} \cdot M_{bkg}(m_{\mu\mu}) + V_{sig,sig} \cdot M_{sig}(m_{\mu\mu})}{N_{bkg} \cdot M_{bkg}(m_{\mu\mu}) + N_{sig} \cdot M_{sig}(m_{\mu\mu})} \\
 {}_sW_{bkg}(m_{\mu\mu}) &= \frac{V_{bkg,bkg} \cdot M_{bkg}(m_{\mu\mu}) + V_{bkg,sig} \cdot M_{sig}(m_{\mu\mu})}{N_{bkg} \cdot M_{bkg}(m_{\mu\mu}) + N_{sig} \cdot M_{sig}(m_{\mu\mu})} ,
 \end{aligned} \tag{10}$$

307 where $M_{sig,bkg}(m_{\mu\mu})$ are the signal and background PDFs, $N_{sig,bkg}$ are the yields of each com-
 308 ponent and $V_{i,j}$ is the covariance matrix of the i^{th} and j^{th} sources of events ($i, j = \text{signal and}$
 309 background).

310 Each weight is applied to the dataset and then it is projected on the σ_ℓ in order to obtain the
 311 signal and background σ_ℓ distributions. Finally, the resulting distributions are converted into
 312 *RooHistPdf* to be used as Punzi-terms. In order to avoid zeros on the pdf in the low statistics
 313 high σ_ℓ region, a limit is imposed in the σ_ℓ value, which is propagated to the rest of the analysis.
 314 This limit is obtained from the σ_ℓ histogram, and set at the value where the two following

consecutive bins are empty. An example of such distributions for two analysis bins in pp is presented in Fig.4. The number of events lost due to the limitation in σ_ℓ is written in the legend, and it is always smaller than 0.6%.

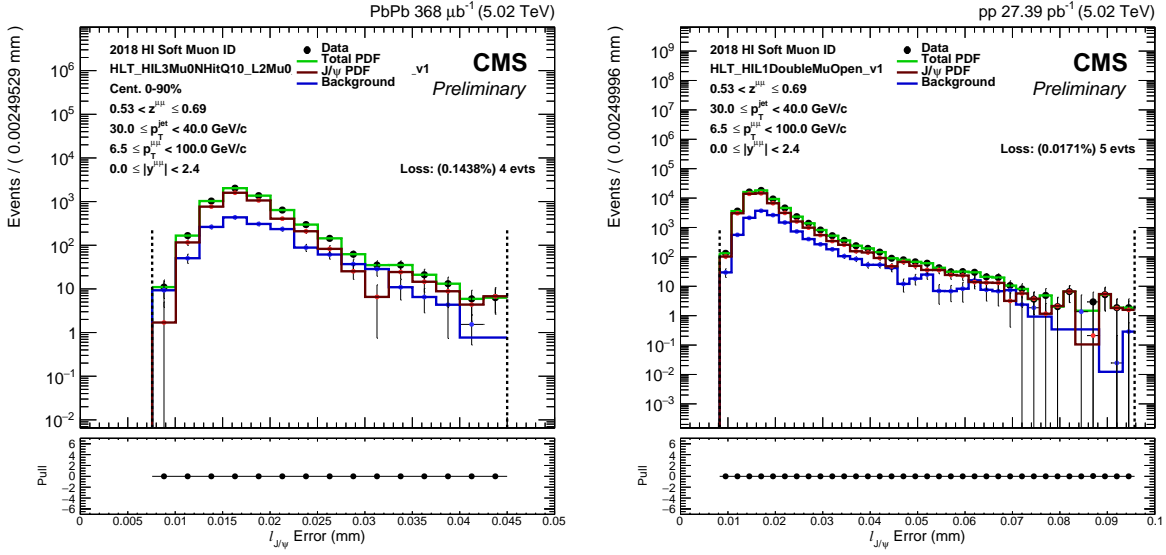


Figure 4: Two examples of σ_ℓ distributions for J/ψ and background and their corresponding PDFs in PbPb(left) and pp (right). The dashed lines represent the limits in the error distribution range, which is propagated to the rest of the analysis.

318 **4.2.2 Parameterisation of lifetime resolution**

319 In this section we describe the procedure to obtain the parameterisation of the lifetime resolution,
320 $R_i(\ell_{J/\psi}|\mu, s_i \sigma_\ell)$ in eq.4. The prompt $J/\psi \ell_{J/\psi}$ distribution can be considered as the lifetime
321 resolution. In order to obtain this distribution from data we assume that the negative tail in the
322 $\ell_{J/\psi}$ distribution should be mostly due to prompt J/ψ affected by resolution, so we use events
323 from this negative tail to determine the resolution. Among those events, we can have also
324 background dimuons, so the signal and background components are separated using the $sPlot$
325 technique, as in Sec. 4.2.1. The resulting distribution can be described by the weighted sum of
326 several Gaussian functions. One of them describes most of the core ('narrow') region, while the
327 other Gaussians take the tail ('wide') components.

$$R_i(\ell_{J/\psi}|\mu, s \cdot \sigma_\ell) = [f_{res} \cdot \text{Gauss}(\ell_{J/\psi}|\mu_1, s_1 \cdot \sigma_\ell) + \\ (1 - f_{res}) \cdot [f2_{res} \cdot \text{Gauss}(\ell_{J/\psi}|\mu_2, s_2 \cdot \sigma_\ell) + (1 - f2_{res}) \cdot \text{Gauss}(\ell_{J/\psi}|\mu_3, s_3 \cdot \sigma_\ell)]] \quad , \quad (11)$$

328 where the f_{res} and $f2_{res}$ are the relative weights of the individual gaussian functions on the total
329 resolution pdf. The Gaussian components have separated sigmas. It has been checked that the
330 mean of each component is always consistent with zero, and therefore they are fixed to zero
331 in the fits. The Punzi-terms used in the resolution PDFs are templates of the σ_ℓ distributions
332 obtained from real data in Sec. 4.2.1.

333 Examples for PbPb and pp resolution fits in data are given in Fig. 5. The dashed lines represent
334 only the fitting range, and no restriction is imposed in the resolution values in the following
335 steps of the analysis.

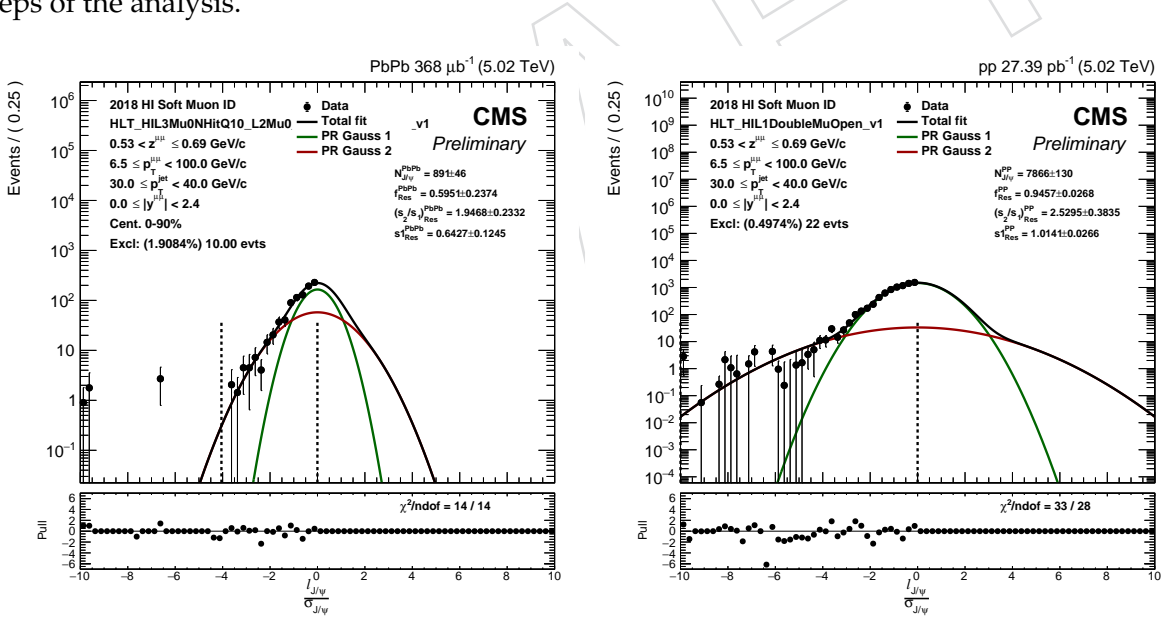


Figure 5: $\ell_{J/\psi}$ resolution distributions for J/ψ in data. The distributions are fitted with a weighted sum of two Gaussians. The dashed lines represent only the fitting range.

336 4.2.3 Parameterisation of b hadron decay length

337 In this section we describe the procedure to obtain the parameterisation of the b hadron de-
 338 cay length distributions, which is the b hadron component ($F_{\text{NonPrompt}}^{\text{true}}(\ell'_{\text{J}/\psi})$) of $F_{\text{Sig}}^{\text{true}}(\ell'_{\text{J}/\psi})$ in
 339 eq.5. The $F_{\text{NonPrompt}}^{\text{true}}(\ell'_{\text{J}/\psi})$ distribution of the b hadrons has an exponential behaviour. The J/ψ
 340 $\ell'_{\text{J}/\psi}$ distribution at generated level ($\ell'_{\text{J}/\psi}$) in nonprompt J/ψ MC can be described by a single
 341 exponential function,

$$F_{\text{NonPrompt}}^{\text{true}}(\ell'_{\text{J}/\psi}) = e^{-|\lambda_{\text{DSS}}| \cdot \ell'_{\text{J}/\psi}} , \quad (12)$$

342 where λ_{DSS} stands for the average decay length of b hadrons (Single Sided Decay). Examples
 343 of $F_{\text{NonPrompt}}^{\text{true}}(\ell'_{\text{J}/\psi})$ fits are shown in Fig.6 for pp and PbPb events.

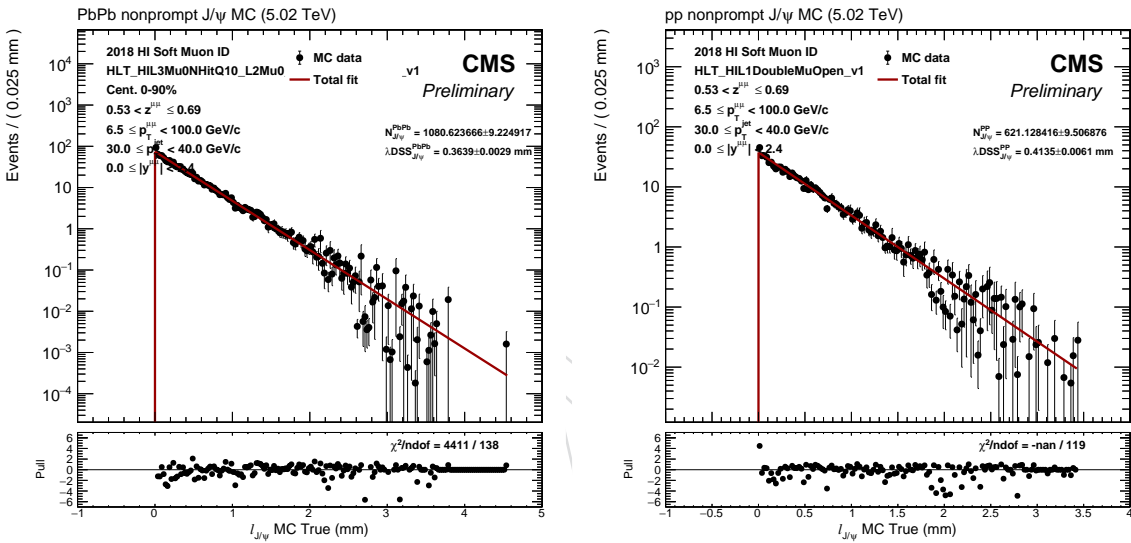


Figure 6: $F_{\text{NonPrompt}}^{\text{true}}(\ell'_{\text{J}/\psi})$ distributions in PbPb (left) and pp (right) events.

344 **4.2.4 Parameterisation of $\ell_{J/\psi}$ distribution of background dimuons**

345 In this section we describe the procedure to obtain the parameterisation of the decay length
 346 distributions of background dimuons, $F_{Bkg}^{true}(\ell'_{J/\psi})$ in eq.4. In order to use the full background
 347 statistics for the parameterisation we use the *sPlot* technique in Sec. 4.2.1 to obtain a background
 348 dataset. The same limit on the maximum and minimum σ_ℓ used for the σ_ℓ parameterisation is
 349 imposed here. The “nonprompt” (there is no actual physical notion of prompt and nonprompt
 350 for background) component of $F_{Bkg}^{true}(\ell'_{J/\psi})$ is described by a combination of a single-sided decay,
 351 a flipped single-sided decay and a double-sided decay functions, while the “prompt” compo-
 352 nent is described by a Dirac delta function:

$$F_{Bkg}^{true}(\ell'_{J/\psi}) = b_{bkg} \cdot \left[f_{DLIV} \cdot \left(f_{DFSS} \cdot e^{-|\lambda_{DSS}| \cdot \ell'_{J/\psi}} + (1 - f_{DFSS}) \cdot e^{|\lambda_{DF}| \cdot \ell'_{J/\psi}} \right) + (1 - f_{DLIV}) \cdot e^{-|\lambda_{DDS}| \cdot \ell'_{J/\psi}} \right] + (1 - b_{bkg}) \cdot \delta(\ell'_{J/\psi}), \quad (13)$$

353 where b_{bkg} represents the background “nonprompt fraction”. This function is convolved with
 354 the resolution functions obtained in Sec. 4.2.2 to fit the background reconstructed $\ell_{J/\psi}$ distribu-
 355 tions in data. All the resolution parameters are fixed to those obtained in data fits in Sec. 4.2.2.
 356 Examples of these background $\ell_{J/\psi}$ fits can be seen in Fig. 7 for pp and PbPb data.

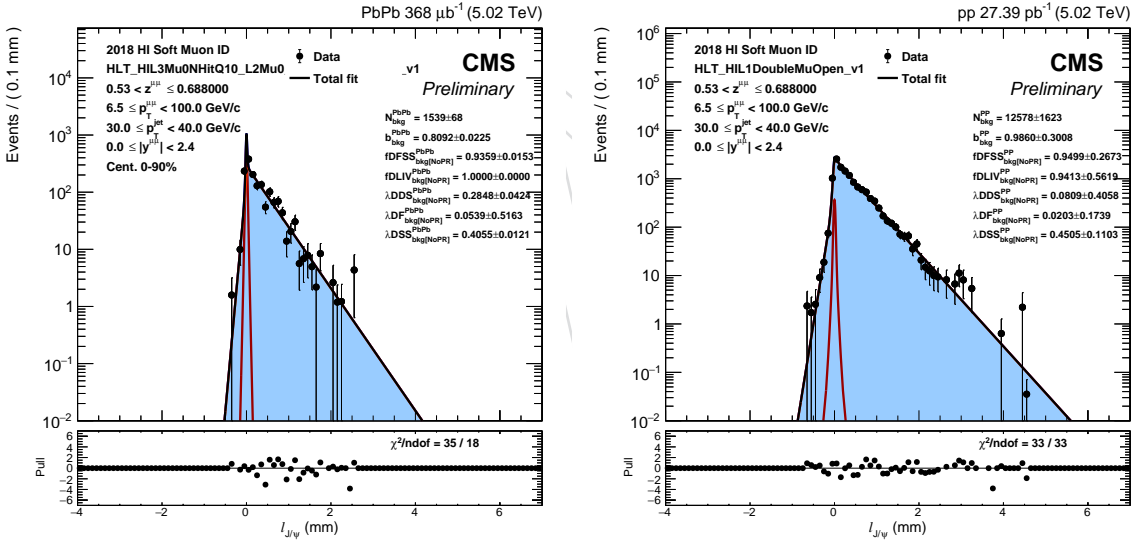


Figure 7: $F_{Bkg}(\ell_{J/\psi})$ distribution for PbPb (left) and pp (right).

4.3 Bidimensional fitting of invariant mass and pseudo-proper decay length

In this section we summarise the bidimensional fitting (2D fits) procedure of the invariant mass and pseudo-proper decay length. The settings for the 2D fits are the following:

- From the invariant mass parameterisations in Sec. 4.1 we fix all the signal and background parameters, except the number of inclusive J/ψ mesons, $N_{J/\psi}$, and the number of background dimuons, N_{bkg} , which are left as free parameters in the fits but constrained.
- The exponential decay parameters of the b hadron decay obtained from fits of the non prompt MC sample in Sec. 4.2.3 are used as initial parameters in the fit, and they are left free.
- All the parameters of the resolution function obtained in Sec. 4.2.2, are fixed from fits on the data sample.
- The parameters of the $\ell_{J/\psi}$ background fits obtained in Sec. 4.2.4 are all fixed in the 2D fits.
- The b fraction ($b_{J/\psi}$ in the plots), is a free parameter in the 2D fits.

An example of the mass and $\ell_{J/\psi}$ projections of these fits in pp can be seen in Fig. 8. The corresponding 2D PDFs are presented in Fig. 9.

DRAFT

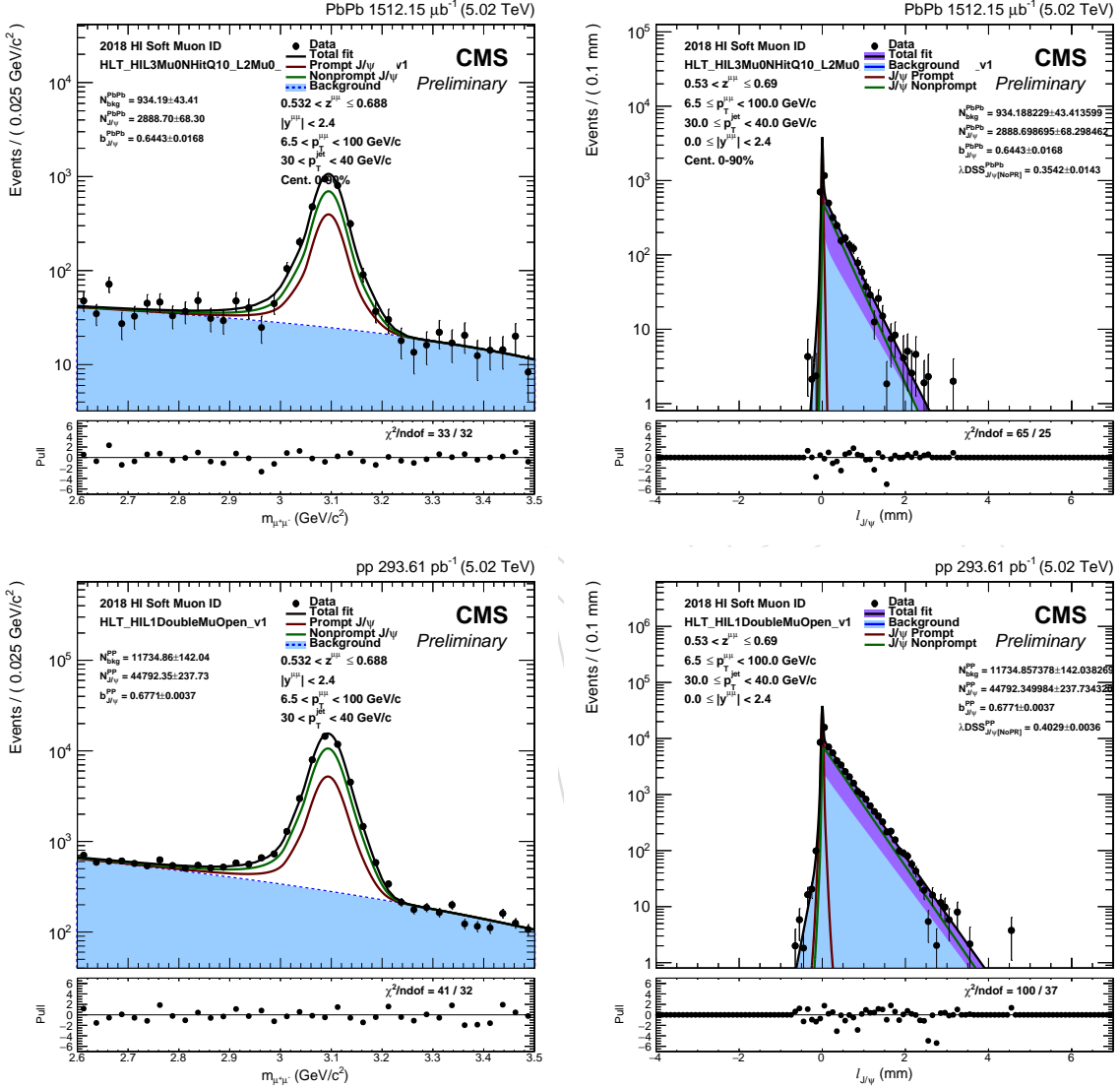


Figure 8: Invariant mass and $\ell_{J/\psi}$ projections of bidimensional fit of $\ell_{J/\psi}$ and invariant mass distributions for two given analysis bins.

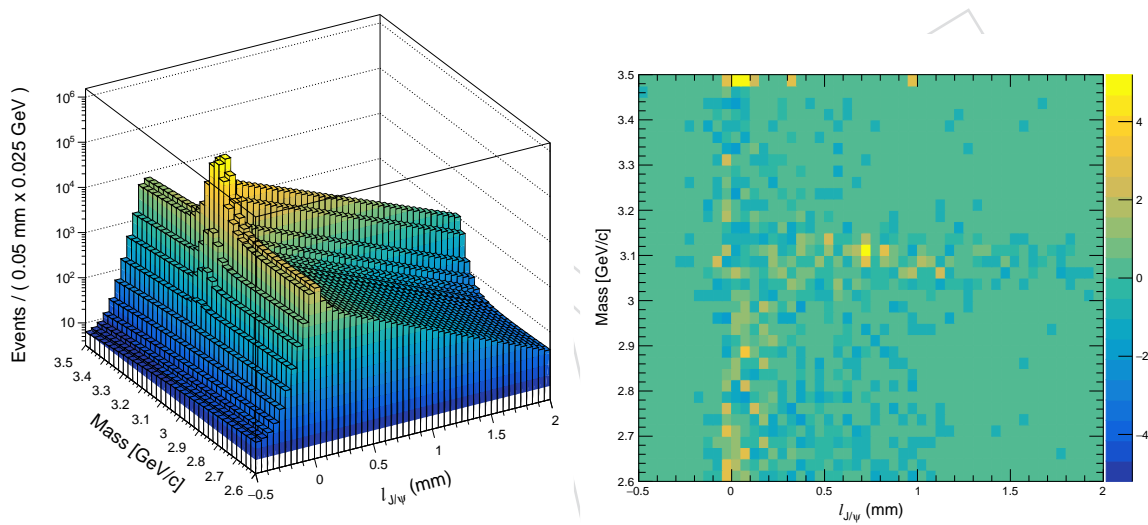


Figure 9: On the left: a bidimensional PDF of $\ell_{\text{J}/\psi}$ and invariant mass for a z bin in PbPb. On the right: the pull distribution of the fit

³⁷⁴ Finally, the number of prompt and nonprompt J/ψ mesons used for the results are simply com-
³⁷⁵ puted as:

$$\begin{aligned} N_{\text{prompt}}^{J/\psi} &= (1 - f_b) \cdot N^{J/\psi} , \\ N_{\text{nonprompt}}^{J/\psi} &= f_b \cdot N^{J/\psi} \end{aligned} \quad (14)$$

³⁷⁶ To compute the statistical uncertainties of the prompt and non prompt results, the correlation
³⁷⁷ of the non prompt fraction and the number of extracted inclusive J/ψ is taken into account.

DRAFT

378 5 Acceptance and Efficiency

Dimuon acceptances are computed with the following definition:

$$\alpha = \frac{N(\text{generated dimuons, both muons pass acceptance cuts})}{N(\text{all generated dimuons})} \quad (15)$$

379 where the single muon acceptance cuts have been defined in Eq. (1) in Section 3. Both single
 380 muons are required to pass the single muon kinematic cuts.

381 And dimuon efficiencies are computed with the following definition:

$$\varepsilon = \frac{N(\text{reconstructed dimuons, both muons passing analysis cuts})}{N(\text{generated dimuons, both muons passing acceptance cuts})} \quad (16)$$

382 where the analysis cuts have been defined in Section 3, and the acceptance cuts in Eq. (1).
 383 Therefore the efficiencies computed in this section include reconstruction, trigger and selec-
 384 tion efficiency. Reconstructed dimuons are also required to be of opposite sign, and to have
 385 a mass between $0.6\text{ GeV}/c$ below and $0.4\text{ GeV}/c$ above the J/ψ mass ($3.096\text{ GeV}/c$). At last, the
 386 reconstructed dimuons are asked to be matched to a generated dimuon, in the sense that the
 387 maximum $\Delta R_{\text{reco}-\text{gen}}^{\pm} = \sqrt{(\Delta\eta_{\text{reco}-\text{gen}}^{\pm})^2 + (\Delta\phi_{\text{reco}-\text{gen}}^{\pm})^2}$ between the reconstructed and gener-
 388 ated muons for each leg of the dimuon should be below 0.03.

Therefore $\text{Acc} \times \text{Eff}$ becomes:

$$\alpha \times \varepsilon = \frac{N(\text{reconstructed dimuons, both muons passing analysis cuts})}{N(\text{all generated dimuons})} \quad (17)$$

389 In order to take into account possible discrepancies between the single muon efficiencies com-
 390 puted in MC and those in data, the tag and probe (T&P) scale factors have to be applied to each
 391 single muon. These scale factors are computed centrally for all dimuon analyses in AN-18-316
 392 [15]. All single muons are corrected with Muon ID and trigger T&P scale factors. For pp a
 393 scale factor is derived for the “global” reconstruction, including both the tracking efficiency
 394 and stand-alone muon efficiency. For PbPb, only the tracking efficiency is evaluated.

395 The J/ψ acceptance and efficiency corrections are determined in simulation in finely binned
 396 maps of $J/\psi p_T$, η , and (in the case of PbPb efficiency) collision centrality. The correction is
 397 applied as a weight factor to each J/ψ prior to the signal extraction.

398 The binning of the corrections had to be carefully chosen to minimize the sensitivity of the
 399 corrections to the underlying shape of the distributions in MC, but within the statistical con-
 400 straints of the large, but still finite MC samples. This is particularly true in PbPb, where three
 401 binning dimensions are needed. To test the statistical precision of our $\text{Acc} \times \text{Eff}$ maps, a clo-
 402 sure test was performed by splitting the MC into two statistically independent samples. One
 403 was used to compute the corrections which are then applied on the second. The corrected reco
 404 distributions should match the gen distributions. To the extent that this is not the case, it in-
 405 dicates that the bins are too small and the corrections are fluctuating because of the statistics.
 406 Looking at the dependence of the efficiency on the three variables, we increased the number of
 407 bins until we started to see a nonclosure. Figure 10 shows the results of the closure test in pp
 408 (left), where the correction is done in 2D(p_T and η), and in PbPb (right), where the correction is
 409 done in 3D(p_T and η and centrality). A deviation of around 2% starts to be visible at the low-
 410 est value of J/ψ used in this analysis. This level of nonclosure is small compared to the other

411 sources of systematic uncertainty, and is hence acceptable. It does indicate, however, that we
 412 are approaching the limit of how finely we can bin. It should be noted that the true level of
 413 nonclosure should be a factor of $\sqrt{2}$ smaller, as this test reduces by half the number of events
 414 used for the map. We also explored several other choices, by rebinning one axis and binning
 415 more finely another, but we do not observe much difference in the closure test.

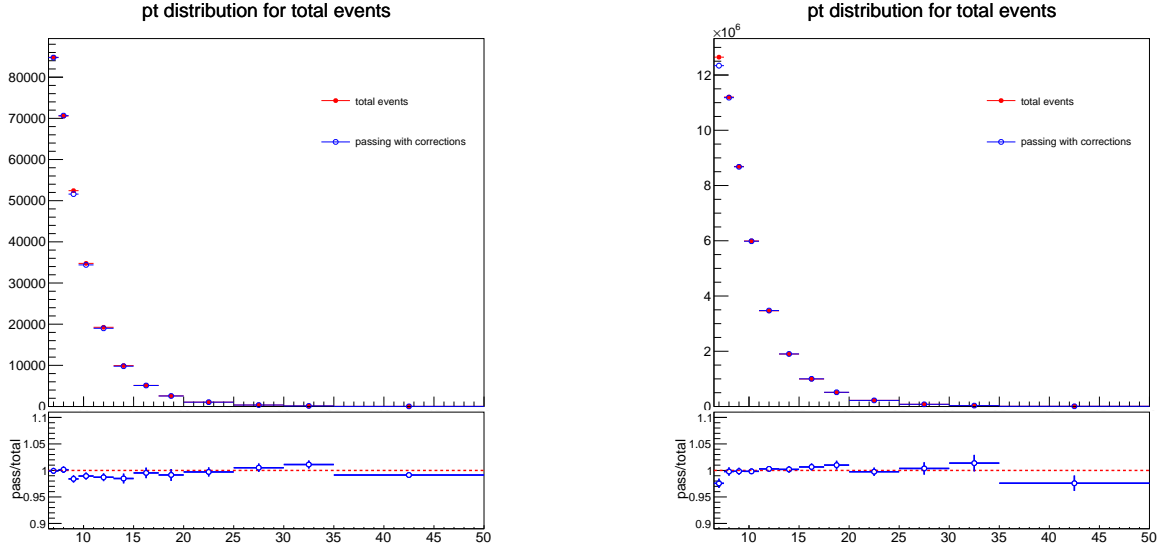


Figure 10: Closure tests for the 2D efficiency correction map used in pp (left) and 3D map used in PbPb (right).

416 Once we settled on our choice of fine binning we had to convince ourselves that finite bin size
 417 were under control. We did this by varying the shape of the spectrum in MC, taking advantage
 418 of two weight factors that are applied. Our MC simulations are done with a flattened \hat{p}_T
 419 distribution, in order to populate large values of $J/\psi p_T$. A per-event weight factor then applied, such
 420 that the natural shape of the \hat{p}_T distribution is restored. The PbPb MC is also produced by em-
 421 bedding into a minimum-bias (i.e., without any centrality selection/bias) background sample.
 422 The second weight factor we apply is to weight events by N_{coll} , to simulate the effect of the hard
 423 scattering centrality bias. We test for finite bin size effects by removing both of these weight
 424 factors. In order to avoid possible variations from the fitting procedure, we simply applied a
 425 tight restriction on the dimuon invariant mass. Fig. 11 shows the ratio of the inclusive (i.e.,
 426 without any jet requirement) $J/\psi p_T$ distribution, as well as the z distribution with the nominal
 427 jet selection. The bias on the results is within 1%. It should be noted that the difference in
 428 the spectral shape induced by removing these weights is far larger than the possible data/MC
 429 difference. Hence we assume that the finite bin size bias is negligible. The baseline corrections
 430 are chosen to be the ones without the weights applied, as this simplifies the evaluation of the
 431 statistical uncertainty on the $\text{Acc} \times \text{Eff}$ from the MC, as evaluated in Section 7.4.

432 The acceptance and efficiency corrections, for prompt J/ψ in pp and PbPb collisions are pre-
 433 sented in Fig. 12, as a function of p_T and rapidity. In the case of PbPb, the 0–5% centrality
 434 selection is shown.

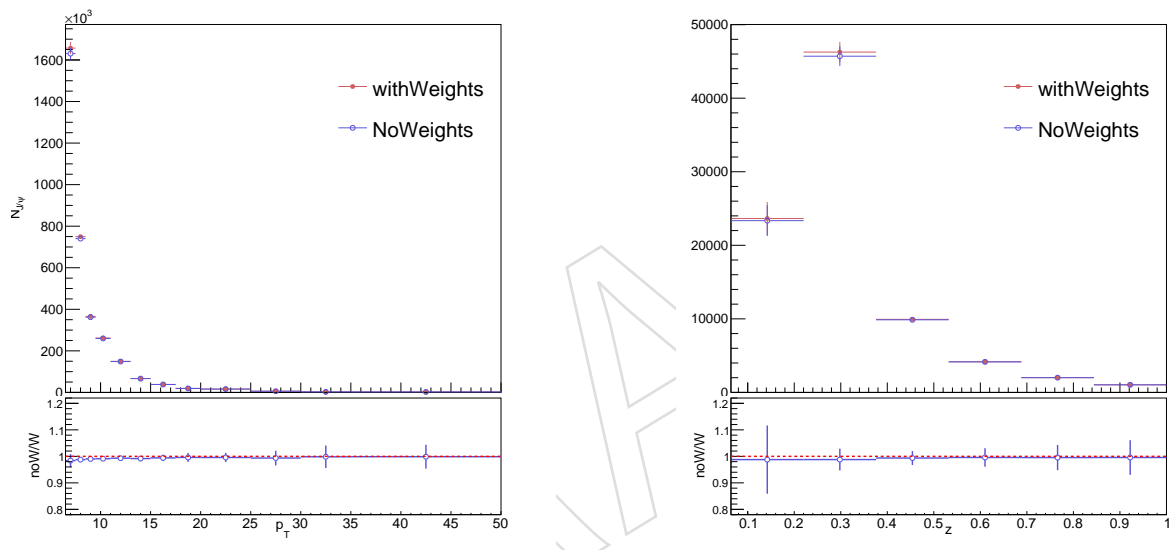


Figure 11: p_T and z distributions using corrections derived with and without MC weights.

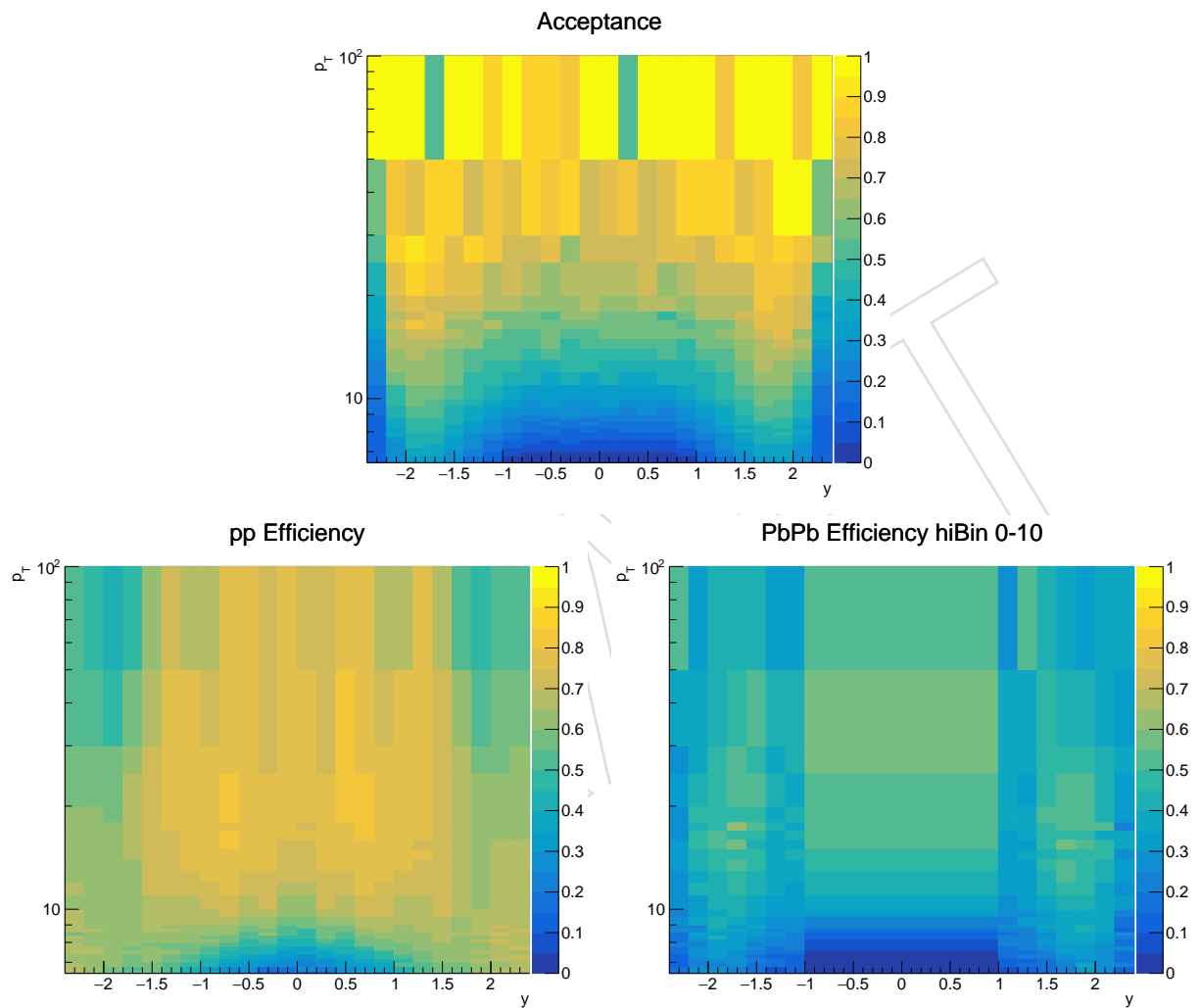
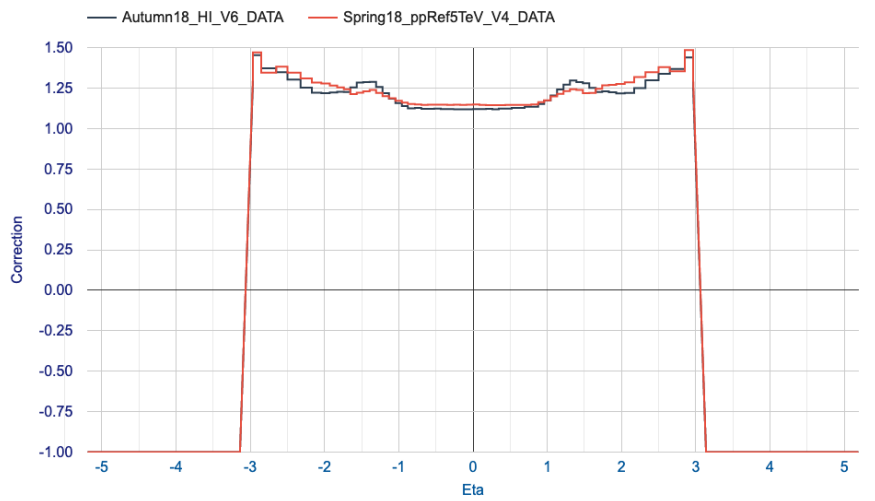


Figure 12: Acceptance (top) and efficiency (bottom) of prompt J/ψ as a function of p_T and rapidity in pp (left) and the most 5% most central PbPb (right) MC events.

435 6 Jet energy corrections and resolution

436 6.1 Jet energy corrections

437 This analysis uses standard jet energy corrections that are approved by the CMS JetMET group.
 438 These values are provided for us in the form of text files, with the tags Autumn18_HI_V6_X
 439 and Spring18_ppRef5TeV_V4_X, for PbPb and pp, respectively, and where “X” represents
 440 “DATA” or “MC”. These text files can be visualized with an online tool. Figure 13 shows the
 applied JECs for data as a function of η at a jet p_T value of 30 GeV.



441 Figure 13: The jet energy corrections applied to real data as a function of η at a jet p_T value of
 442 30 GeV, as obtained by the online viewer.

443 The factorized framework for producing these corrections is described in detail in Ref. [23]. In
 444 this framework, calibrations are derived in two steps, a “relative” correction, which flattens
 445 the detector response as a function of η in narrow ranges of p_T , followed by an “absolute”
 446 correction, which corrects the energy scale as a function of p_T . Such corrections are necessary
 447 due to the non-linear response of calorimeters. The momentum determination of the charged
 448 component of jets is driven by the tracking, such that the response requires very little additional
 449 calibration. On the other hand, the neutral components, especially the neutral hadrons, tend to
 be under-corrected for lower values of p_T .

450 Jet energy corrections are derived from an ensemble of inclusive jets, i.e., they average over all
 451 jet fragmentation patterns. In this analysis, however, we aim to measure the yield of jets as
 452 function of the jet fragmentation variable z . The response of jets as a function of the generator-
 453 level z is shown in Fig. 14 in pp (left) and PbPb (right) collisions. The open symbols show the
 454 response with the standard JECs, for both prompt and nonprompt J/ψ -jets. For pp collisions,
 455 as the value of z gets small, one observes that the response approaches unity, indicating that the
 456 standard JECs are appropriate. As z approaches one, however, one observes a response that
 457 is too large. In the limit of $z = 1$, the jet consists of a single J/ψ . Since the momentum of the
 458 decay muons is measured very precisely by the tracker, the jet kinematics are already close to
 459 the truth value *before* the application of the JECs. The size of the overcorrection at large z thus
 460 corresponds to the value of the JEC at that value of p_T (averaged over η).

461 To flatten the response vs. η , a rather simple procedure was developed in AN2017-319. Rather
 462 than applying the full JEC to the jet, one rather applies it only to the non- J/ψ component of

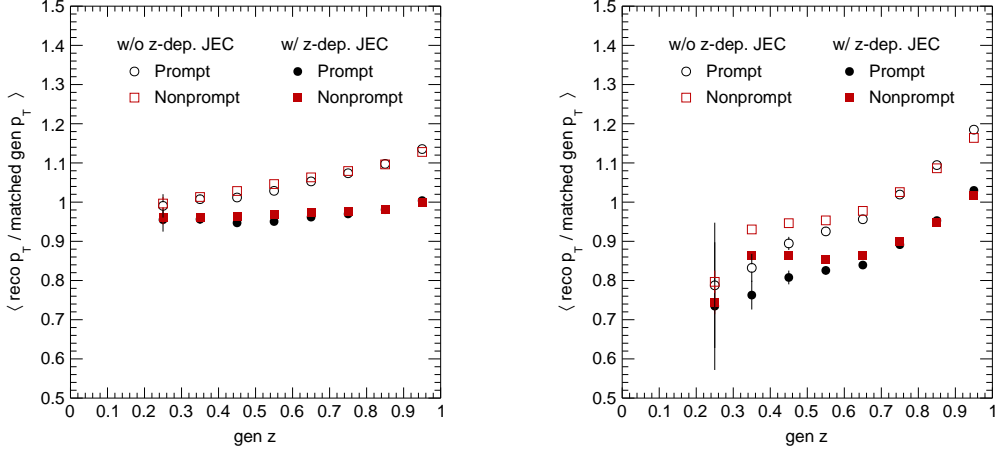


Figure 14: The response of J/ψ -jets vs. z , before (open symbols) and after (closed symbols) z -dependent corrections in pp (left) and $PbPb$ (right) collisions. Prompt and nonprompt J/ψ are shown separately, as indicated in the legend.

463 the jet. The new p_T of the jet after this procedure is obtained by combining the value with the
 464 standard correction $p_{T,\text{rec}}$ with the raw value without any correction $p_{T,\text{raw}}$, using the measured
 465 value of z , as follows.

$$p_{T,\text{new}} = (1 - z)p_{T,\text{rec}} + zp_{T,\text{raw}} \quad (18)$$

466 The response after this z -dependent correction is also shown in Fig. 14, in closed symbols. In
 467 pp collisions (left panel) one observes a much reduced dependence on z after this residual
 468 correction. At large z the response is very close to unity, as expected. At low z the response
 469 is few percent lower than unity, showing that the procedure works well, but is not exact. In
 470 $PbPb$ collisions (right panel) one again observes that the high z response is (un)corrected to
 471 unity. However, the overall dependence of the response on z is not much different than before
 472 application of the z -dependent corrections. This is due to the fact that the measured z value
 473 used in Eq. 18 has a poor correspondance with the that of the generator-level one. An isolated
 474 J/ψ , for example, will often be reconstructed at a low value of z in $PbPb$, due to a downward
 475 local fluctuation of the underlying event. The residual z -dependence of the JES is left to be
 476 corrected for by the unfolding procedure, as described in Section 9, which is performed both as
 477 function of jet p_T , and as a function of z . Nevertheless, the JECs play limiting the non-uniformity
 478 of the response in other variables that are not taken into account explicitly in the unfolding, in
 479 particular in η , over which the detector response to jets varies significantly.

480 Figures 15 and 16 show the response as a function of jet η in pp collisions for prompt and
 481 nonprompt J/ψ , respectively. Figures 17 and 18 show the same for $PbPb$. Again, the response is
 482 shown before the z -dependent corrections in open symbols and afterwards in closed symbols.
 483 Different slices in z are shown as indicated in the legend. In all cases the high z jets show
 484 a bow-shaped response with the standard corrections, which is effectively flattened by the z -
 485 dependent procedure. In pp collisions the z -dependence is generally quite flat after the residual
 486 z corrections. The same small residual z dependence is evident, as was shown in Fig. 14. In
 487 $PbPb$ collisions the larger remaining z -dependence is also again apparent. For each z bin the η
 488 dependence of the response is fairly flat. A small remaining bow shape in the η dependence of

489 the response at low z (more visible in the nonprompt sample, due to its better statistics at low
 490 z) is within the size of the systematic uncertainty on the JES, as determined from dijet balancing
 491 studies.

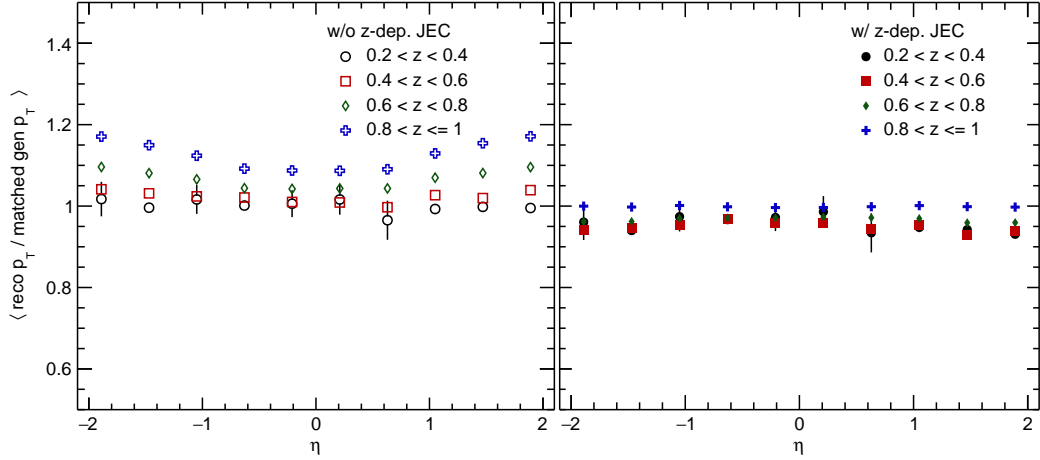


Figure 15: The response of prompt J/ψ -jets vs. η , before (left) and after (right) z -dependent corrections in pp collisions. Different slices in z are shown, as indicated in the legend.

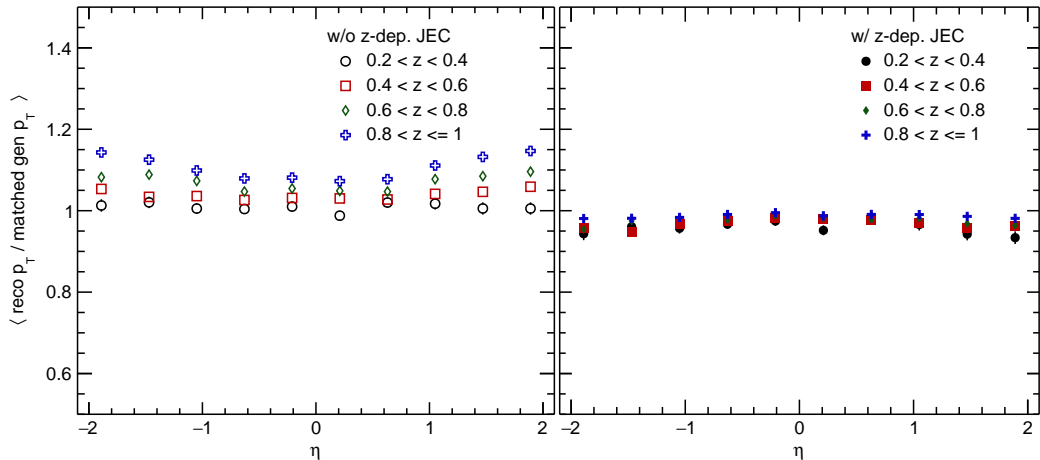


Figure 16: The response of nonprompt J/ψ -jets vs. η , before (left) and after (right) z -dependent corrections in pp collisions. Different slices in z are shown, as indicated in the legend.

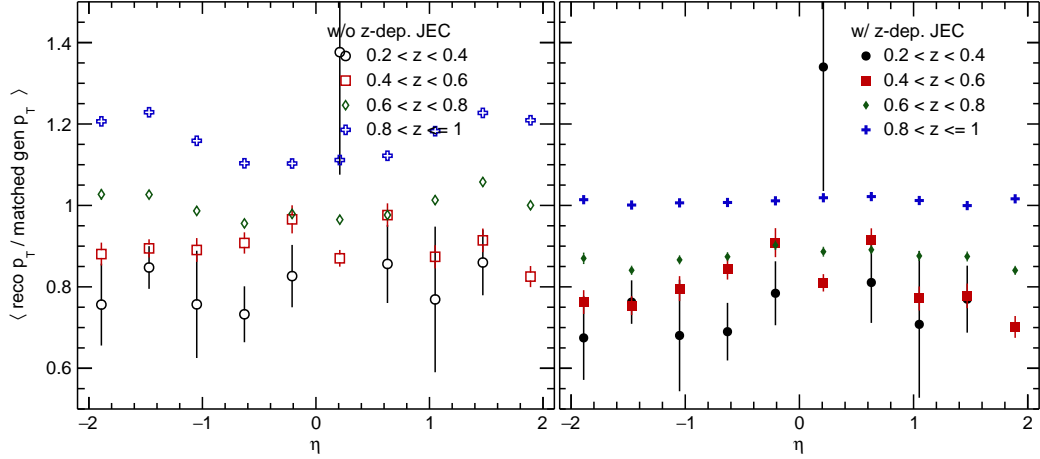


Figure 17: The response of prompt J/ψ -jets vs. η , before (left) and after (right) z -dependent corrections in PbPb collisions. Different slices in z are shown, as indicated in the legend.

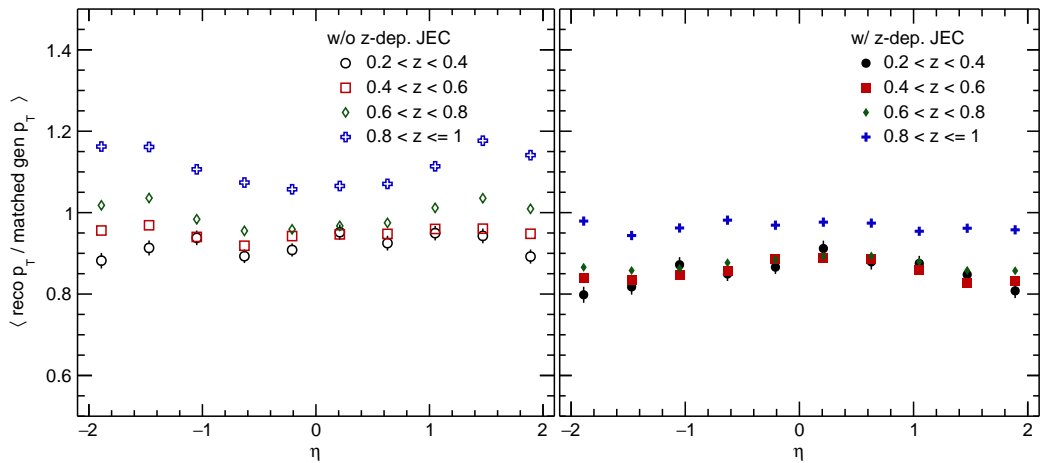


Figure 18: The response of nonprompt J/ψ -jets vs. η , before (left) and after (right) z -dependent corrections in PbPb collisions. Different slices in z are shown, as indicated in the legend.

492 **6.2 Jet energy resolution**

493 The resolution of jets in pp and PbPb is well described by the so-called CSN parametrization,
 494 where the relative uncertainty on p_T is given by:

$$\sigma(p_T)/p_T = \sqrt{C^2 + S^2/p_T + N^2/p_T/p_T}. \quad (19)$$

495 The noise term N , comes from the underlying event and is negligible compared to the two other
 496 contributions in the low pileup pp data used in this analysis (the stochastic term S dominates
 497 in the p_T range studied here). In PbPb collisions, simulations are well-described by centrality
 498 independent S and C values, with N values that depend on centrality. The C and S values
 499 derived from simulation by the jet reco group are 0.06 and 0.98 ($\sqrt{\text{GeV}}$).

500 The p_T resolution is known to be somewhat different in data and simulation. To take this
 501 into account, we treat the centrality-independent and dependent contributions separately. For
 502 the centrality independent contributions, we use the data/MC scale factors provided by the
 503 JetMET group. These scale factors and the corresponding uncertainties derived from high lu-
 504 minosity pp data in 2017 and 2018 can be viewed here: <https://twiki.cern.ch/twiki/bin/view/CMS/JetResolution>. In 2017 they are evaluated from data spanning running
 505 period B (near the beginning of the year) until running period F, which directly preceded the
 506 pp reference run (running period G) with the tag Fall17_V3. No scale factors are provided
 507 for individual running periods, rather the uncertainties cover the variation of detector perfor-
 508 mance over the course of the year. For the 2018 data, we use the scale factors that are provided
 509 for running period D alone (the one just preceding the PbPb run), although these scale factors
 510 are not very different from the ones provided that are averaged over the entire year, with the
 511 tag JER_Autumn18_RunD_V7_MC. Fig. 19 shows the scale factors and the uncertainties as a
 512 function of η for 2018 data.
 513

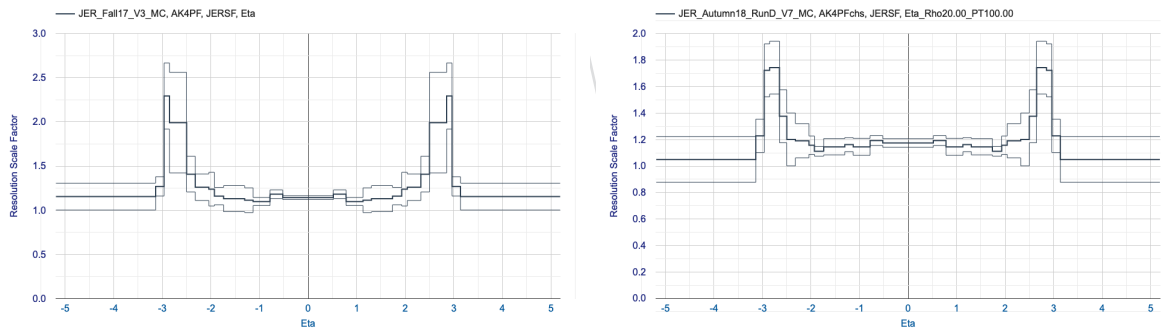


Figure 19: Data/MC scale factors as a function of η for pp (left) and PbPb (right), derived by the JETMet group.

514 In practice the MC values are smeared in the transfer matrix used in the unfolding, described
 515 in Section 9. The smearing procedure used is variant of the stochastic smearing approach de-
 516 scribed in the aforementioned JetMET twiki. We take the non-J/ ψ part of the jet and smear and
 517 reassign the reconstructed value of jet p_T by randomly sampling a Gaussian function. The cen-
 518 troid of the Gaussian is the original value of the reconstructed jet p_T . The width of the Gaussian
 519 is given by

$$p_{T,\text{meas}} * \sqrt{C^2 + S^2/p_{T,\text{true}}} * \sqrt{\text{SF}^2 - 1}, \quad (20)$$

520 where $p_{T,\text{meas}}$ and $p_{T,\text{true}}$ are the measured and generator-level p_T values, respectively, for the
 521 non- J/ψ part of the jet. SF is the scale factor. The values of C and S are the ones taken from
 522 Ref. [24].

523 To check the validity of our smearing approach we ran a simply toy MC, which is shown in
 524 Fig. 20. We smeared jets of $p_T = 35\text{ GeV}$ by the CSN parameterization in Eq. 19, using two
 525 choices of $N = 0\text{ GeV}$ and $N = 5\text{ GeV}$, to represent pp and PbPb, respectively. The exact value
 526 is immaterial for this test, $N = 5\text{ GeV}$ was chosen purely for visibility on the final plots. We
 527 then smeared the jets a second time, inflating the C and S values by an arbitrary scale factor of
 528 1.25. Finally, we smeared the jets according to our analysis procedure. We take the jets smeared
 529 by the original factor (without the scale factor), and then apply an additional smearing to the
 530 reconstructed jet p_T value according to Eq. 20. The analysis procedure is found to reproduce
 531 the p_T distribution of jets with resolution given by the data/MC scale factors.

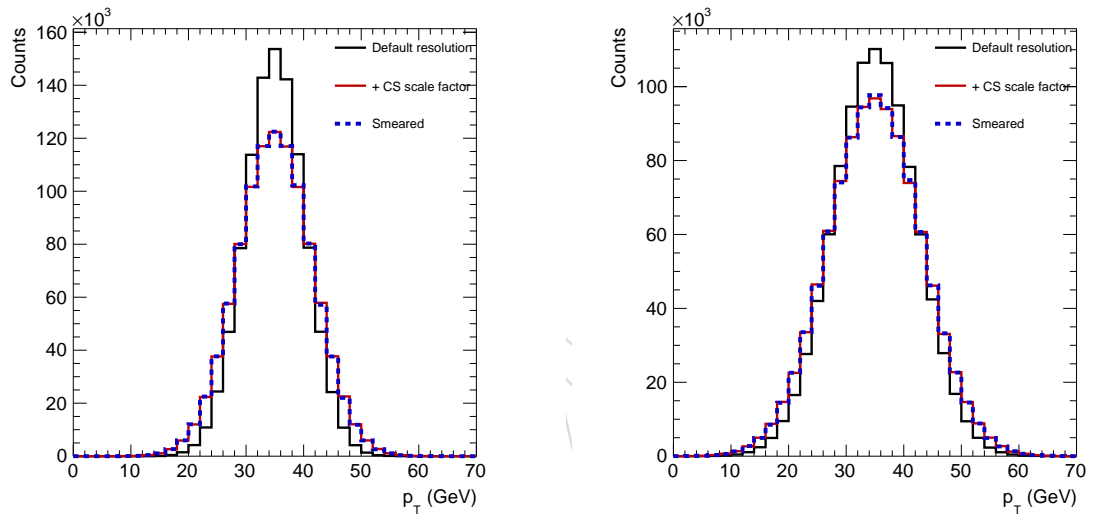


Figure 20: Smearing of the JER for jets of 35 GeV with $N = 0$ and $N = 5$. The smeared values are shown with the default C and S values (black line) and with an arbitrary scale factor (red line). The blue line shows the smearing according to the analysis procedure described in the text.

532 The uncertainty on the value is evaluated based on the random cone studies performed in anal-
 533 ysis HIN-19-013. The p_T density (ρ) evaluated in random cones was found to be overestimated
 534 in MC. Good agreement between data and MC was found by shifting the MC centrality def-
 535 inition by 4.5%, such that, e.g., one compares 0 – 10% data to 4.5 – 14.5% MC. A comparison
 536 of the underlying event energy density from random cones in data and simulation is shown
 537 in Fig. 21. The rest of the study may be found in https://twiki.cern.ch/twiki/pub/CMS/HiJetReco2019/c_rho_eta_allEta.pdf. The plots show that a variation by 1.5%
 538 in centrality up and down is sufficient to cover data-MC differences in the ρ distribution. We
 539 use these variations to the transfer matrix to assign an uncertainty on the jet resolution from the
 540 UE.

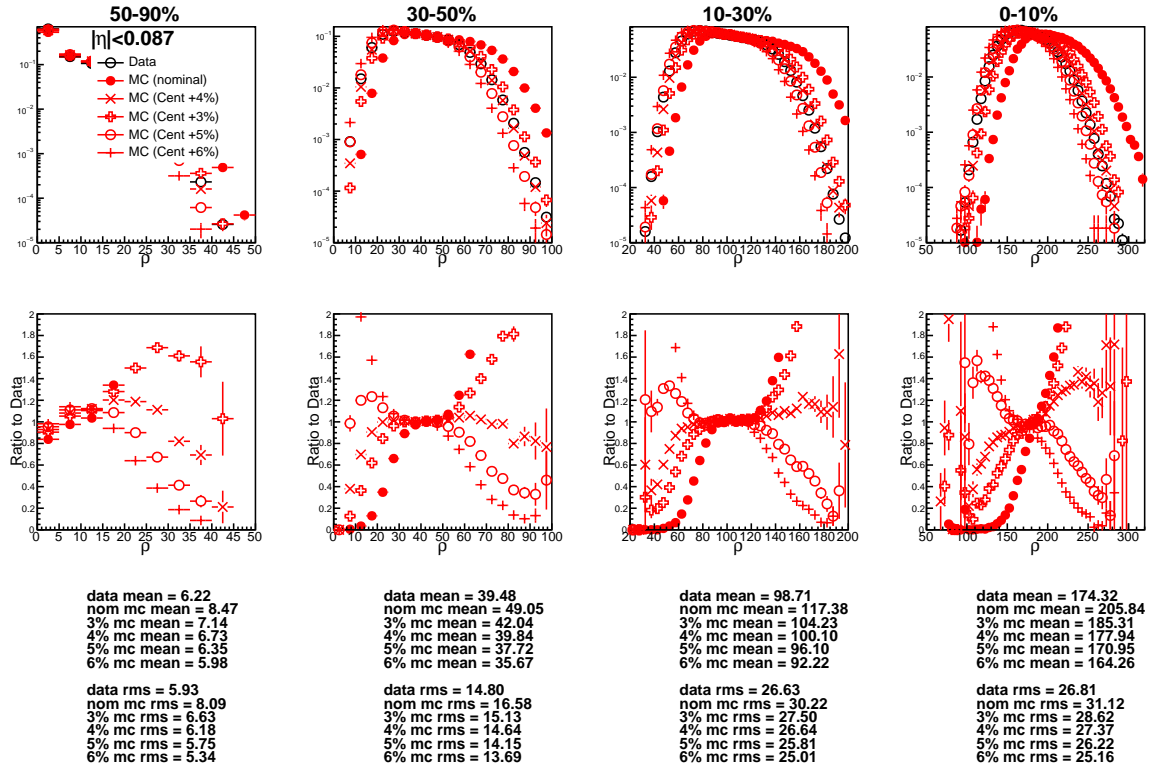


Figure 21: Underlying event density (ρ) from random cones in data and HYDJET simulation, for various centrality selections, in a central pseudorapidity region ($\eta < 0.087$). In addition to the default simulation, the simulation is shown shifted by 3,4,5 and 6% in centrality.

542 **7 J/ψ signal extraction systematic uncertainties**

543 In this section we describe the procedure for the estimation of the systematic uncertainties of
544 each step of the analysis.

545 **7.1 Invariant mass parameterisation uncertainty**

546 The tests to determine the systematic uncertainties on the different ingredients of the invariant
547 mass parameterisation are the following:

548 On the signal side:

- 549 1. Variation of signal parameters for the nominal shape (double Crystal Ball): fits on data
550 are performed by leaving free the parameters that were fixed from MC in the nominal fits
551 one by one. See details in Sec. 7.1.1.
- 552 2. Variation of the signal shape: use a Crystal Ball plus a Gaussian function as signal shape
553 instead of the double Crystal Ball function.

554 On the background side:

- 555 1. Variation of the fitting range. Use 2.6-3.4 instead of 2.6-3.5.
- 556 2. Use an exponential of Chebychev polynomials instead of the Chebychev polynomials for
557 the background parameterisation

558 In the cases where several tests are made for the same item listed above, the maximum de-
559 viation from the nominal value of the prompt and nonprompt J/ψ yields obtained with these
560 variations is taken as systematic uncertainty for each source. Finally the uncertainties from the
561 different sources will be added in quadrature.

562 The different tests performed for the determination of the systematic uncertainties are dis-
563 cussed in detail in the following subsections.

564 **7.1.1 Variation of signal parameters**

565 In order to estimate the uncertainty due to the determination of the signal parameters from
566 MC, we perform fits in data leaving the fixed parameters free one by one.

567 In Figure 22 an example of the invariant mass fits with the double Crystal Ball function in data,
568 performed in two different analysis bins following the above procedure, is given as illustration.
569 These plots are to be compared with the nominal ones in Fig.3. As we can observe the reduced
570 χ^2 shows almost no variation with respect to the nominal fits.

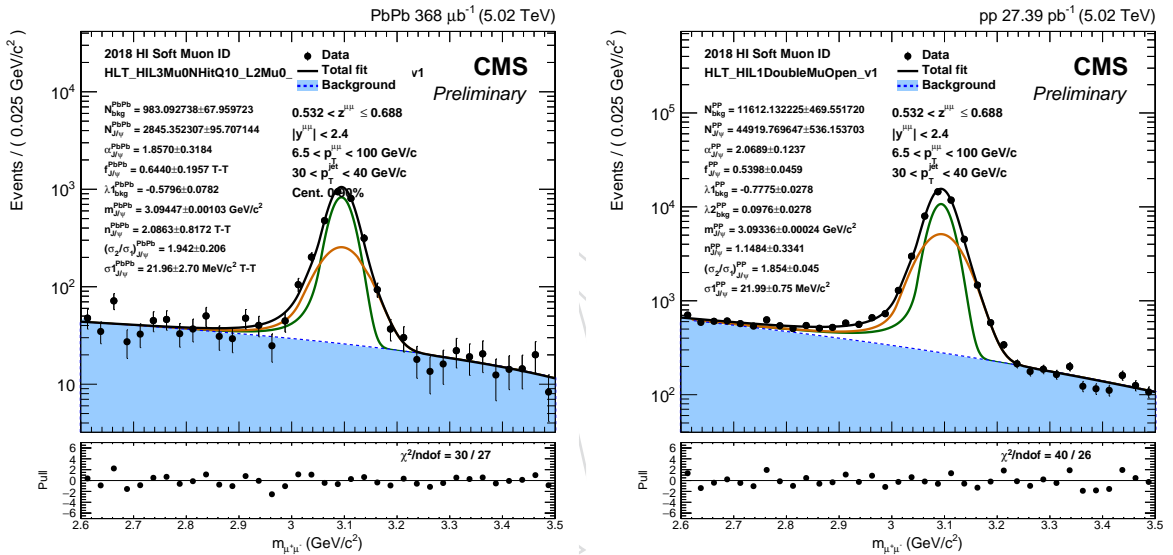


Figure 22: Examples of invariant mass constrained fits for in pp and PbPb data.

571 **7.1.2 Variation of signal shape**

572 For these tests, a Crystal Ball plus a Gaussian function is used instead of the double Crystal Ball
 573 function: $g_{\text{CBG}}(m_{\mu^+\mu^-}) (f \cdot g_{\text{CB}}(m_{\mu^+\mu^-}) + (1 - f) \cdot g_{\text{G}}(m_{\mu^+\mu^-}))$, were g_{CB} is the Crystal Ball shape
 574 defined in Eq. 7 and g_{G} is just a Gaussian shape. The signal parameters of the Crystal Ball plus
 575 Gaussian shape are determined from MC fits in the same way as for the double Crystal Ball
 576 shape.

577 In this case, the tail parameters α and n are fixed to the values found in MC. The same nom-
 578 inal background functions obtained with the double Crystal Ball function are used, but the
 579 background parameters are left free.

580 In Figure 23 an example of the invariant mass fits with the Crystal Ball plus Gaussian function
 581 in data, performed in two different analysis bins, following the above procedure is given as
 582 illustration. If we compare these plots with the nominal ones in Fig.3 we can observe that
 583 the reduced χ^2 is similar. The extracted number of J/ψ vary by 0.6% (0.1%) at mid (forward)
 584 rapidity for these specific fits.

585 By using a new signal shape, a new set of α , n and σ_2/σ_1 had to be derived following exactly
 586 the same way the nominal values were obtained.

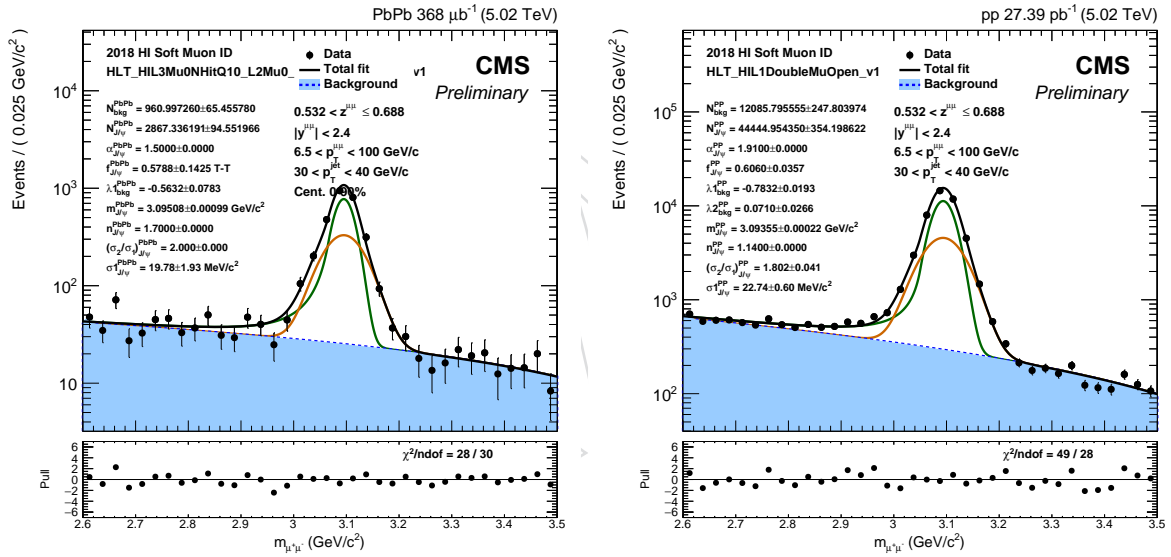


Figure 23: Example of invariant mass fits with the Crystal Ball plus Gaussian function in pp and PbPb data.

Table 2: Nominal α , n and σ_2/σ_1 values

Jet p_T (GeV/c)	Alpha pp	Alpha Pb-Pb	σ_2/σ_1 Pb-Pb
40-60	2.04 ± 0.09	1.8 ± 0.1	1.9 ± 0.1
30-40	2.02 ± 0.05	1.97 ± 0.07	2.0 ± 0.1
10-30	2.01 ± 0.01	1.93 ± 0.01	1.89 ± 0.01
6.5-10	2.01 ± 0.02	1.95 ± 0.03	1.7 ± 0.03

Table 3: Nominal n values for different jet p_T bins in pp

z	6.5-10 GeV/c	10-30 GeV/c	30-40 GeV/c	40-60 GeV/c
0.064-0.22	-	-	-	-
0.22-0.376	-	1.19 ± 0.06	0.98 ± 0.06	0.98 ± 0.08
0.376-0.532	-	1.24 ± 0.02	1.08 ± 0.03	1.18 ± 0.06
0.532-0.688	1.28 ± 0.01	1.28 ± 0.01	1.25 ± 0.04	1.23 ± 0.07
0.688-0.844	1.3 ± 0.01	1.3 ± 0.01	1.45 ± 0.08	1.5 ± 0.1
0.844-1	1.6 ± 0.01	1.6 ± 0.01	1.9 ± 0.2	1.6 ± 0.3

Table 4: Nominal n values for different jet p_T bins in Pb-Pb

z	6.5-10 GeV/c	10-30 GeV/c	30-40 GeV/c	40-60 GeV/c
0.064-0.22	-	-	-	-
0.22-0.376	-	1.45 ± 0.07	1.35 ± 0.06	1.46 ± 0.06
0.376-0.532	-	1.51 ± 0.04	1.36 ± 0.03	1.49 ± 0.04
0.532-0.688	-	1.45 ± 0.03	1.43 ± 0.04	1.62 ± 0.07
0.688-0.844	1.4 ± 0.1	1.5 ± 0.02	1.49 ± 0.05	1.85 ± 0.09
0.844-1	1.55 ± 0.02	1.59 ± 0.01	1.7 ± 0.07	2.01 ± 0.08

Table 5: Varied α , n and σ_2/σ_1 values

Jet p_T (GeV/c)	Alpha pp	Alpha Pb-Pb	σ_2/σ_1 Pb-Pb
40-60	1.9 ± 0.1	1.5 ± 0.3	1.8 ± 0.1
30-40	1.91 ± 0.08	1.5 ± 0.2	2 ± 0.1
10-30	1.83 ± 0.02	1.77 ± 0.04	1.86 ± 0.01
6.5-10	1.83 ± 0.02	1.81 ± 0.04	1.68 ± 0.02

Table 6: Varied n values for different jet p_T bins in pp

z	6.5-10 GeV/c	10-30 GeV/c	30-40 GeV/c	40-60 GeV/c
0.064-0.22	-	-	-	-
0.22-0.376	-	1.4 ± 0.1	0.9 ± 0.1	0.8 ± 0.1
0.376-0.532	-	1.08 ± 0.03	0.91 ± 0.05	1.2 ± 0.1
0.532-0.688	1.14 ± 0.03	1.14 ± 0.03	1.14 ± 0.07	1.24 ± 0.08
0.688-0.844	1.21 ± 0.02	1.21 ± 0.02	1.29 ± 0.09	1.2 ± 0.2
0.844-1	1.48 ± 0.01	1.48 ± 0.01	1.8 ± 0.2	1.3 ± 0.2

Table 7: Varied n values for different jet p_T bins in Pb-Pb

z	6.5-10 GeV/c	10-30 GeV/c	30-40 GeV/c	40-60 GeV/c
0.064-0.22	-	-	-	-
0.22-0.376	-	1.34 ± 0.03	1.5 ± 0.1	1.46 ± 0.09
0.376-0.532	-	1.47 ± 0.06	1.56 ± 0.06	1.5 ± 0.07
0.532-0.688	-	1.23 ± 0.08	1.73 ± 0.07	1.6 ± 0.1
0.688-0.844	1.4 ± 0.1	1.3 ± 0.05	1.8 ± 0.1	1.8 ± 0.2
0.844-1	1.36 ± 0.03	1.4 ± 0.01	1.7 ± 0.1	2.0 ± 0.2

587 7.1.3 Variation of invariant mass fitting range

588 In order to estimate how the background parameterisation (and hence the extracted number
 589 of J/ψ) is affected by the choice of the invariant mass range, we vary the fitting range from
 590 2.6-3.5 GeV/ c^2 to 2.6-3.4 GeV/ c^2 . The order of the Chebychev polynomial function used to
 591 parametrise the background is the same as the one used for the nominal fits.

592 In Figure 24 we give an example of the invariant mass fits with the reduced invariant mass
 593 range in data, performed in two different analysis bins. If we compare these plots with the
 594 nominal ones in Fig.3 we can observe that the reduced χ^2 is similar.

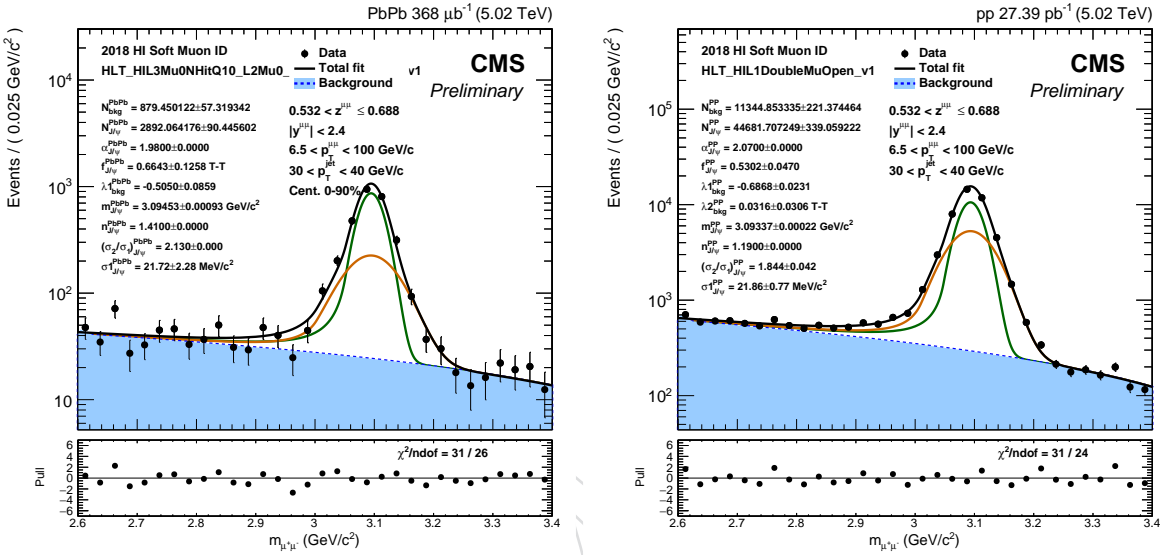


Figure 24: Example of invariant mass fits with reduced mass range in pp and PbPb data.

595 7.1.4 Variation of background shape

596 The last systematic test for the background parameterisation is on the choice of the background
 597 shape itself. In this case we change the functional form of the background shape from a Cheby-
 598 chev polynomial to an exponential of a Chebychev polynomial. We perform the fits using
 599 orders 0-6 for the polynomial in the exponential, and we apply the LLR test with 5% as p-value
 600 in order to determine the best order for each analysis bin.

601 In Figure 25 an example of the invariant mass fits using the exponential of Chebychev polyno-
 602 mials to parametrise the background in data, performed in two different analysis bins is given
 603 as illustration. If we compare these plots with the nominal ones in Fig.3 we can observe that
 604 the reduced χ^2 is similar.

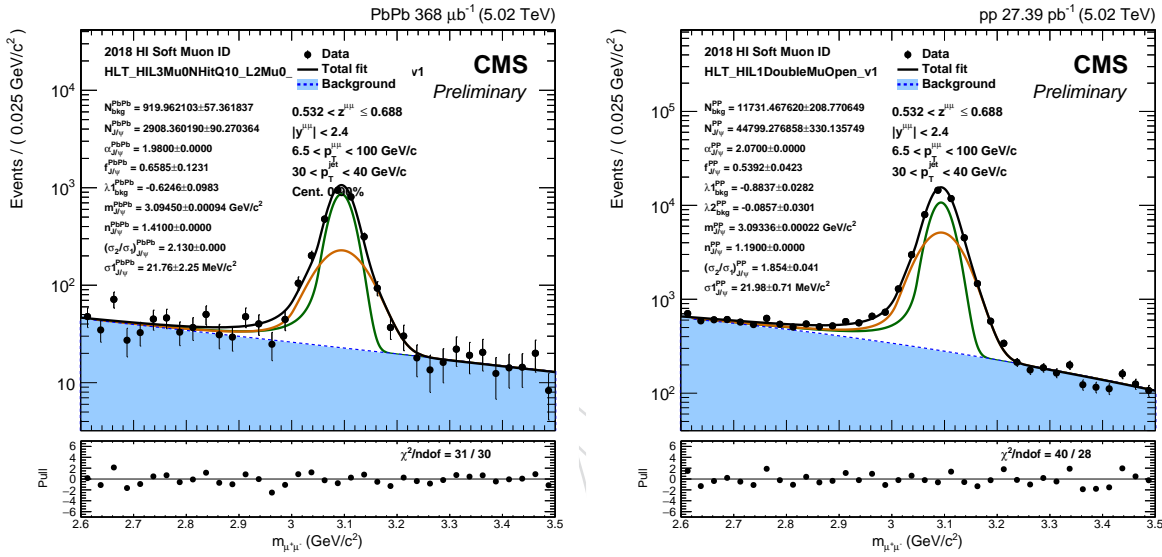


Figure 25: Example of invariant mass fits using the exponential of Chebychev polynomials for the background in pp and PbPb data.

605 7.2 Pseudo-proper decay length parameterisation uncertainty

606 The systematic uncertainties on the pseudo-proper decay length parameterisation are the fol-
607 lowing:

608 On the error distributions side:

- 609 1. Propagate the invariant mass systematic tests to the PDF of the error distribution. It was
610 shown in [9] that this uncertainty can be neglected.
- 611 2. Use the total $\ell_{J/\psi}$ error distribution instead of the signal and background ones in the 2D
612 fits this has no influence on the $\ell_{J/\psi}$ resolution, so no need to take this into account there).

613 On the resolution side:

- 614 1. Use the $\ell_{J/\psi}$ resolution from prompt MC

615 On the b hadron decay length side:

- 616 1. Make a template of the nonprompt MC reco $\ell_{J/\psi}$ distribution instead of the one side decay
617 function convolved with the resolution function.

618 On the background distributions side:

- 619 1. Make a template of the distribution instead of the fit
- 620 2. Propagate the prompt MC $\ell_{J/\psi}$ resolution to these fits

621 7.2.1 Systematics on $\ell_{J/\psi}$ resolution

622 In order to estimate the systematic uncertainty due to the parameterisation of the $\ell_{J/\psi}$ resolu-
623 tion, we obtain the resolution from prompt J/ψ MC (It was shown in [9] that the nonprompt
624 MC samples were not appropriated for this). The $\ell_{J/\psi}$ resolution can be directly determined by
625 fitting the prompt J/ψ MC sample, since the true $\ell_{J/\psi}$ value is zero. The resulting distributions
626 are then fitted with the weighted sum of two gaussian functions as for the case of the nominal
627 resolution fits in data. The Punzi-terms used in the resolution PDFs are templates of the σ_ℓ
628 distributions obtained from real data in Sec. 4.2.1. In Fig. 26 we give two examples of the $\ell_{J/\psi}$
629 resolution parameterisation for pp MC events.

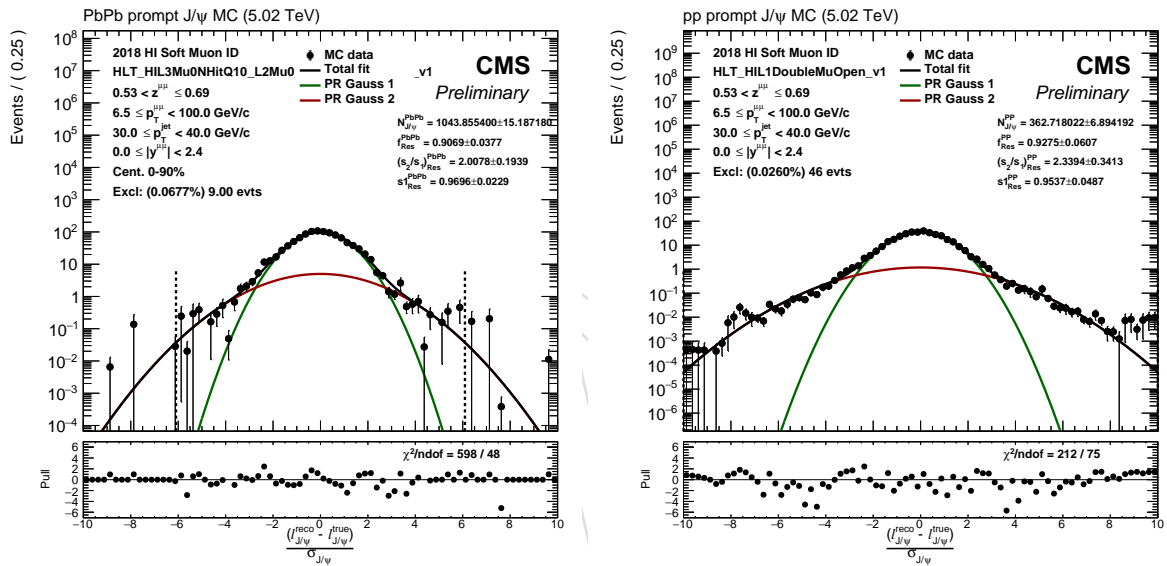


Figure 26: $\ell_{J/\psi}$ resolution distributions for prompt J/ψ MC sample. The distributions are fitted with a weighted sum of two Gaussians. The dashed lines represent only the fitting range.

630 7.2.2 Systematics on b hadron decay parameterisation

631 In this case instead of using the convolution of the resolution function with the exponential
 632 decay function initialised with the nonprompt J/ψ MC value of the b decay length, a template
 633 of the reconstructed $\ell_{J/\psi}$ distribution in nonprompt J/ψ MC is used in the 2D fitting procedure.
 634 The templates are made using RooKeysPdf [25]. These PDF templates have to be multiplied by
 635 the corresponding data $\ell_{J/\psi}$ error distribution (Punzi terms) in the 2D fits. Examples of these
 636 templates are given in Fig. 27.

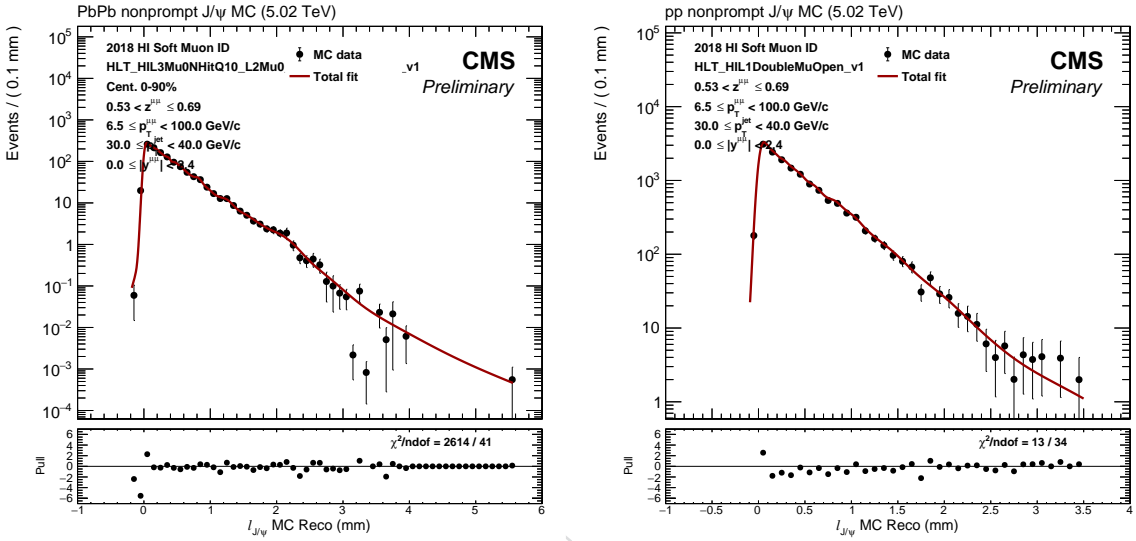


Figure 27: Templates of $F_{NonPrompt}(\ell_{J/\psi})$ distributions in pp and PbPb MC.

637 **7.2.3 Systematics on $\ell_{J/\psi}$ background distribution**

638 To take into account miss-modelling of the $\ell_{J/\psi}$ background distribution in Sec. 4.2.4 due to the
 639 choice of the fitting function, templates of the background distribution are created and used in
 640 the 2D fits instead of the PDFs. The $sPlot$ technique is used to unfold the signal and background
 641 $\ell_{J/\psi}$ distributions, which allows to use all the background events. The smoothen templates are
 642 created with RooKeysPdf [25] technique. In Fig. 28 examples of these templates in pp and PbPb
 643 data are shown.

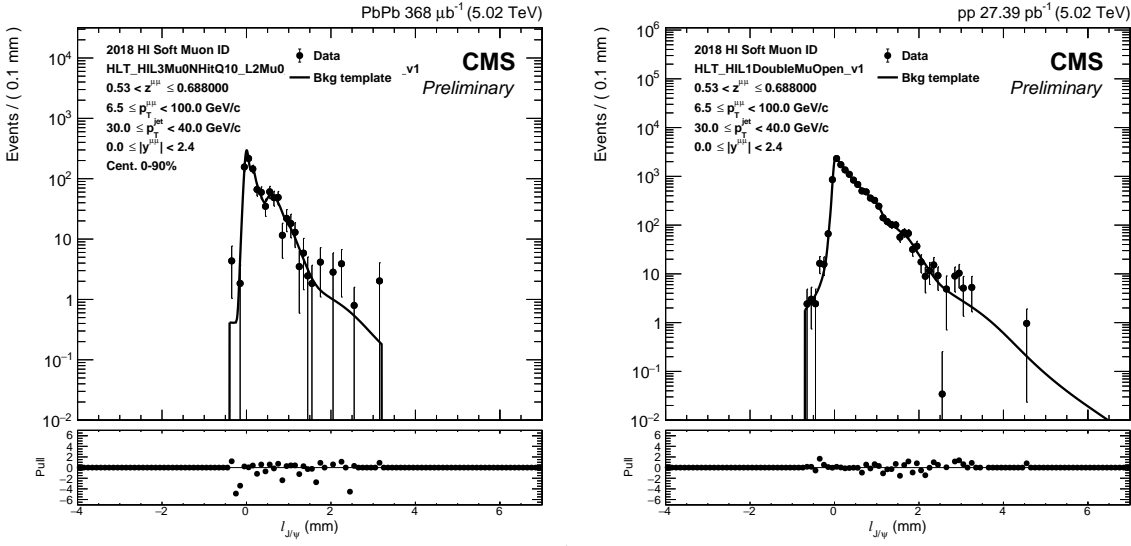


Figure 28: Templates of the $\ell_{J/\psi}$ background distributions in pp and PbPb data.

644 **7.3 Summary of signal extraction systematics**

645 7.4 Acceptance times efficiency uncertainty

646 The treatment of the T&P scaling factor uncertainties in this section were performed following
 647 the recommendations of the T&P team in the dilepton PinG found in <https://twiki.cern.ch/twiki/pub/CMS/HIMuonTagProbe/TnPHeaderFile.pdf> for PbPb and https://twiki.cern.ch/twiki/pub/CMS/HIMuonTagProbe/TnP_pp_summary_12.07.2019.pdf for pp.
 648 The muon trigger and muon ID T&P scaling factors are used to correct the nominal prompt J/ψ
 649 acceptance \times efficiency. In addition, for pp a scale factor is derived for the global reconstruc-
 650 tion, including both the tracking efficiency and stand-alone muon efficiency. For PbPb, only
 651 the tracking efficiency is evaluated.
 652
 653 The impact of the acceptance and efficiecy variations on the signal extraction on data is esti-
 654 mated using the MC samples. The procedure consist on applying the nominal 2D acceptance
 655 and efficiency correction to the reconstructed MC samples, in the same way as it is done on
 656 data, and simply counting the number of J/ψ in each analysis bin, $N_{\text{J}/\psi}^{\text{nominal}}$. Then the vari-
 657 ations of the corrections are applied one-by-one to obtain different acceptance and efficiency
 658 corrections. These corrections are applied to the reconstructed MC, and the number of J/ψ in
 659 each analysis bin is counted, $N_{\text{J}/\psi}^{\text{variation}}$. The systematic uncertainty of each T&P scaling factor
 660 is estimated from the difference $N_{\text{J}/\psi}^{\text{nominal}} - N_{\text{J}/\psi}^{\text{variation}}$ in MC.
 661
 662 The statistical and systematic uncertainties of the T&P scale factors are taken into account for
 663 the systematic uncertainty of the J/ψ acceptance \times efficiency. For each source we have two
 664 up/down statistical variation and two up/down systematic variations. In addition to that
 665 an uncertainty is assigned to the tag selection for all effeciecies. The tag trigger selections is
 666 varied from `HLT_HIL3Mu5_NHitQ10` to `HLT_HIL3Mu3_NHitQ10`.
 667 For the each component, the maximum deviation from the nominal value between the 2 up /down
 668 scale factors is taken as the systematic uncertainty ($\max(N_{\text{J}/\psi}^{\text{nominal}} - N_{\text{J}/\psi}^{\text{up}}, N_{\text{J}/\psi}^{\text{nominal}} - N_{\text{J}/\psi}^{\text{down}})$).
 669 The resulting systematic uncertainty from each scale factor is added in quadrature to the total
 670 systematic component of the systematic uncertainty on the J/ψ acceptance \times efficiency. The total
 671 systematic uncertainty related to the T&P scale factors, on the J/ψ acceptance \times efficiency, arises
 672 from the quadratic sum of the statistical and systematic components described above.
 673 In addition, the statistical uncertainty on the efficiency (due to limited MC statistics) is taken
 674 into account by performing 100 toy monte-carlo on both corrections. The efficiency value in
 675 each (p_T, y) bin in the acceptance corrections is randomly re-generated using a binomial func-
 676 tion where $(\epsilon)^{\text{new}} = \frac{\text{binomial}(N_{\text{tot}}, (\epsilon))}{N_{\text{tot}}}$. The value of the uncertainty is the RMS of the results
 677 obtained from the 100 toy monte-carlo (std dev. $(N_{\text{J}/\psi}^{\text{nominal}} - N_{\text{J}/\psi}^{\text{toy}, i}) ; i = 1..100$). The same
 678 procedure is done for the acceptance.
 679 Since this binomial function takes the number of events in the denominator of the efficeincy as
 680 input, it doesn't handle well weighted corrections. This is why it's better to refrain from using
 681 big weights e.g. NColl weights. Otherwise this uncertainty would be artificially negligible.
 682 As mentioned in Section refsec:efficiencies, unweighted corrections are used for the nominal
 683 results and the weighted efficeincies are used as systematic uncertainties for the mismodeling
 684 of the corrections.
 685 Finally, the total systematic uncertainty on the acceptance \times efficiency is the quadratic sum of
 686 the uncertainty related to the T&P scale factors, the statistical uncertainty on the acceptance \times efficiency
 687 and the uncertainty from the mismodelling of the kinematic distributions in MC. In Fig.29 a
 688 summary plot of the different sources of uncertainties and the total systematic uncertainty on
 689 the acceptance \times efficiency is presented for pp and PbPb in the nominal z bins.

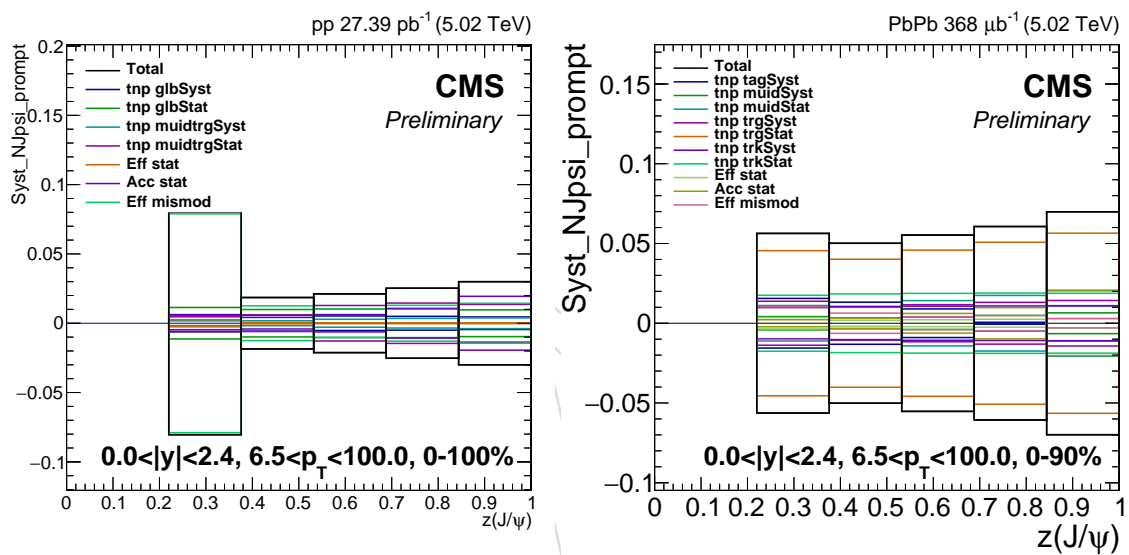


Figure 29: Systematic uncertainties of acceptance \times efficiency on prompt J/ ψ mesons in pp (left) and PbPb (right) rapidity. The values of the uncertainties are given relative to the nominal value.

690 7.5 Summary plots of systematic uncertainties on bidimensional fits

691 The plots in this section summarise the systematic uncertainties on the prompt and non prompt
 692 number of extracted J/ψ mesons due to the bidimensional fitting procedure for the different
 693 analysis bins. The corresponding tables with the values are given in App. ???. The systematic
 694 uncertainty of a given bin, corresponding to a given piece of the 2D fits, is computed as the
 695 maximum difference between the nominal result and the systematic tests. The total uncertainty
 696 for each bin is computed as the quadratic sum of the uncertainties of the different pieces. In
 697 Fig. 30, the values of the uncertainties are given relative to the nominal value in the nominal z
 698 bins.

699 7.5.1 Uncertainties on the number of extracted prompt J/ψ

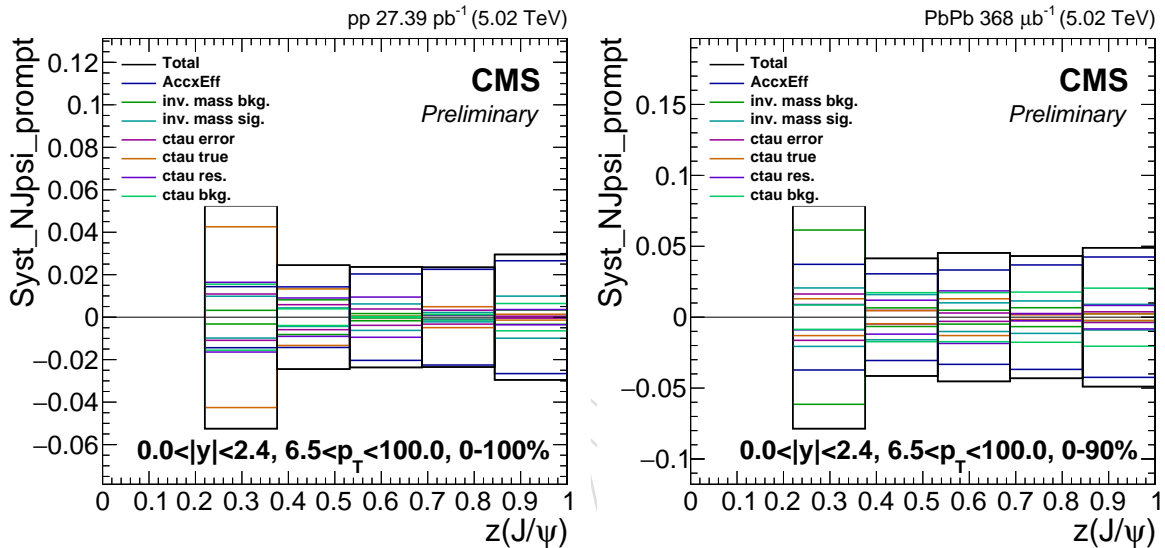


Figure 30: Systematic uncertainties of 2D fits for the number of extracted prompt J/ψ mesons in pp (left) and PbPb (right) collisions as a function of z . The values of the uncertainties are given relative to the nominal value.

700 8 Raw quarkonia yields

701 This section presents the “raw” J/ψ yields, meaning that the J/ψ are fully corrected while the be-
 702 fore unfolding of resolution effects is performed. The uncertainties presented are correspond-
 703 ingly only those of the quarkonia yield extraction. The unfolded results, including uncertainties
 704 on jet reconstruction effects are presented in 12.

705 8.1 Raw prompt J/ψ yields

706 Figure 31 shows the yield of prompt J/ψ as a function of z in pp and PbPb collisions, for the
 707 nominal jet p_T range of 30 – 40 GeV. The distributions show a radically different shape in pp
 708 and PbPb, which is due to the large combinatorial underlying event in the latter case. A J/ψ of
 709 modest p_T is very likely to overlap with a jet in this range, leading to a large peak at low z . One
 710 also expects a corresponding depletion of J/ψ at large values of z .

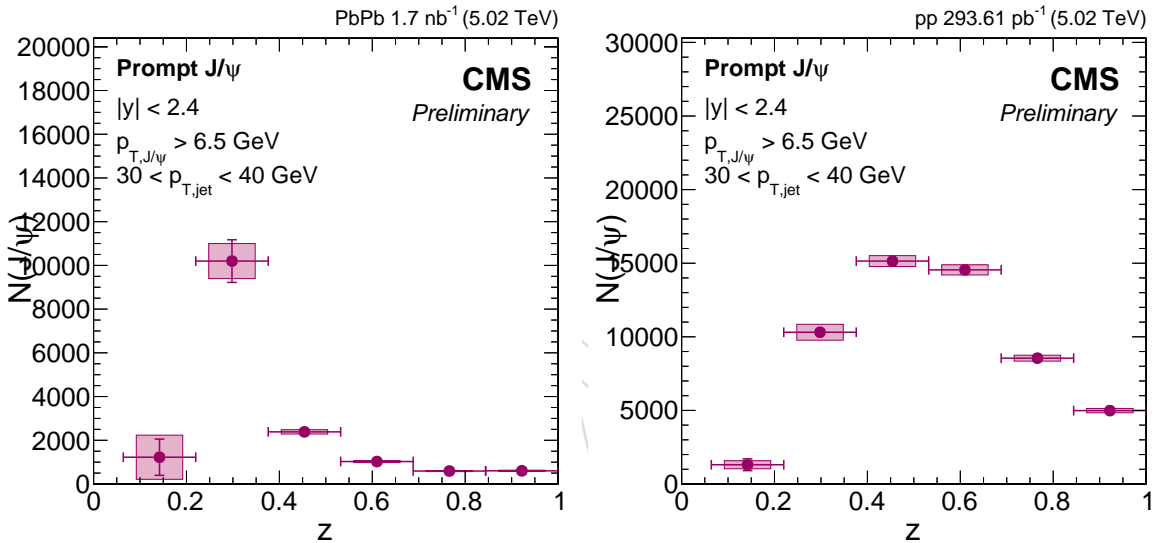


Figure 31: Prompt J/ψ yields, as a function of z , in pp collisions (left) and PbPb collisions (right), for the nominal jet p_T range of 30 – 40 GeV.

711 8.2 unfolding input

712 In order to unfold the effect of bin migration from finite jet resolution, we need to measure the
713 z distribution in lower and higher ranges of jet p_T . We measured in two “underflow” ranges of
714 jet p_T , 10–20 and 20–30 GeV, as well as two overflow ranges, 40–50 and 50–60 GeV.

DRAFT

715 8.2.1 Low- p_T (jet)

716 Figure 32 shows the yield of prompt J/ ψ as a function of z for in pp and PbPb collisions in the
 717 two jet p_T (jet) underflow bins.

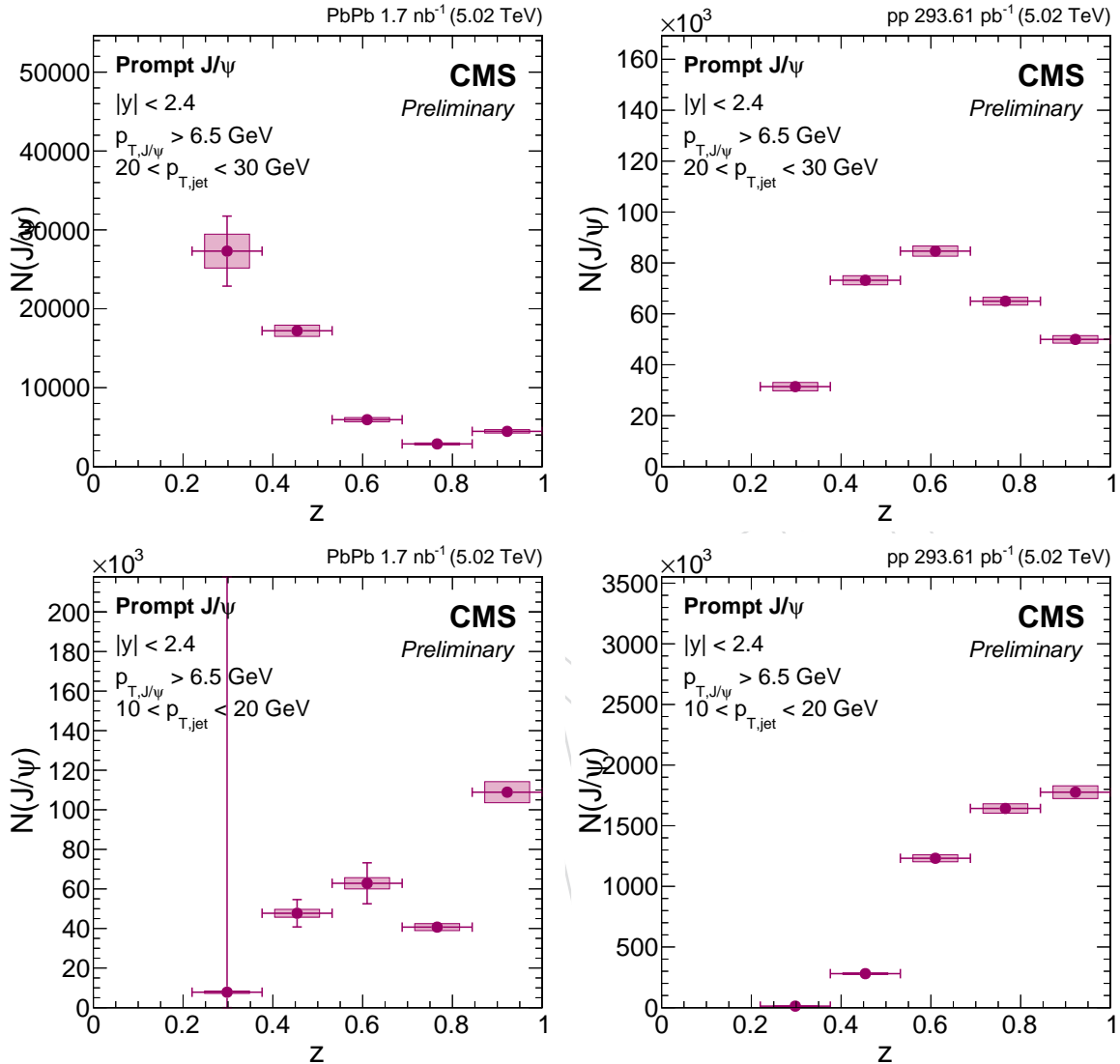


Figure 32: Prompt J/ ψ yield as a function of z in pp and PbPb collisions for $10 < p_T(jet) < 20$ and $20 < p_T(jet) < 30$ GeV.

⁷¹⁸ **8.2.2 high- p_T (jet)**

⁷¹⁹ Figure 33 shows the yield of prompt J/ ψ as a function of z for in pp and PbPb collisions in the
⁷²⁰ two jet p_T overflow bins.

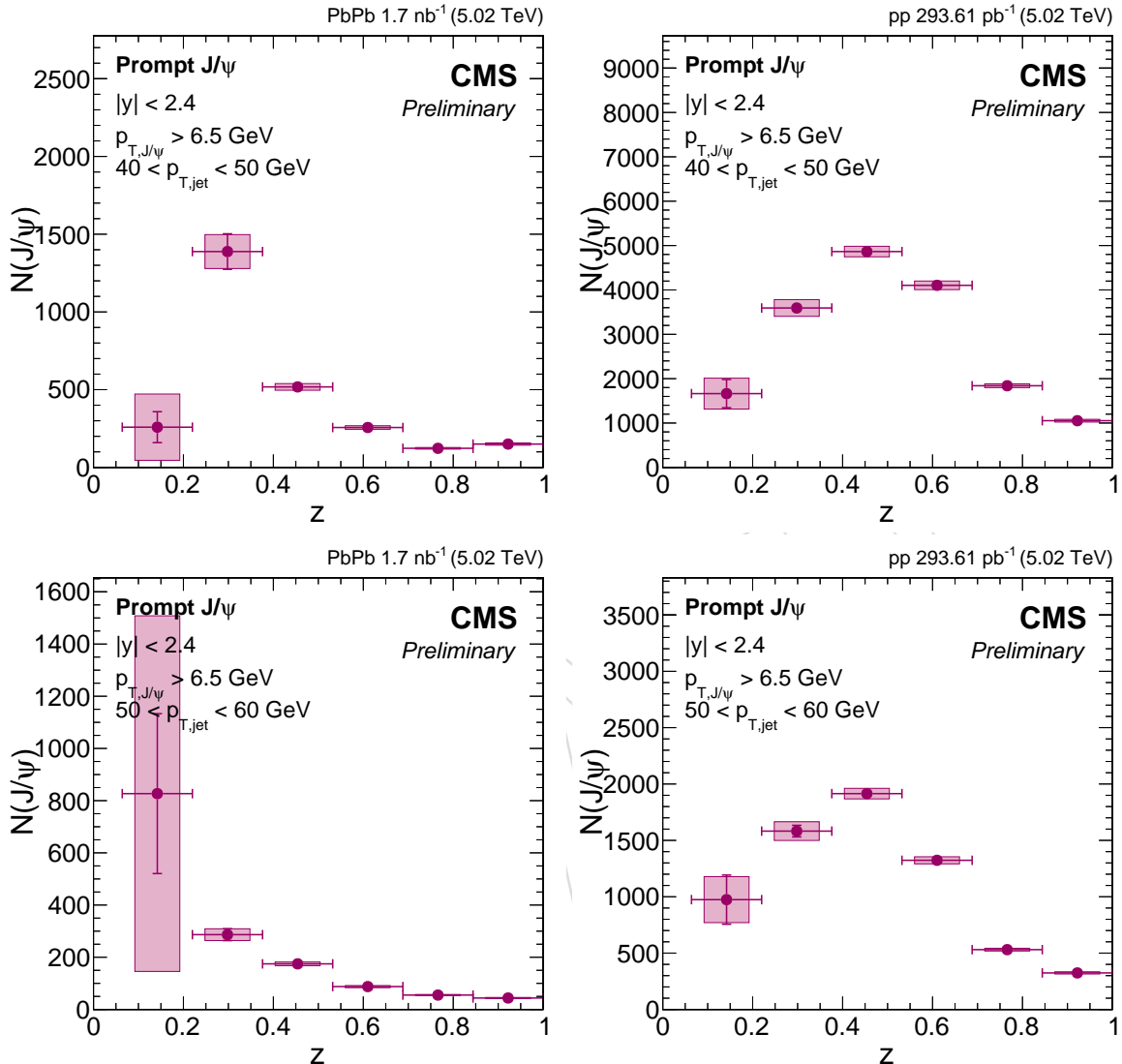


Figure 33: Prompt J/ ψ yield as a function of z in pp and PbPb collisions for $40 < p_T(jet) < 50$ and $50 < p_T(jet) < 60$ GeV.

721 9 Unfolding bin migration effects

722 The p_T resolution of inclusive jets in the range where we perform our measurement (30 – 40
 723 GeV), is around 15 – 20% in pp collisions and can reach around 50% in central PbPb collisions.
 724 The relatively wide resolution of jets, coupled with their steeply falling spectrum, causes sub-
 725 stantial bin migration. The net effect is somewhat smaller on the z distribution than on the p_T
 726 spectrum of jets itself, as the fragmentation function scales logarithmically with jet p_T , whereas
 727 the yield decreases with p_T according to a power law. However, the effect is by no means
 728 negligible, especially in PbPb collisions. This is demonstrated in Fig. 34, which compares the
 729 generator-level and measured z distributions from prompt MC. The correction of resolution ef-
 730 ffects requires the application of an unfolding method.

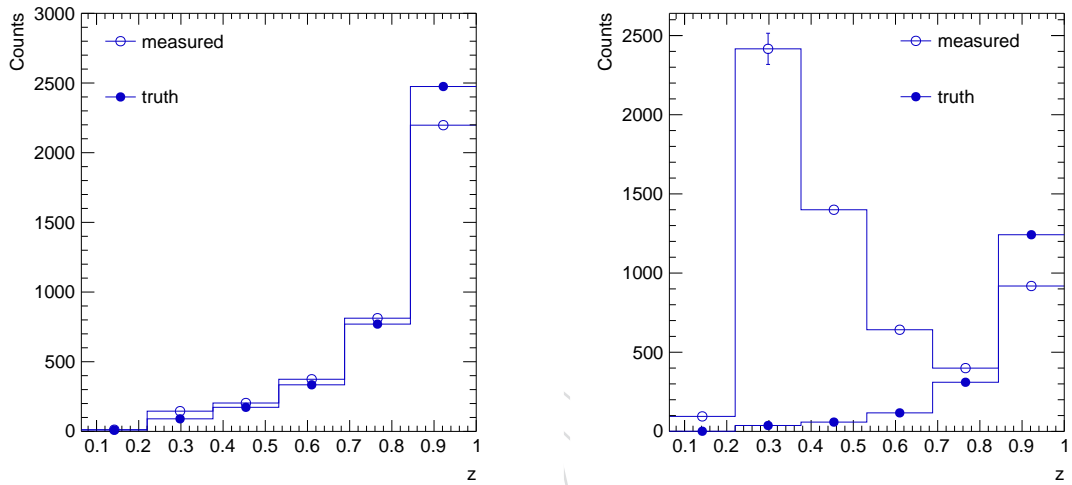


Figure 34: A comparison of the MC truth to the measured z distribution in pp (left) and PbPb collisions (right).

731 It is not sufficient to only correct for the resolution as a function of p_T . As discussed in Section 6,
 732 if one neglects the resolution of the J/ψ itself, the resolution is proportional to z . To take the
 733 dependence of the resolution on both p_T and z into account, we unfold in two dimensions. A
 734 framework for doing 2D unfolding is available in the RooUnfold package. We use D’Agostini’s
 735 iterative method, which is initialized with a “prior” guess of the unfolded distributions.

736 As is standard, the transfer matrix, which describes the detector response to the signal of inter-
 737 est, is taken from MC. The transfer matrix encodes the relationship between the measured and
 738 truth (labeled “gen” here) values. The transfer matrices for pp and PbPb are shown in Fig 35.
 739 The lower and upper limits of 6.5 and 60 GeV, respectively, were chosen such that 99% of jets
 740 with a gen p_T in the range of $30 < p_T < 40$ GeV are in the measured range. This was tested
 741 in both prompt and nonprompt PbPb MC. The depicted transfer matrices are normalized such
 742 that the sum over any gen bin, i.e., integrating over all measured bins, adds to unity. Hence
 743 this shows the probability of a given gen value to end up in any of the measured bins. For the
 744 case of 2D unfolding, the transfer matrix is a 4D histogram. In HIN-18-012 [26], it was found
 745 that to minimize finite bin size effects finer binnings are required on the gen axes, compared to
 746 the measured ones. We therefore increase the number of bins by a factor of 5 for the gen jet p_T
 747 axis and a factor of 8 for the gen z axis.

748 The unfolding procedure we use follows closely that used by LHCb. By default RooUnfold

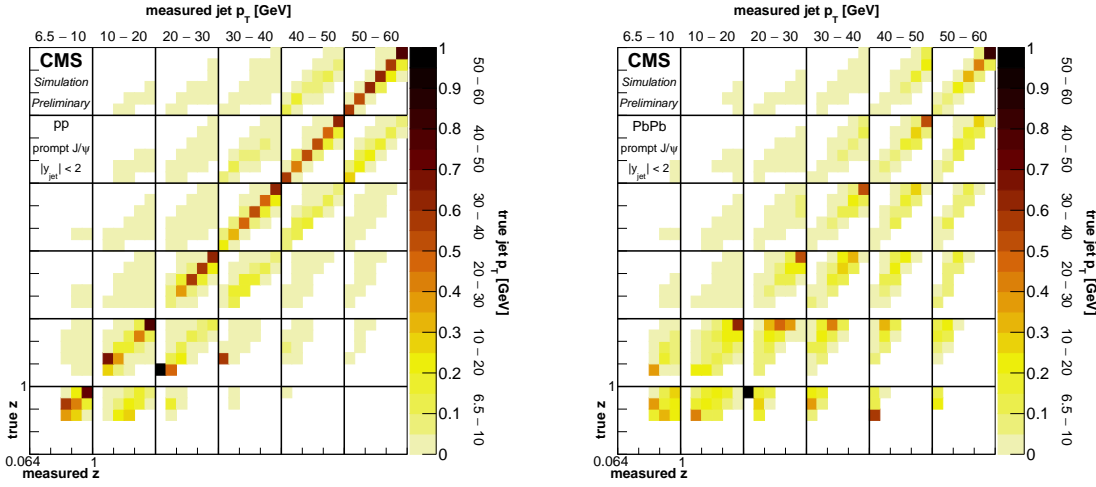


Figure 35: The 2D transfer matrix for bin migration in jet p_T in pp (left) and PbPb collisions (right).

749 initializes the unfolding with the MC truth distribution as the prior. However, such a choice can
 750 easily lead to a biased result, particularly in the case when the MC truth is a poor representation
 751 of the data. Following LHCb, we instead start with a prior which is flat in z , in order not to
 752 assume a shape that is peaked to large z , as in prompt MC, or peaked towards lower values,
 753 as in nonprompt MC. This is particularly important as the shape of the prompt MC does not
 754 reflect the shape in the prompt data. In the iterative method, the unfolded distribution at
 755 each iteration is then used as input to the next iteration. After performing a certain number
 756 of iterations, which is a tunable parameter, a new “super-iteration” is started. This means that
 757 we revert to the original prior, except the z distribution is initialized to match the output of the
 758 previous super-iteration. The number of super iterations is a second tunable parameter. The
 759 strength of the regularization depends on both the number of iterations and super-iterations.

760 We start by testing the unfolding machinery purely in MC. Using a self-same sample for the
 761 measured distribution and transfer matrix, the unfolding performs perfectly. A less trivial test
 762 is performed by splitting the same into two equal sized statistically independent pieces. In
 763 this first test, which we use to understand the qualitative features of the unfolding, we fix the
 764 number of iterations to three, and study the behavior as a function of the number of super-
 765 iterations. This choice of three iterations was inherited from the LHCb measurement and from
 766 HIN-18-012 [26], where it was found to give reasonable results for pp collisions. Figure 36
 767 shows the results of the unfolding for the pp and PbPb prompt J/ψ MC. The left panels show
 768 the distributions, while the right panels show the ratio of the unfolding output for selected
 769 super-iterations to the measured distributions. The success of the unfolding can be gauged
 770 by comparing these curves to the ratio of the truth to measured distributions, which is also
 771 shown. For the pp MC, the measured distribution is already relatively close to the truth one.
 772 After one super-iteration the unfolded result is quite close to the truth one, removing most of
 773 the bin migration effect. Further super-iterations actually degrade the performance, inducing
 774 an oscillatory behavior in the results.

775 Looking at the prompt MC in PbPb, we see that the measured value is quite far from the truth.
 776 The truth is peaked towards large z , i.e., the J/ψ in the MC are isolated. When super-imposed
 777 on the large and fluctuating PbPb underlying event, we see that these isolated J/ψ often appear
 778 at low z . The overall yield in the measured distribution is larger, as more jets tend to migrate

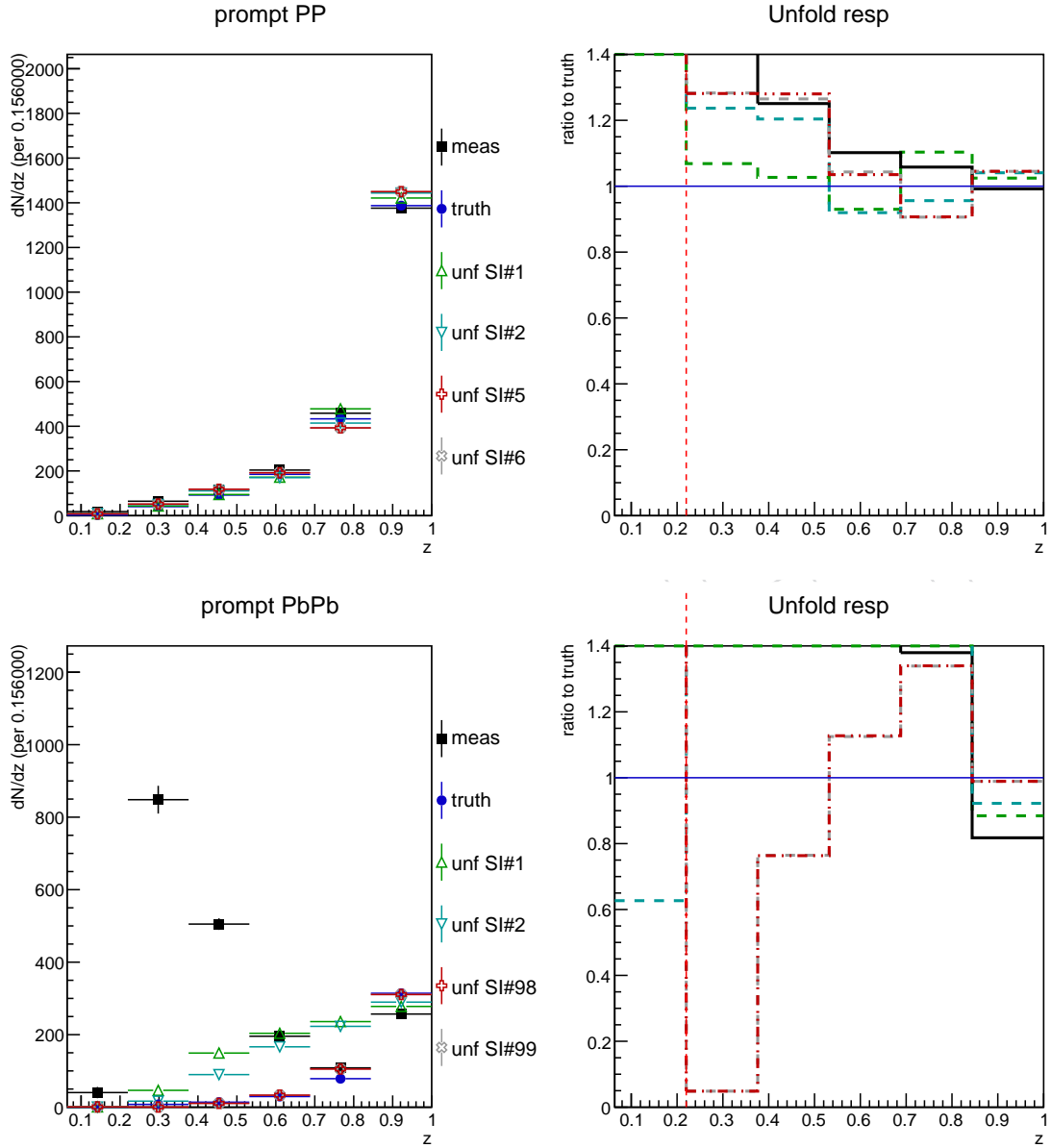


Figure 36: Closure test of the unfolding in MC for prompt J/ψ in pp (top) and $PbPb$ (bottom) collisions. The left set of panels shows the truth, measured and unfolded z distribution after selected super-iterations, while the right shows the ratio of these to the true z distribution.

779 into the nominal jet p_T bin, than out of it, due to the steeply falling jet p_T spectrum. The large
 780 peak at low z already disappears after a single super-iteration. However, we found that one
 781 needs to go to a much larger number of super-iterations to recover the shape of the truth
 782 distribution. For illustration we show the result 98 and 99 super-iterations. The unfolding
 783 converges to a stable result, which is also the case for a large number of (super-) iterations in
 784 pp. The general features of the truth distribution is recovered, although the agreement is not
 785 perfect.

786 At this point we realized that a more careful optimization of the regularization parameters
 787 is necessary. We considered that it might be useful to tune not only the number of super-
 788 iterations, but the number of standard iterations, as well. Further, we realized that the oscil-
 789 latory behavior caused by under-regularization, as clearly observed in the pp MC test, should
 790 depend on the statistical precision of the measured sample. Therefore, we had better try to
 791 emulate the statistical precision of the data. To do so, we smeared each jet p_T and z bin in the
 792 measured distribution in MC according the relative uncertainty from the same bin in data. We
 793 then ran the unfolding with several choices for the number of iterations per super-iteration.
 794 Figure 38 (left) shows the χ^2 between the measured and truth distributions for three choices of
 795 number of iterations, 3, 5, 7, 10 and 20, as a function of the number of super-iterations. When
 796 computing the χ^2 , only the statistical uncertainty of the truth is taken into account. For the
 797 initial choice of three iterations, the best agreement is achieved after 25 iterations, after which
 798 the performance degrades.

799 We also considered that the optimal choice of the regularization parameters could depend on
 800 the shape of the measured distribution. To test this hypothesis, we performed the unfolding on
 801 the nonprompt MC, where the z distribution looks very different. The true z distributions are
 802 shown in Fig. 37. The corresponding χ^2 scan is shown in the right panel of Figure 38. Here
 803 it appears that a larger number of iterations improves the performance. The best performance
 804 was achieved with 10 iterations, which is the most that we've tried. The best number of super-
 805 iterations was smaller for the prompt case, showing a shallow minimum around 9.

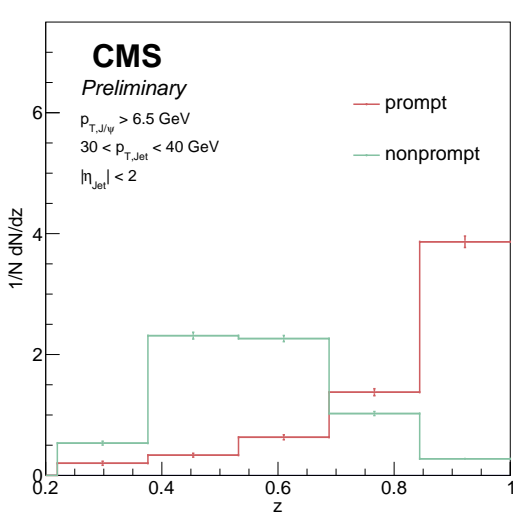


Figure 37: MC truth distributions of z in pp for prompt and nonprompt

806 The z distributions for the best number of iterations (3 for prompt and 10 for nonprompt)
 807 are shown for several super-iterations, up to the best one (25 super-iterations), in Fig 39. For

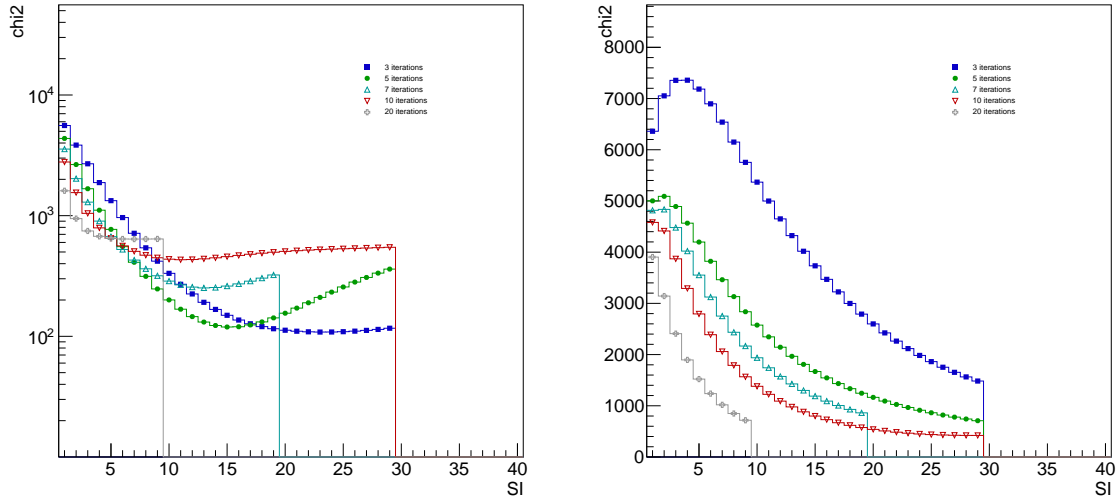


Figure 38: χ^2 of the unfolding in MC for prompt J/ψ in $PbPb$ collisions for prompt (left) and nonprompt (right).

808 prompt MC, we see very good agreement between the unfolded and truth distribution for the
 809 best choice of regularization parameters. For the nonprompt case, although the main features
 810 of the truth distribution are still recovered, there is somewhat poorer agreement between the
 811 unfolded and truth distributions. This may indicate that the best choice for regularization
 812 parameters obtained so far, may still be sub-optimal. We still plan to explore more choices for
 813 these parameters to see if better performance can be achieved.

814 A χ^2 scan was also performed for the pp MC, as shown in Fig. 40. For the prompt data, the best
 815 performance was achieved for 5 iterations, with only 1 super-iteration. For the nonprompt MC,
 816 a larger number of iterations is preferred. The best performance was achieved with 10 iterations,
 817 the largest number tried so far. As was the case for the prompt MC, the best performance was
 818 obtained without any additional super-iterations. Fig. 41 shows the z distributions, using 3 and
 819 10 iterations for prompt and nonprompt MC, respectively. The unfolded distributions compare
 820 reasonably well with the truth ones for the curves corresponding to one super-iteration.

821 The same procedure is also done in two centrality ranges: 0-20% and 20-90%. The Closure tests
 822 for central $PbPb$ collisions are shown in Fig 42. Where 2 iterations and 28 super-iterations were
 823 found to be the best option for prompt and 10 iterations and were chosen for nonprompt. The
 824 tests for the peripheral collisions are shown in Fig 43. 21 super-iterations of 2 iterations are
 825 chosen for prompt and 13 super-iterations of 10 iterations were chosen for nonprompt.

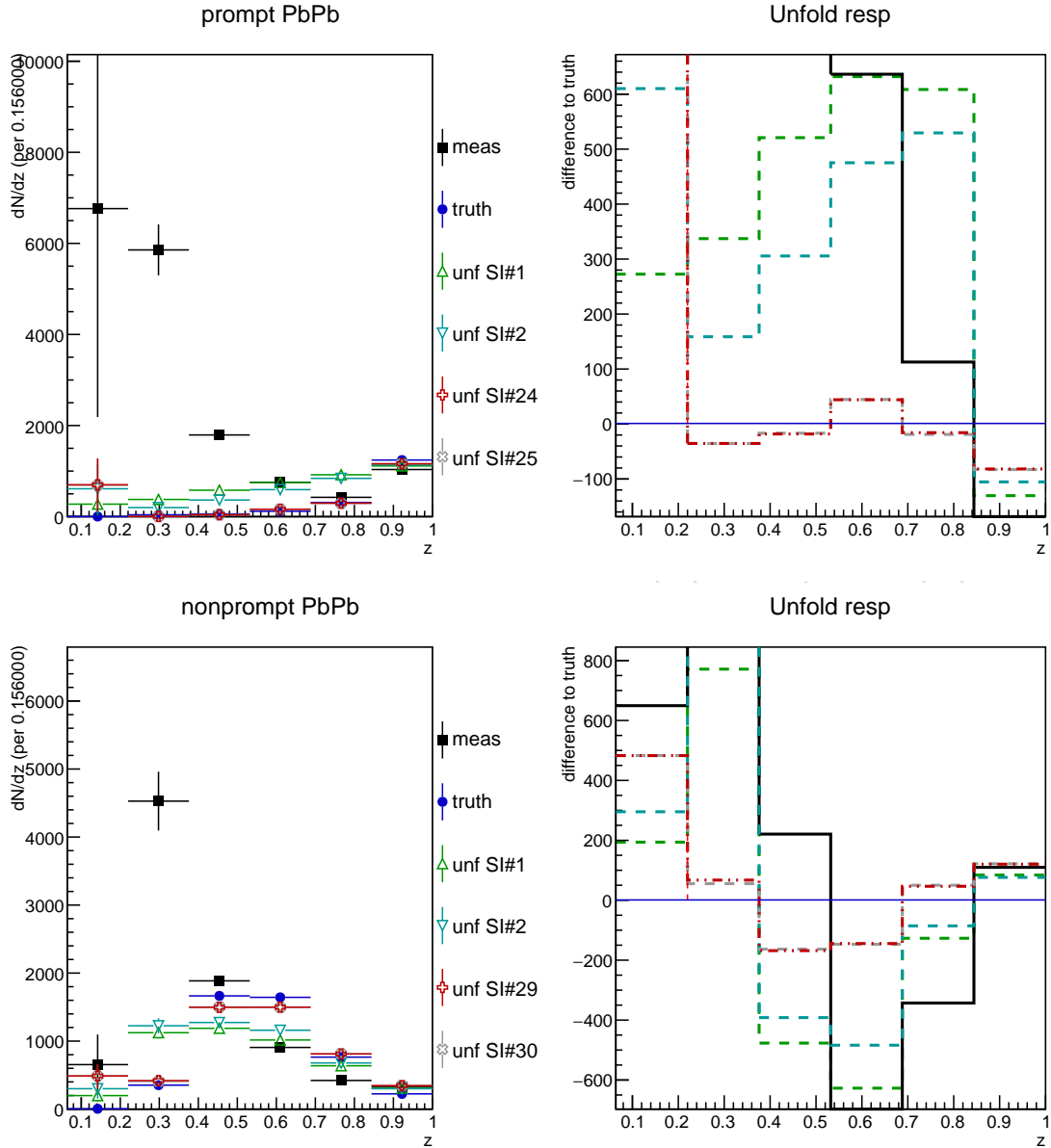


Figure 39: Closure test of the unfolding in MC for prompt J/ψ in $PbPb$ collisions for prompt (top) and nonprompt (bottom). The left set of panels shows the truth, measured and unfolded z distribution after selected super-iterations, while the right shows the difference between these and the true z distribution.

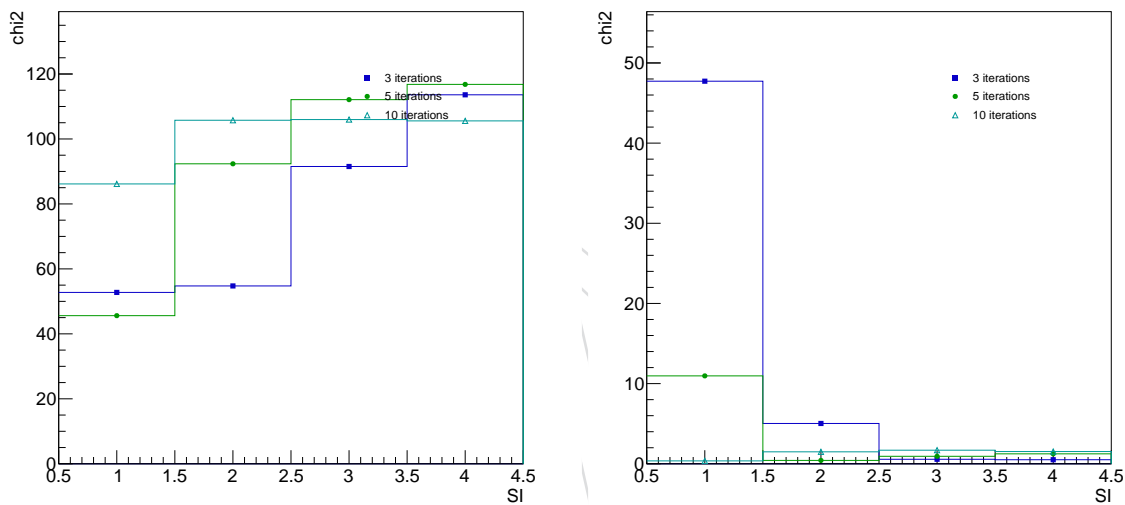


Figure 40: χ^2 of the unfolding in MC for prompt J/ ψ in pp collisions for prompt (left) and nonprompt (right).

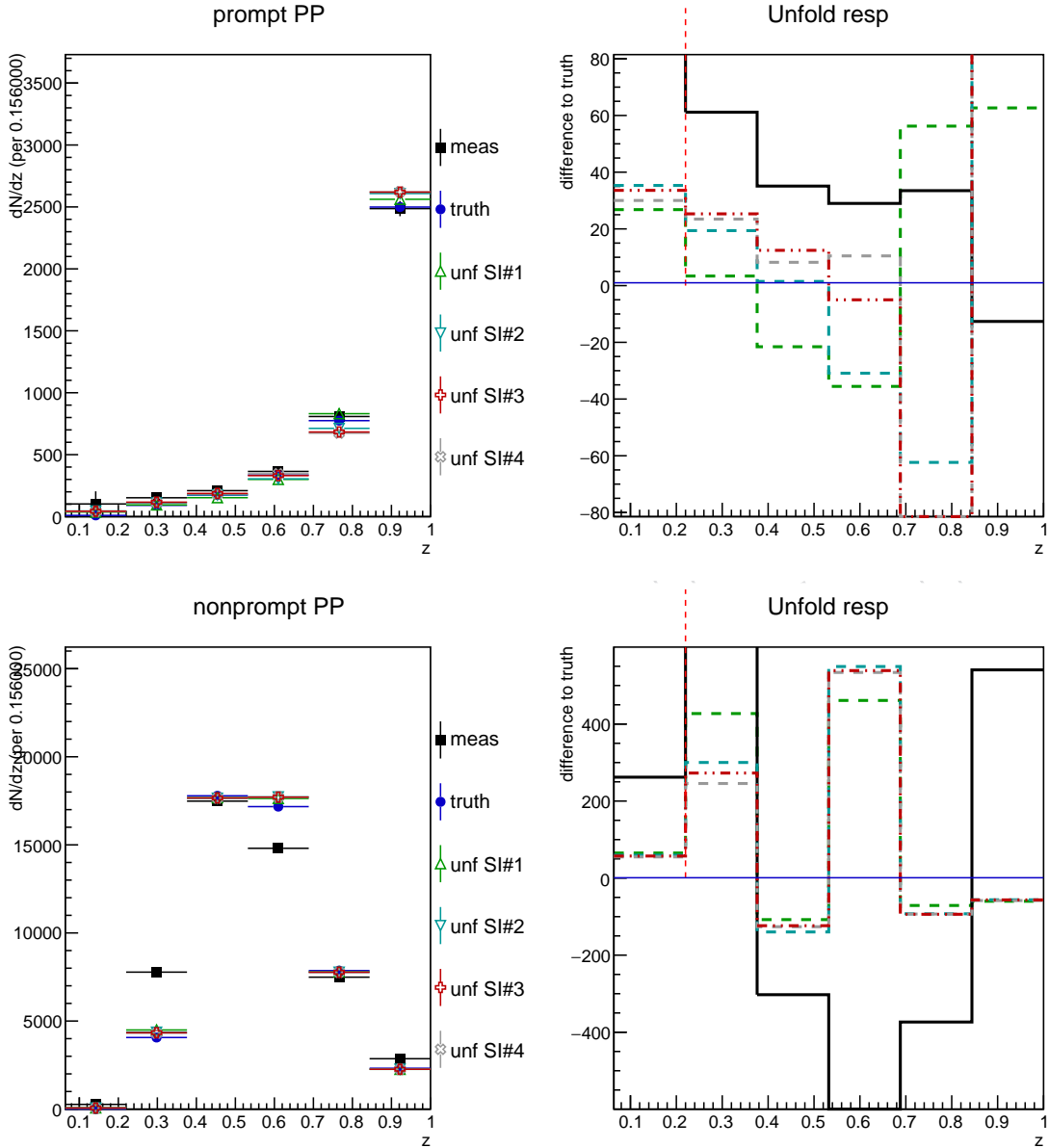


Figure 41: Closure test of the unfolding in MC for prompt J/ψ in pp collisions for prompt (top) and nonprompt (bottom), which have been smeared to emulate the statistical precision of read data. The left set of panels shows the truth, measured and unfolded z distribution after selected super-iterations, while the right shows the difference these and the true z distribution.

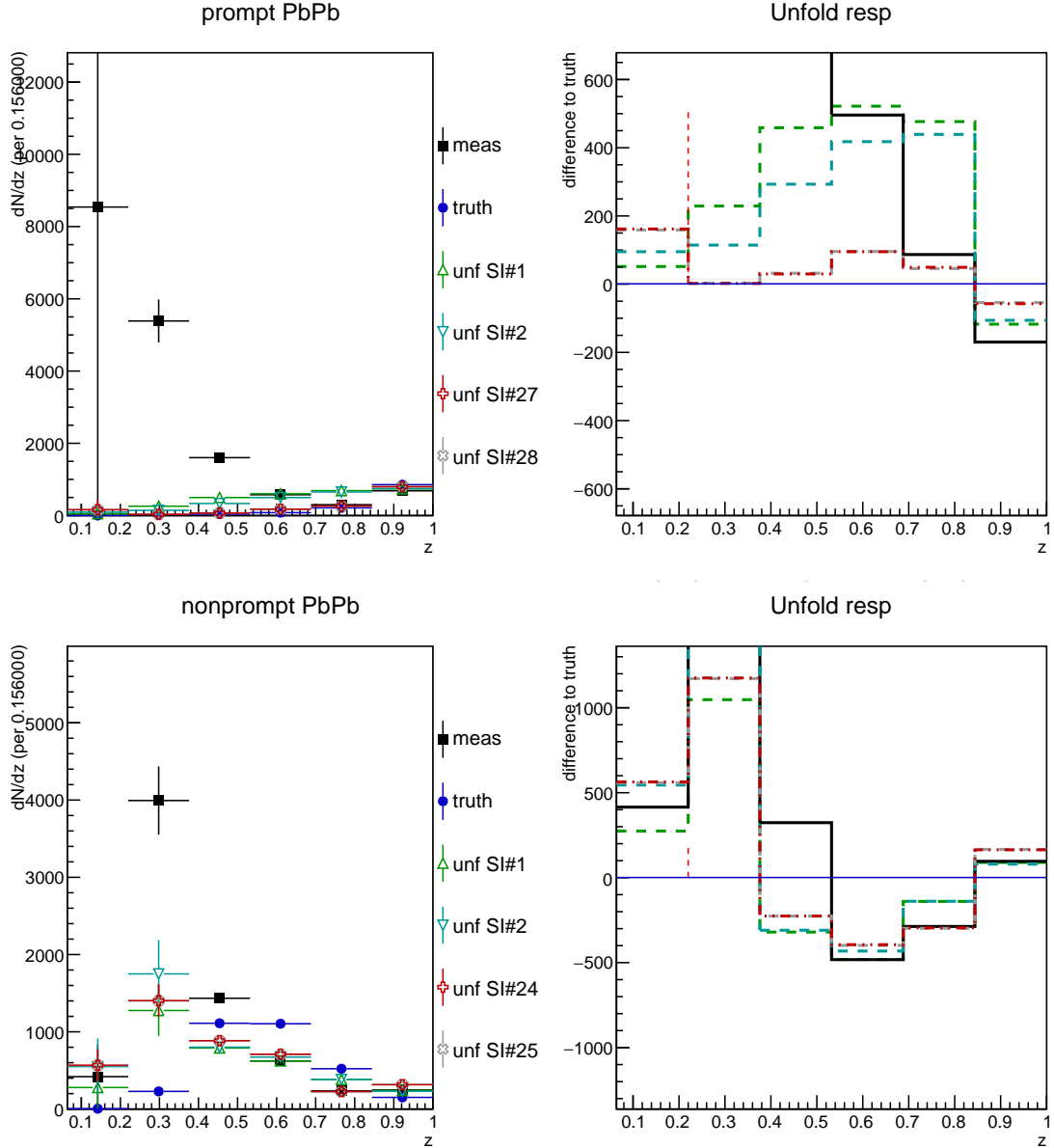


Figure 42: Closure test of the unfolding in MC for prompt J/ψ in central PbPb collisions for prompt (top) and nonprompt (bottom). The left set of panels shows the truth, measured and unfolded z distribution after selected super-iterations, while the right shows the difference between these and the true z distribution.

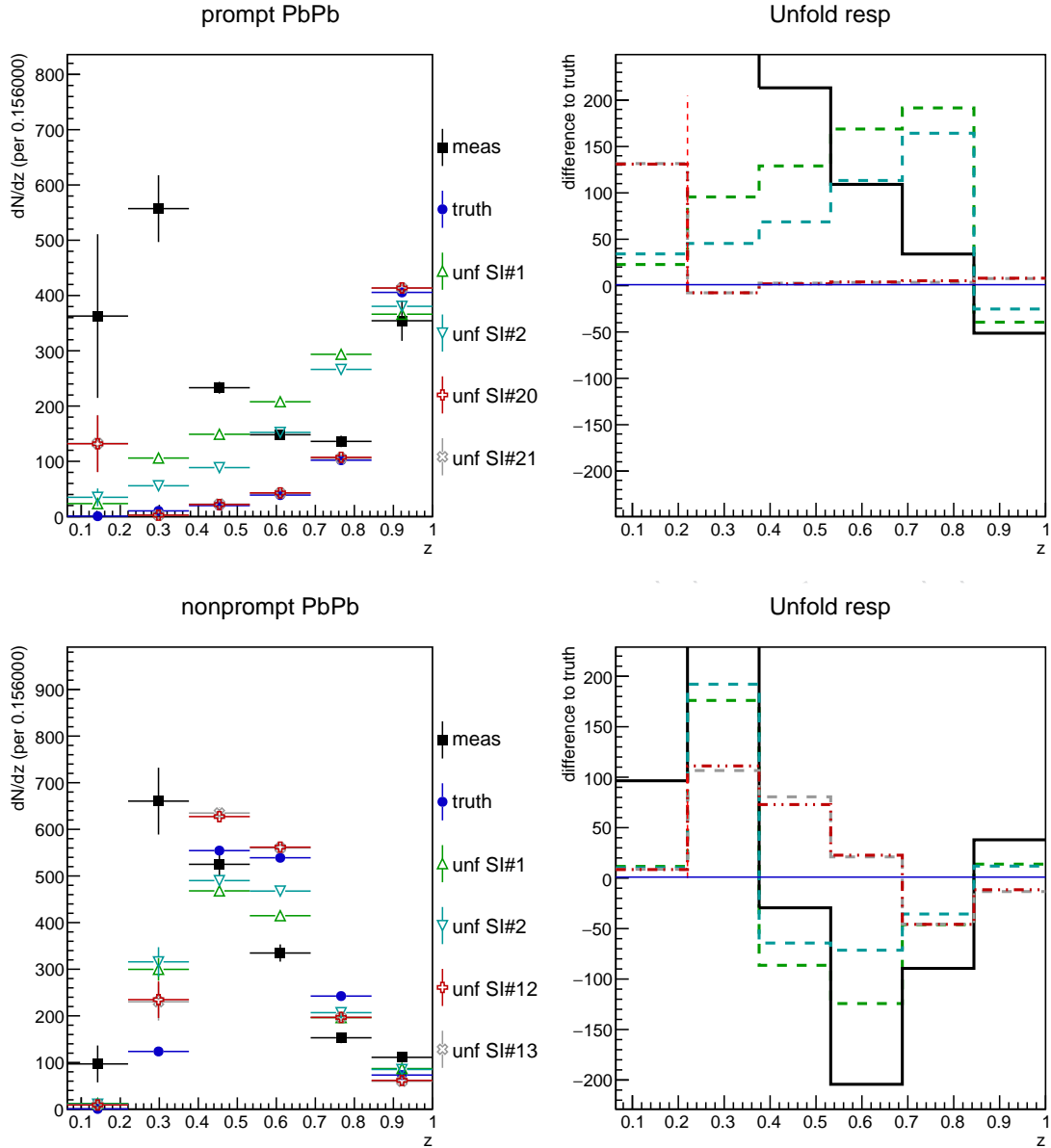


Figure 43: Closure test of the unfolding in MC for prompt J/ψ in central PbPb collisions for prompt (top) and nonprompt (bottom). The left set of panels shows the truth, measured and unfolded z distribution after selected super-iterations, while the right shows the difference between these and the true z distribution.

826 Figure 44 shows the unfolding procedure applied to the prompt J/ψ data in pp and PbPb col-
827 lisions. The transfer matrix is smeared to account for the data-to-simulation difference in jet
828 energy resolution, as described in Section 6.2. The best regularization settings from the test
829 with the smeared prompt MC are used. In pp, where the number of iterations is set to 3, the
830 majority of the difference between the unfolded and truth distributions is already apparent
831 after the first super-iteration (which is the selected setting). Further super-iterations change
832 the result somewhat, but are changing very little by super-iteration 6, which is also the case
833 in the MC test. PbPb also shows an evolution that is qualitatively similar to the MC. With the
834 selected setting of 3 iterations, the large peak at low z is already removed by the end of the first
835 super-iteration. As in MC, the PbPb data require a larger number of super-iterations to become
836 stable, but no longer change by the chosen setting of 25 super-iterations.



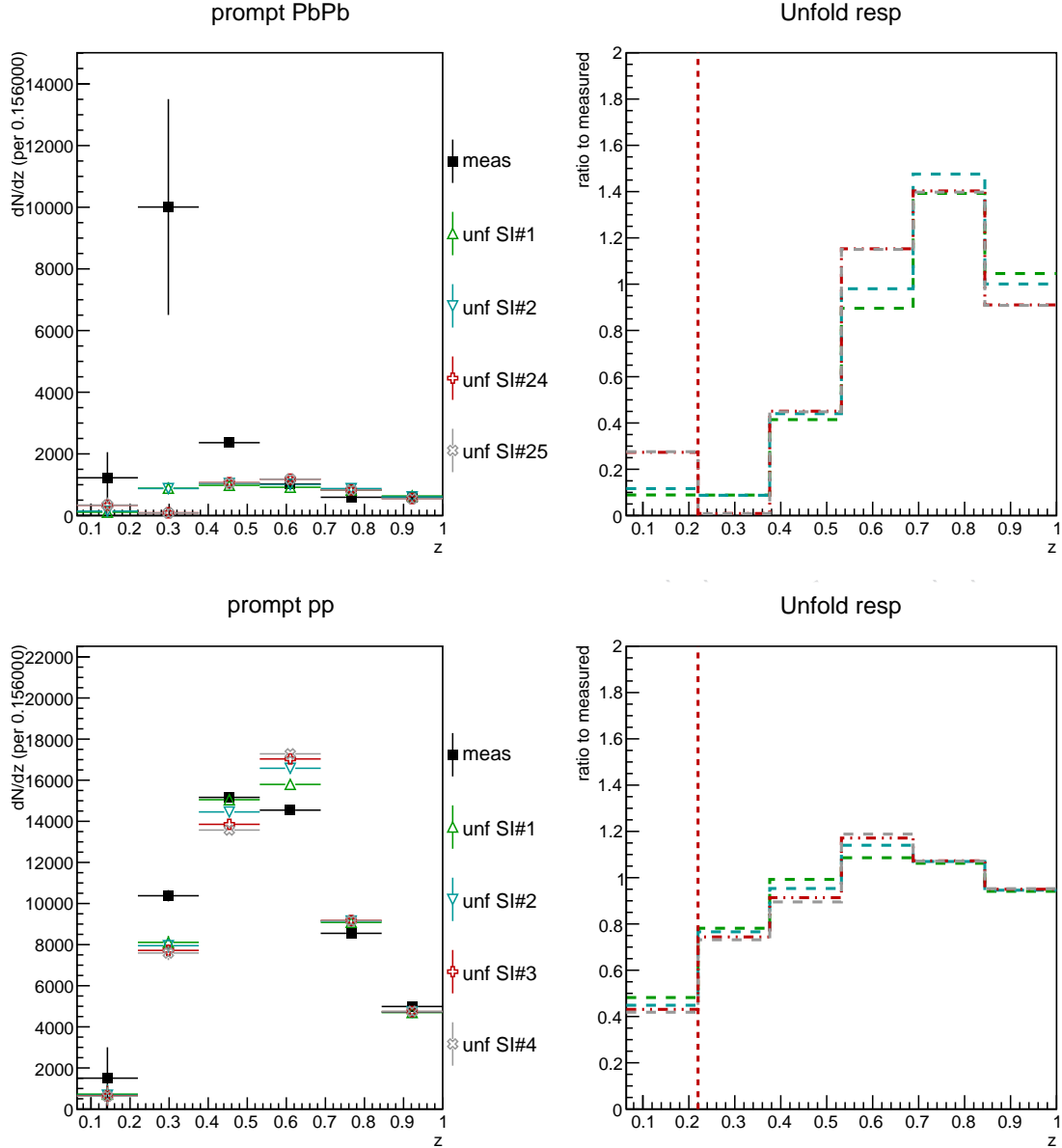
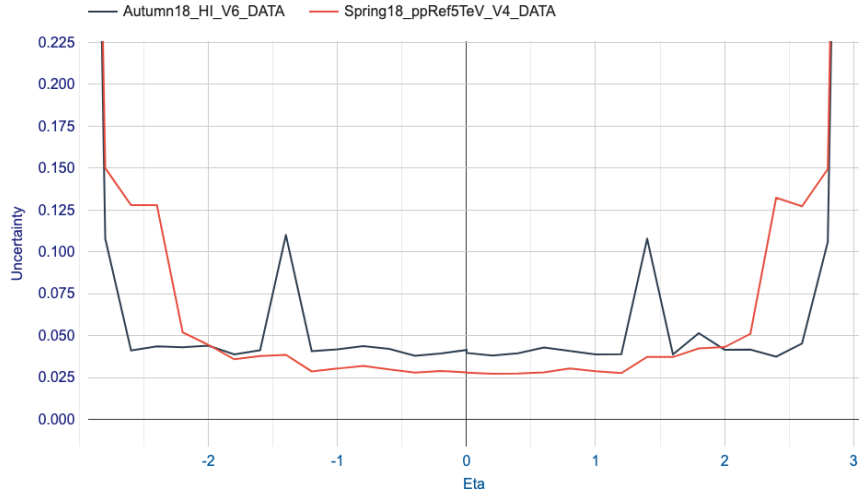


Figure 44: Unfolding of prompt J/ψ data for pp (top) and $PbPb$ (bottom). The left panels show the measured z distributions in the nominal jet p_T bin, and the unfolded ones after various numbers of super-iterations, as indicated in the leged. The right panels show the ratios of the unfolded distributions to the measured ones.

837 10 Jet-related uncertainties

838 The jet energy scale uncertainties were evaluated by the heavy-ion jet reco group, using dijet
 839 and photon+jet balancing studies for both the pp and PbPb datasets [27], using the methods
 840 described in Ref. [23]. The uncertainty at $p_T = 30\text{ GeV}$, as a function of η is shown in Fig. 45. In
 841 pp, the uncertainty varies from about 3 – 4%. In PbPb the uncertainty is around 4%, except in
 842 the barrel-endcap transition region ($1.2 < \eta < 1.6$), where it reaches around 10%.



843 Figure 45: Uncertainty on the jet energy scale, as a function of η , in pp and PbPb data.

844 The uncertainty does not apply to the fraction of the jet that is comprised of the muons from
 845 J/ψ , as the muon kinematics are much more precisely known. The J/ψ component of jet does
 846 not lead to any uncertainty on the jet energy scale, as the $J/\psi p_T$ enters both the numerator and
 847 denominator in the ratio z . The J/ψ does of course have a finite resolution, but this is small
 848 compared to the relatively poor resolution of the "jetty" component, i.e., the part of the jet
 849 whose momentum is given by $1 - z$.

850 The variation of the jet energy scale is propagated by shifting the reconstructed jet p_T values
 851 in the transfer matrix used in the unfolding. For illustrative purposes, in Fig. 46 we show the
 852 effect of the energy scale shift on the measured z distribution, for the nominal jet p_T selection.
 853 Rather than perform the fits to extract the prompt yield, we simply select on J/ψ in the mass
 854 range of 3 – 3.2 GeV, without applying any lifetime selection.

855 To propagate the uncertainty from jet p_T resolution, the data/MC scale factors discussed in Sec-
 856 tion 6.2 are according to their uncertainties (provided by the JetMET group) and the unfolding
 857 is repeated. For the 2018 data, the uncertainty on these scale factors ranges from about 3% in
 858 mid-rapidity to about 7%, for the endcap and transition regions. For 2017 data, the uncertainty
 859 is comparable in the barrel region (2 – 4%, depending on η), but is larger in the endcap and
 860 transition regions, where it varies from 10 – 20%, depending on η . The contribution to the jet
 861 resolution from the PbPb underlying event is estimated by varying the centrality definition in
 862 MC, as described in Section 6.2. The centrality is shifted by 5% for the nominal results. 0%
 863 and 10% are taken as uncertainties. Fig. 47 shows the unfolded z distributions with the three
 864 centrality shifts.

865 An uncertainty is attributed to the regularization strength used in the unfolding by changing
 866 from the best settings derived from prompt J/ψ MC, to the ones derived from nonprompt J/ψ

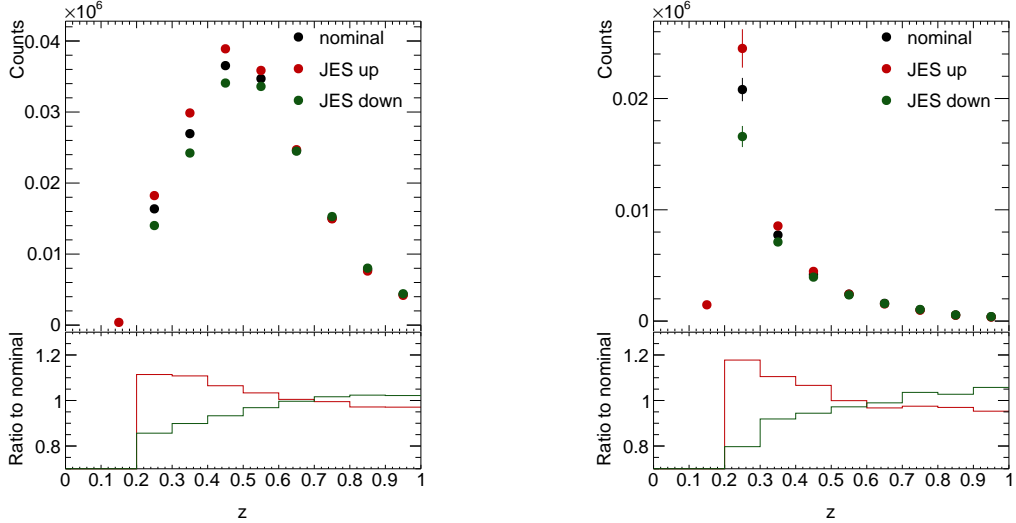


Figure 46: Effect of shifting the JES within its uncertainties in pp (left) and PbPb (right) data. Rather than extracting the yield from fits, we restricted the invariant mass of the J/ψ candidate to $3 - 3.2$ GeV.

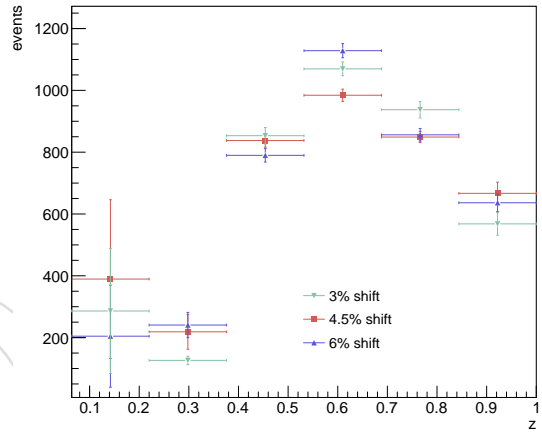


Figure 47: Unfolded results with different MC centrality shifts in prompt data for pp (left) and PbPb collisions (right).

866 MC, as shown in Fig. 48. These settings are explained in Section 9.

867 The statistical uncertainty on the transfer matrix is also estimated. This is done by producing
 868 100 toy variations of the MC transfer matrices by smearing the bin contents by their statistical
 869 uncertainties (exactly as done for the acceptance x efficiency errors). The uncertainty is shown
 870 in Fig 49 for pp and PbPb.

871 Finally, an uncertainty is assigned on the shape of the prior distribution. This is done by relax-
 872 ing the assumption of a prior that is flat in z , which is quite far from the data, to the z shape
 873 taken from nonprompt MC, which is closer to the shape found in pp data by LHCb and in
 874 HIN-18-012. Fig fig:priorSyst shows the difference between the unfolded distributions for the
 875 two prior choices.

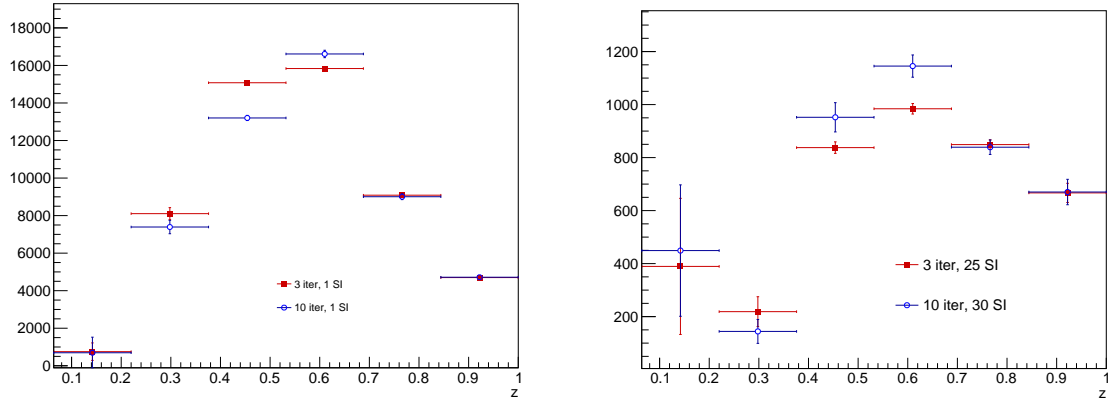


Figure 48: Unfolded results with different regularization settings in prompt data for pp (left) and PbPb collisions (right).

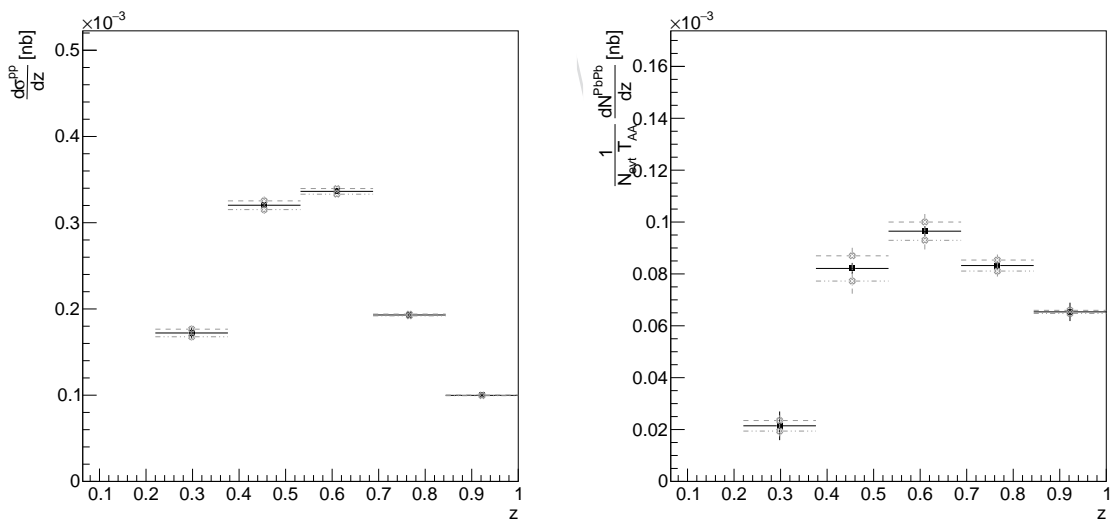


Figure 49: Systematic uncertainties coming from the statistical uncertainty on the response matrix for pp (left) and PbPb (right)

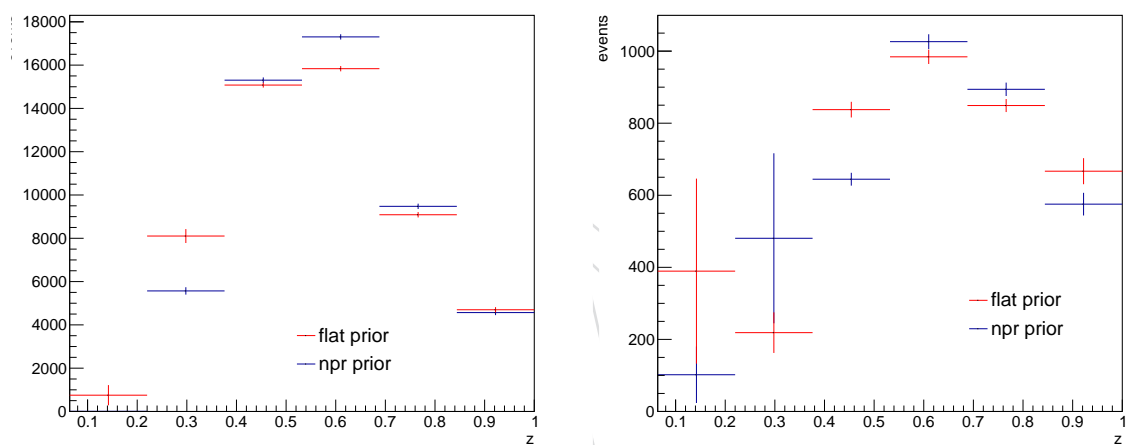


Figure 50: Systematic uncertainties coming from the uncertainty on the shape of the prior for pp (left) and PbPb (right)

876 11 Summary of systematic uncertainties

877 The systematic uncertainty is broken down into several sources shown in Fig. 51. The relative
 878 uncertainties are shown in Fig. 52 All sources of systematic uncertainty on the J/ψ signal ex-
 879 traction, which were presented in Section 7, are summed together in quadrature. The various
 880 subsources of jet related uncertainties, presented in Section 10, are shown individually on the
 881 plot.

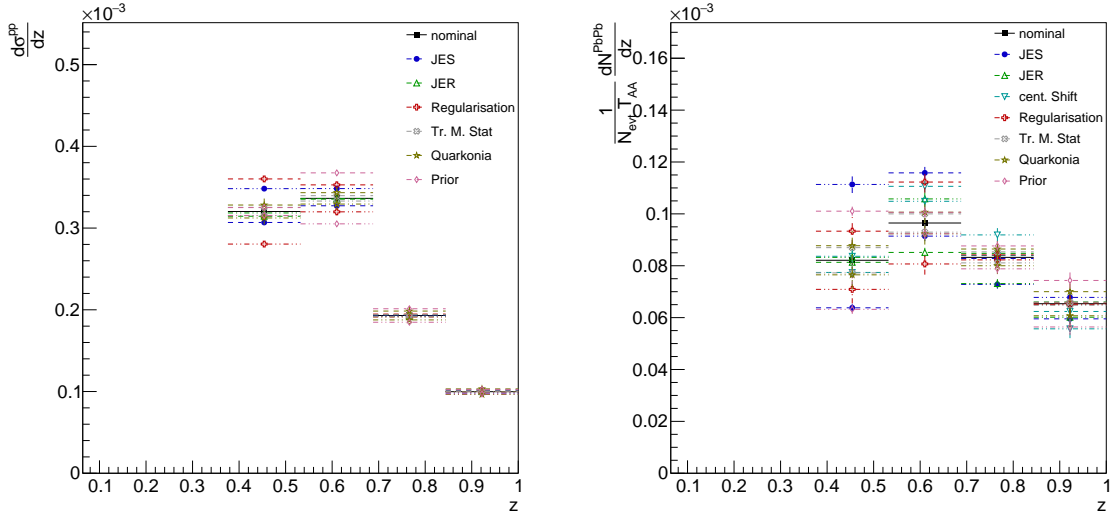


Figure 51: Systematic uncertainties for prompt J/ψ mesons in pp (left) and PbPb (right) colli-
 sions as a function of z .

882 In addition to the z -dependent uncertainties, there is an overall normalization uncertainty for
 883 the pp and PbPb data. The uncertainty on the pp data from the luminosity is 3.5%. The uncer-
 884 tainty on the PbPb data comes from the T_{AA} , as evaluated in a Glauber model and amounts to
 885 2.2%.

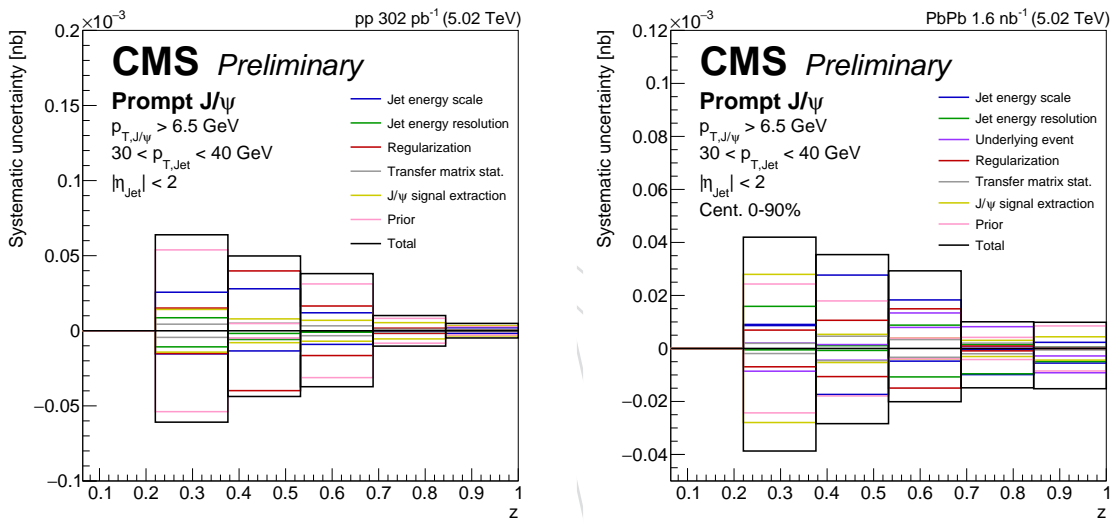


Figure 52: Absolute systematic uncertainties for prompt J/ψ mesons in pp (left) and PbPb (right) collisions as a function of z.

886 12 Results

887 Figure 53 shows the yield of prompt J/ψ as a function of z for pp and PbPb after applying the
 888 unfolding. The mean of the z distribution in PbPb collisions is evidently shifted to larger values
 889 of z . A possible explanation would be that J/ψ with low z , which should on average be created
 890 late in the shower evolution, come from jets that have experienced a high degree of quenching.
 891 Isolated J/ψ , on the other hand, should not experience energy loss, as the J/ψ itself is a color
 892 neutral bound state. The Debye screening effects that are thought to dominate the suppression
 893 of J/ψ at low momentum, maybe be less relevant than jet queching at large momentum. A
 894 comparison between the R_{AA} in central (0-20%) and mid-central events (20-90%) is shown in
 895 Fig. 54.

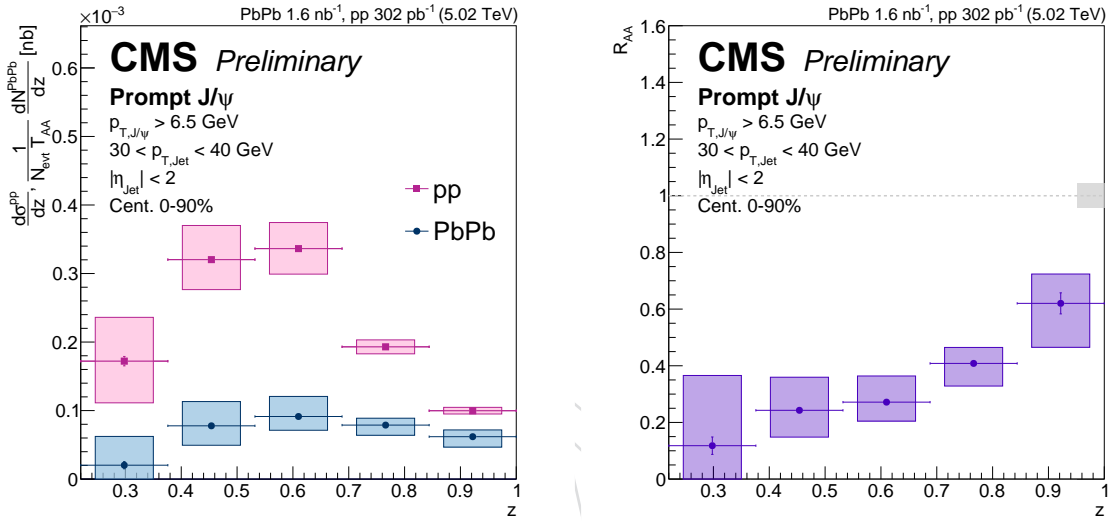


Figure 53: Unfolded prompt J/ψ z distributions in pp and $PbPb$ collisions (left) and the R_{AA} (right).

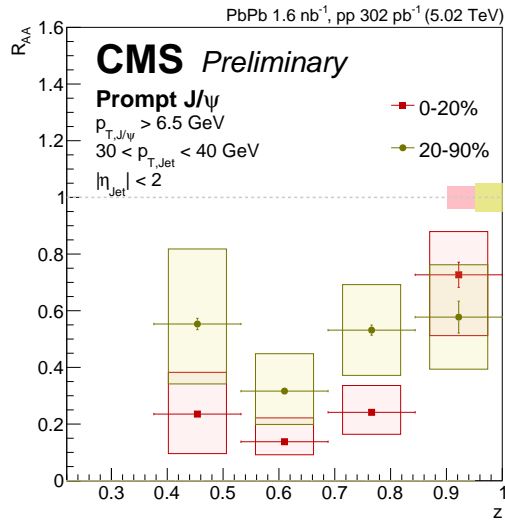


Figure 54: Unfolded prompt J/ψ R_{AA} in centrality bins.

896 References

- 897 [1] T. Matsui and H. Satz, “J/ ψ suppression by quark-gluon plasma formation”, *Phys. Lett. B*
898 **178** (1986) 416, doi:10.1016/0370-2693(86)91404-8.
- 899 [2] P. Braun-Munzinger and J. Stachel, “(Non) thermal aspects of charmonium production
900 and a new look at J/ ψ suppression”, *Phys. Lett. B* **490** (2000) 196,
901 doi:10.1016/S0370-2693(00)00991-6, arXiv:nucl-th/0007059.
- 902 [3] PHENIX Collaboration, “J/ ψ production versus centrality, transverse momentum, and
903 rapidity in AuAu collisions at $\sqrt{s_{\text{NN}}} = 200 \text{ GeV}$ ”, *Phys. Rev. Lett.* **98** (2007) 232301,
904 doi:10.1103/PhysRevLett.98.232301, arXiv:nucl-ex/0611020.
- 905 [4] PHENIX Collaboration, “J/ ψ suppression at forward rapidity in AuAu collisions at $\sqrt{s_{\text{NN}}}$
906 = 200 GeV”, *Phys. Rev. C* **84** (2011) 054912, doi:10.1103/PhysRevC.84.054912,
907 arXiv:1103.6269.
- 908 [5] NA50 Collaboration, “Evidence for deconfinement of quarks and gluons from the J / psi
909 suppression pattern measured in Pb + Pb collisions at the CERN SPS”, *Phys. Lett.* **B477**
910 (2000) 28–36, doi:10.1016/S0370-2693(00)00237-9.
- 911 [6] LHCb Collaboration, “Study of J/ Production in Jets”, *Phys. Rev. Lett.* **118** (2017), no. 19,
912 192001, doi:10.1103/PhysRevLett.118.192001, arXiv:1701.05116.
- 913 [7] R. Bain et al., “NRQCD Confronts LHCb Data on Quarkonium Production within Jets”,
914 *Phys. Rev. Lett.* **119** (2017), no. 3, 032002, doi:10.1103/PhysRevLett.119.032002,
915 arXiv:1702.05525.
- 916 [8] F. Arleo, “Quenching of Hadron Spectra in Heavy Ion Collisions at the LHC”, *Phys. Rev.*
917 *Lett.* **119** (2017), no. 6, 062302, doi:10.1103/PhysRevLett.119.062302,
918 arXiv:1703.10852.
- 919 [9] CMS Collaboration, “Nuclear modification factor of charmonia in PbPb collisions at
920 $\sqrt{s_{\text{NN}}} = 5.02 \text{ TeV}$ ”, arXiv:1712.08959.
- 921 [10] CMS Collaboration, “Charged-particle nuclear modification factors in PbPb and pPb
922 collisions at $\sqrt{s_{\text{NN}}} = 5.02 \text{ TeV}$ ”, *JHEP* **04** (2017) 039,
923 doi:10.1007/JHEP04(2017)039, arXiv:1611.01664.
- 924 [11] CMS Collaboration, “Suppression and azimuthal anisotropy of prompt and nonprompt
925 J/ ψ production in PbPb collisions at $\sqrt{s_{\text{NN}}} = 2.76 \text{ TeV}$ ”, *Eur. Phys. J. C* (2016)
926 doi:10.3204/PUBDB-2016-04916, arXiv:arXiv:1610.00613.
- 927 [12] P. Berta, M. Spousta, D. W. Miller, and R. Leitner, “Particle-level pileup subtraction for
928 jets and jet shapes”, *JHEP* **06** (2014) 092, doi:10.1007/JHEP06(2014)092,
929 arXiv:1403.3108.
- 930 [13] T. Sjöstrand et al., “An Introduction to PYTHIA 8.2”, *Comput. Phys. Commun.* **191** (2015)
931 159–177, doi:10.1016/j.cpc.2015.01.024, arXiv:arXiv:1410.3012.
- 932 [14] Yeonju Go, Kisoo Lee, Javier Martin Blanco, Stephen Sanders, Shengquan Tuo, Qiao Xu,
933 Anna Zsigmond, “Centrality and event plane reconstruction for pbpb collisions at 5 tev
934 in 2015”, CMS Note 2015/080, 2015.

- 935 [15] The Heavy-Ion Dilepton PinG, "Muon performance studies in 2018 pbpb tev data", CMS
936 Note 2018/316, 2018.
- 937 [16] The Heavy-Ion Dilepton PinG, "Dimuon performance studies in 2015 5.02 TeV pp and
938 pbpb data", CMS Note 2016/048, 2016.
- 939 [17] C. Lourenço et al., "Prompt J/ ψ and $\psi(2S)$ differential cross sections in pp collisions at
940 $\sqrt{s} = 7$ TeV", CMS Note AN-2014/003, 2014.
- 941 [18] M. Jo, D. Moon, T. Dahms, and C. Mironov, " R_{AA} and v_2 of prompt and non-prompt J/ ψ
942 in 2011 pbpb and 2013 pp collisions", CMS Note AN-2014/061, 2014.
- 943 [19] W. Verkerke and D. P. Kirkby, "The RooFit toolkit for data modeling", *eConf* **C0303241**
944 (2003) MOLT007, arXiv:physics/0306116. [,186(2003)].
- 945 [20] O. Kukral et al., "Charmonia in 5.02 TeV data", CMS Analysis Note 2016/067, 2016.
- 946 [21] M. Pivk and F. Le Diberder, " $sPlot$: a statistical tool to unfold data distributions",
947 arxiv:physics/0402083 (2005).
- 948 [22] ROOT Collaboration, "HistFactory: A tool for creating statistical models for use with
949 RooFit and RooStats", Technical Report CERN-OPEN-2012-016, Jan, 2012.
- 950 [23] CMS Collaboration, "Jet energy scale and resolution in the CMS experiment in pp
951 collisions at 8 TeV", *JINST* **12** (2017), no. 02, P02014,
952 doi:10.1088/1748-0221/12/02/P02014, arXiv:1607.03663.
- 953 [24] CMS Collaboration, "Comparing transverse momentum balance of b jet pairs in pp and
954 PbPb collisions at $\sqrt{s_{NN}} = 5.02$ TeV", *JHEP* **03** (2018) 181,
955 doi:10.1007/JHEP03(2018)181, arXiv:1802.00707.
- 956 [25] K. S. Cranmer, "Kernel estimation in high-energy physics", *Comput. Phys. Commun.* **136**
957 (2001) 198–207, doi:10.1016/S0010-4655(00)00243-5,
958 arXiv:hep-ex/0011057.
- 959 [26] CMS Collaboration Collaboration, "Production of prompt and nonprompt J/ ψ mesons in
960 jets in pp collisions at $\sqrt{s} = 5.02$ TeV", Technical Report CMS-PAS-HIN-18-012, CERN,
961 Geneva, 2018.
- 962 [27] D. H. Y. Chen, S. Obraszczov, "Jet performance in 2018 PbPb heavy ion run", CMS
963 Analysis Note 2019/017, 2019.
- 964 [28] CMS Collaboration, "Relative Modification of Prompt $\psi(2S)$ and J/ ψ Yields from pp to
965 PbPb Collisions at $\sqrt{s_{NN}} = 5.02$ TeV", *Phys. Rev. Lett.* **118** (2017), no. 16, 162301,
966 doi:10.1103/PhysRevLett.118.162301.

967 A Determination of the invariant mass parameters from MC

968 In this section we present the study performed to choose the best signal shape to fit the data,
 969 extract the parameters that are fixed in the data fitting procedure and test the different assump-
 970 tions that we make in data fits in terms of the relation between the signal parameters of prompt
 971 and nonprompt J/ ψ . The study is based on fitting the MC invariant mass distributions after
 972 background subtraction using the same binning as in data.

973 The resulting background-free MC invariant mass distributions in z bins are fitted with an
 974 unbinned likelihood fit procedure using three different signal shapes: a single Crystal Ball (CB),
 975 a Double Crystal Ball and a Crystal Ball plus a Gaussian function. In the last two cases, the
 976 J/ ψ mass, and the tail parameters (for the double CB) are shared among the two components.
 977 In order to avoid the influence of some possible remaining background events, which affect
 978 specially the right tail of the MC signal, we restrict the fitting range with respect to the one
 979 used in data. The ranges are chosen according to the signal resolution in each rapidity region,
 980 and they are shown as a dashed line in the invariant mass plots ($2.2 < m_{\mu^+\mu^-} < 3.26$ for rapidity
 981 ranges in the region $|y| < 1.2$ and $2.2 < m_{\mu^+\mu^-} < 3.32$ for rapidity ranges in or including the
 982 region $|y| > 1.2$). All the parameters are left free on the fits.

983 A.1 Background subtraction from MC samples

984 In order to obtain a pure J/ ψ sample, the background is removed from the MC sample by re-
 985 quiring a matching of the reconstructed dimuons with a generated J/ ψ . This matching requires
 986 both muons in a dimuon to pass the cut $\Delta R_{reco-gen}^\pm = \sqrt{(\Delta\eta_{reco-gen}^\pm)^2 + (\Delta\phi_{reco-gen}^\pm)^2} < 0.03$,
 987 where $\Delta\eta_{reco-gen}$ and $\Delta\phi_{reco-gen}$ are the differences between the generated and reconstructed
 988 values of the pseudorapidity and azimuthal angle respectively. The value of this cut has been
 989 taken according to the result in Fig. 55, in order to reject most of the background events keeping
 990 a big fraction of the signal. In Fig. 55 we show the MC invariant mass distribution as a function
 991 of ΔR , which in this case is defined as $\Delta R = \max(\Delta R_{reco-gen}^+, \Delta R_{reco-gen}^-)$.

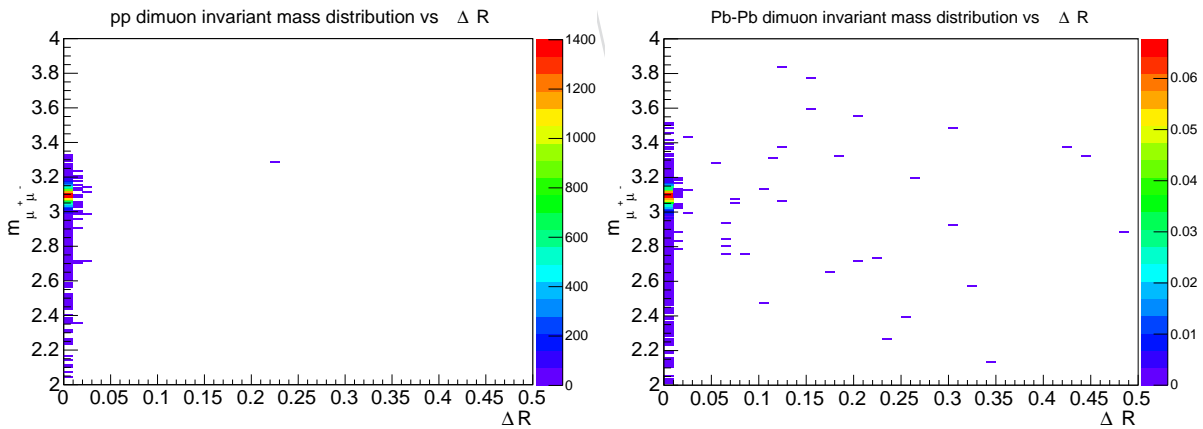


Figure 55: Invariant-mass distribution of $\mu^+\mu^-$ pairs in pp (left) and PbPb (right) MC as a function of $\Delta R = \max(\Delta R_{reco-gen}^+, \Delta R_{reco-gen}^-)$.

992 A.2 Tail parameters study of the two components of the double Crystal Ball

993 In this section we study the evolution of the different parameters of the double Crystal Ball and
 994 Crystal Ball plus Gauss obtained in MC as a function of z . It was shown in HIN-16-004 [28] that
 995 the tail parameters should be the same for the two components of the double CB.

996 In Figs. 56 and 57 we see the evolution of α , and the ratio of sigmas obtained in J/ψ MC fits as
 997 a function of z for the two signal shapes in the rapidity region $|y| < 2.4$. The averages for α
 998 are shown as dashed horizontal lines. Markers in red are not taken into account when average
 999 is computed due to the lack of statistics or because of a bad fit. From these results we observe
 1000 that there is almost no variation of α or the ratio of sigmas as a function of z .

1001 Since α is shown to be independant of z , its value is fixed to the z -integrated fit to extract the
 1002 values of n used to fit data. In addition for Pb-Pb, as the ratio of sigmas is also fixed. n shows
 1003 a dependence on z so the values in data are fixed to the corresponding bin in MC. The results
 1004 are shown in Fig.58.

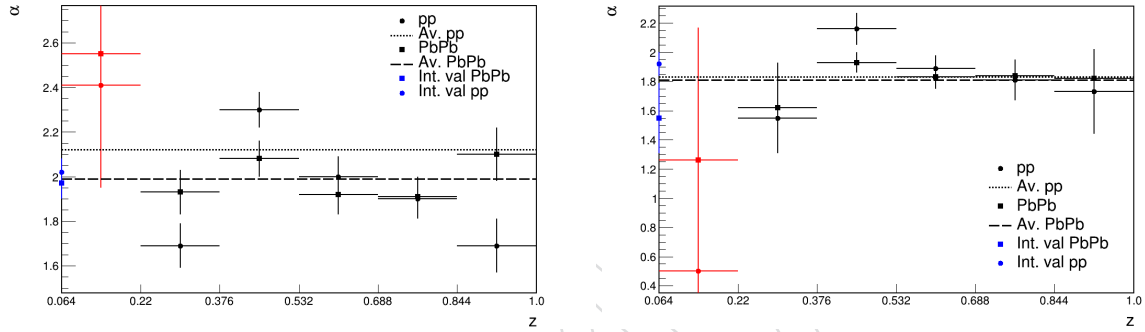


Figure 56: Evolution of α as a function of z in the rapidity range $|y| < 2.4$ for the double Crystal Ball (left) and Crystal Ball plus Gauss (right) shapes, obtained from J/ψ fits in MC with $30 < p_T^{jet} < 40$ GeV. In addition the values obtained in the z -average (dashed lines) over the different bins and z -integrated (blue point) are reported.

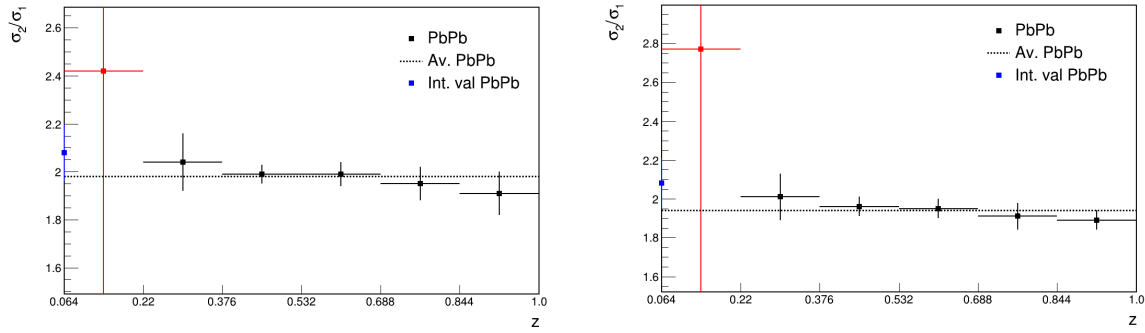


Figure 57: The ratio of sigmas evolution as a function of z in the rapidity range $|y| < 2.4$ for the double Crystal Ball (left) and Crystal Ball plus Gauss (right) shapes, obtained from J/ψ fits in MC with $30 < p_T^{jet} < 40$ GeV. In addition the values obtained in the z -average (dashed lines) over the different bins and z -integrated (blue point) are reported.

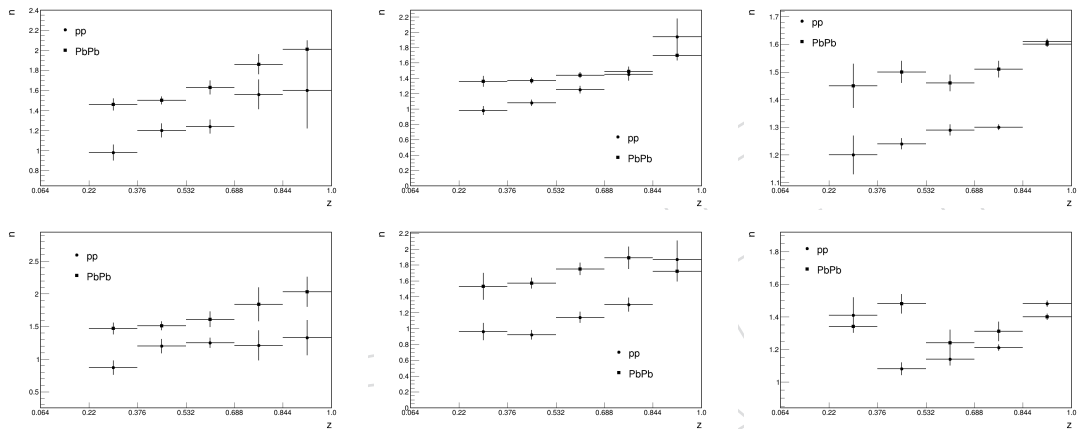


Figure 58: Evolution of n as a function of z for three different jet p_T bins. Results shown for the double Crystal Ball (upper row) and Crystal Ball plus Gauss (lower row) shapes, obtained from J/ψ fits in MC. In each row, from left to right, the jet- p_T ranges are: 40-60, 30-40 and 10-30 GeV.

1005 **A.3 Choice of the Chebychev polynomial order for the background model: LLR**
 1006 **tests**

1007 For each analysis bin, Chebychev polynomials of orders 0 (uniform distribution) to 6 were
 1008 tried, using the double Crystal Ball function with the signal tail parameters and ratio of sigmas
 1009 fixed to the MC values. We chose the order in such a way that increasing the order does not
 1010 significantly improve the quality of the fit. The p-value is required to be smaller than 5%. The
 1011 order of the Chebychev polynomial used to fit the background in data, resulting from the log
 1012 likelihood ratio test performed in each of the analysis bins can be seen in Figs. 68-63, .

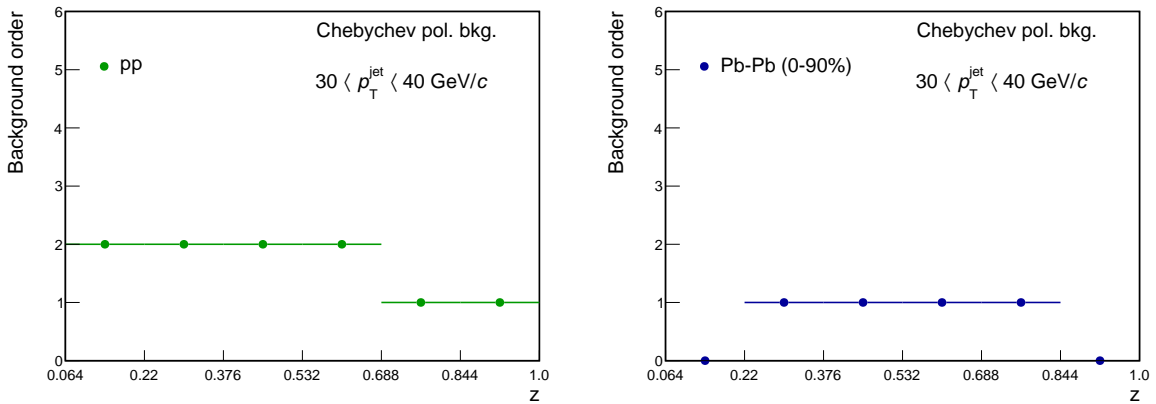


Figure 59: Results of the order chosen for the nominal ($p\text{-value} < 5\%$) fits using the log likelihood ratio test performed in each of the analysis bins as a function of z in pp (left) and PbPb in 0-90% centrality (right) for J/ψ in jets with $30 < p_T < 40 \text{ GeV}$.

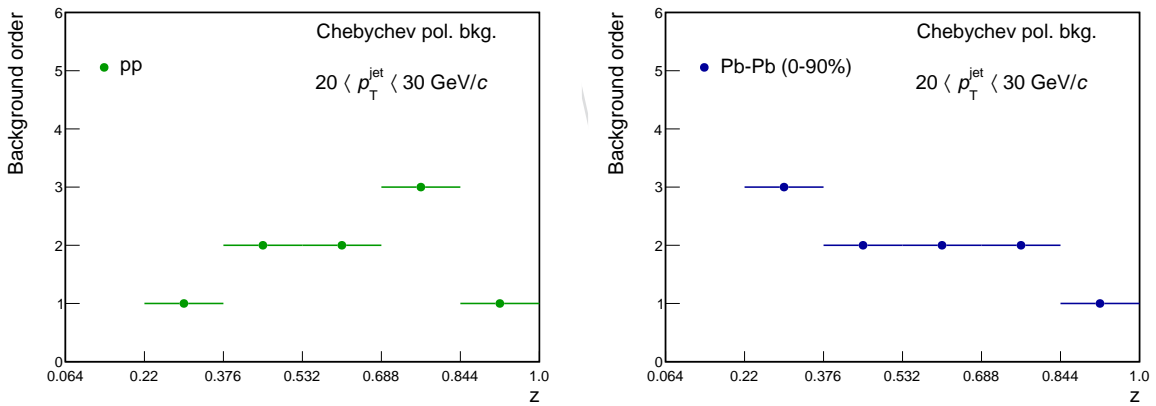


Figure 60: Results of the order chosen for the nominal ($p\text{-value} < 5\%$) fits using the log likelihood ratio test performed in each of the analysis bins as a function of z in pp (left) and PbPb in 0-90% centrality (right) for J/ψ in jets with $20 < p_T < 30 \text{ GeV}$.

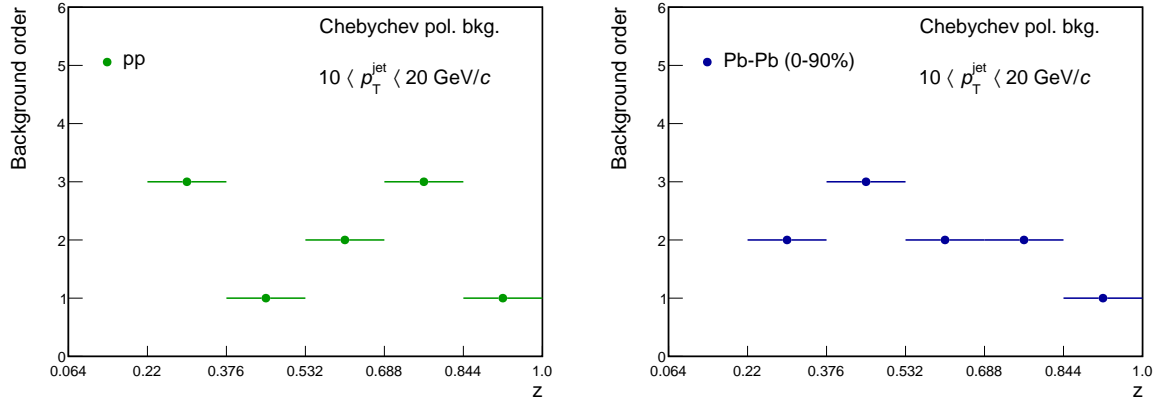


Figure 61: Results of the order chosen for the nominal ($p\text{-value} < 5\%$) fits using the log likelihood ratio test performed in each of the analysis bins as a function of z in pp (left) and $PbPb$ in 0-90% centrality (right) for J/ψ in jets with $10 < p_T < 20 \text{ GeV}$.

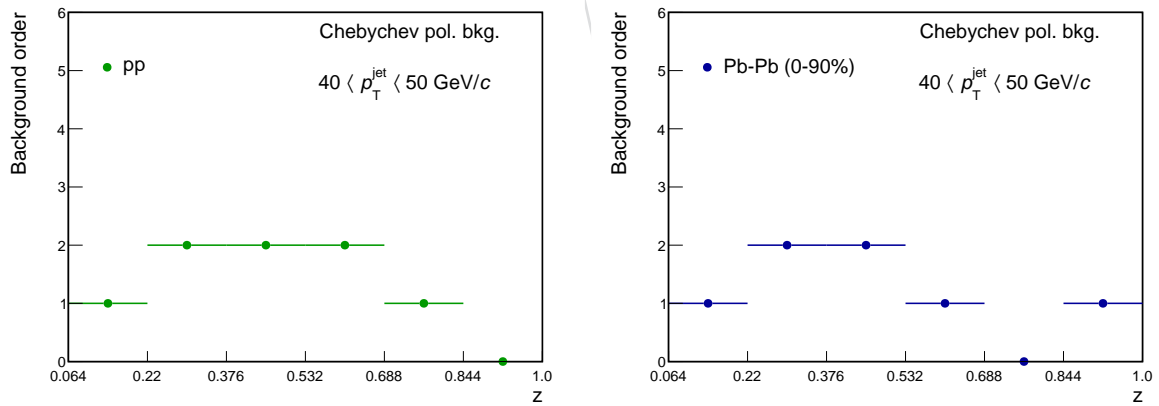


Figure 62: Results of the order chosen for the nominal ($p\text{-value} < 5\%$) fits using the log likelihood ratio test performed in each of the analysis bins as a function of z in pp (left) and $PbPb$ in 0-90% centrality (right) for J/ψ in jets with $40 < p_T < 50 \text{ GeV}$.

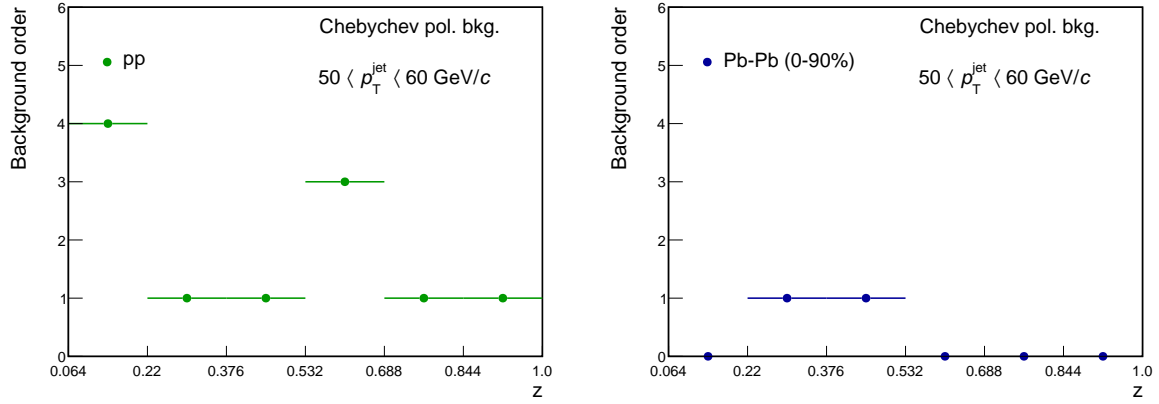


Figure 63: Results of the order chosen for the nominal ($p\text{-value} < 5\%$) fits using the log likelihood ratio test performed in each of the analysis bins as a function of z in pp (left) and Pb-Pb in 0-90% centrality (right) for J/ψ in jets with $50 < p_T < 60 \text{ GeV}$.

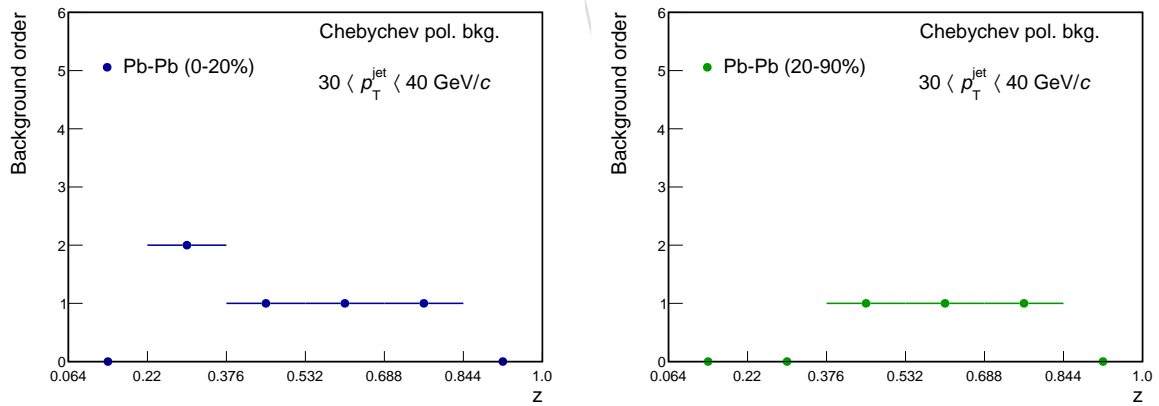


Figure 64: Results of the order chosen for the nominal ($p\text{-value} < 5\%$) fits using the log likelihood ratio test performed in each of the analysis bins as a function of z in 0-20% (left) and 20-90% centrality (right) for J/ψ in jets with $30 < p_T < 40 \text{ GeV}$.

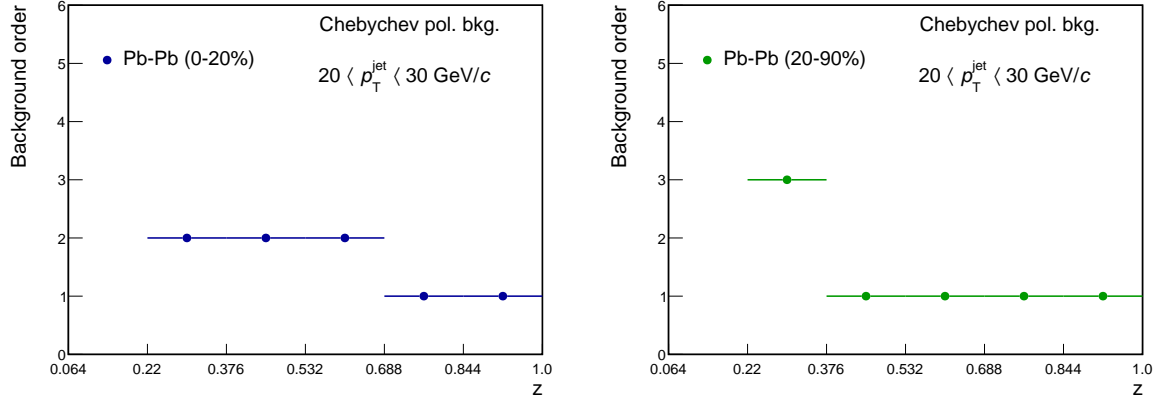


Figure 65: Results of the order chosen for the nominal (p -value $< 5\%$) fits using the log likelihood ratio test performed in each of the analysis bins as a function of z in 0-20% (left) and 20-90% centrality (right) for J/ψ in jets with $20 < p_T < 30 \text{ GeV}$.

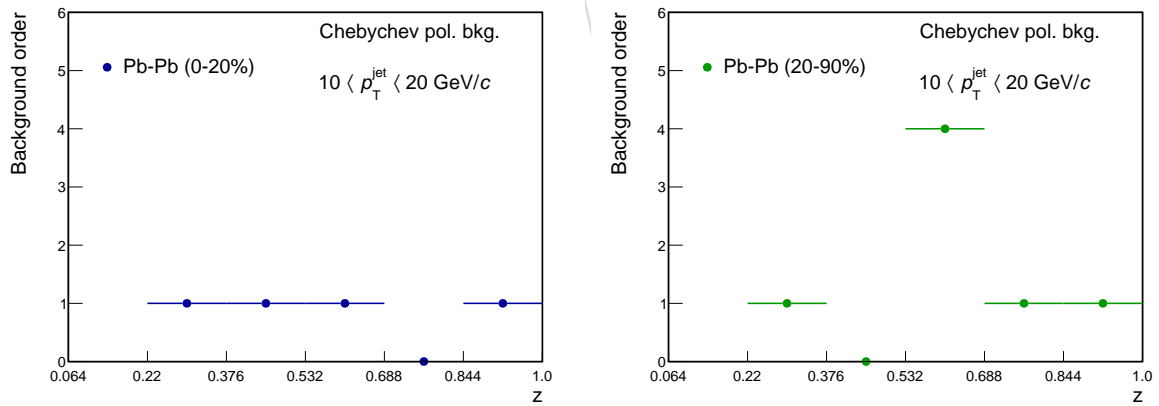


Figure 66: Results of the order chosen for the nominal (p -value $< 5\%$) fits using the log likelihood ratio test performed in each of the analysis bins as a function of z in 0-20% (left) and 20-90% centrality (right) for J/ψ in jets with $10 < p_T < 20 \text{ GeV}$.

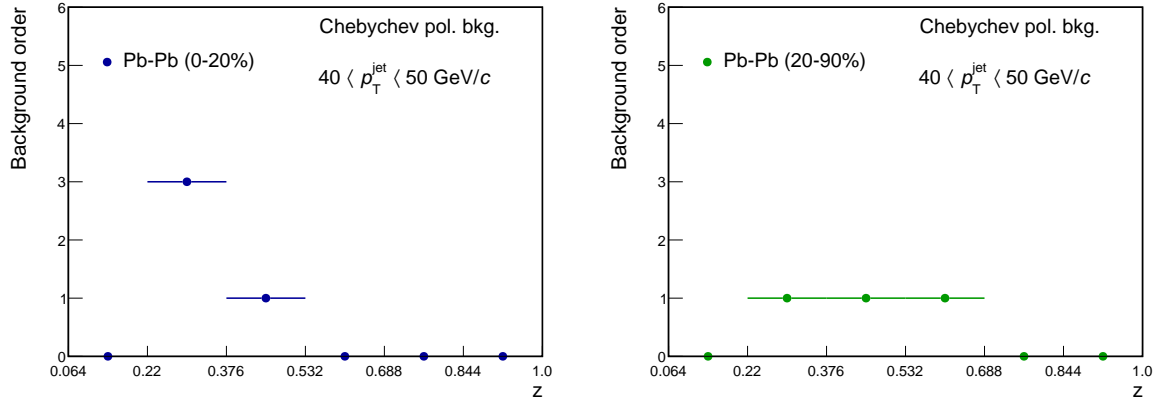


Figure 67: Results of the order chosen for the nominal (p -value $< 5\%$) fits using the log likelihood ratio test performed in each of the analysis bins as a function of z in 0-20% (left) and 20-90% centrality (right) for J/ψ in jets with $40 < p_T < 50 \text{ GeV}$.

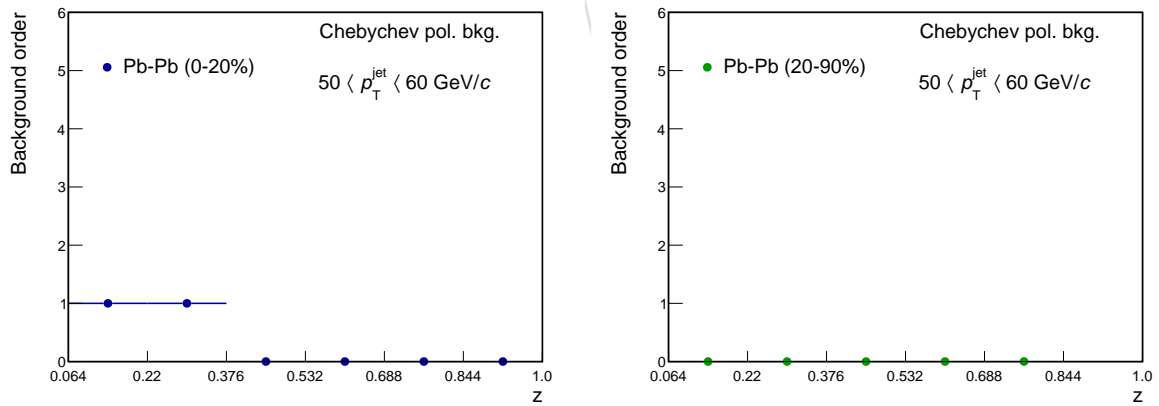


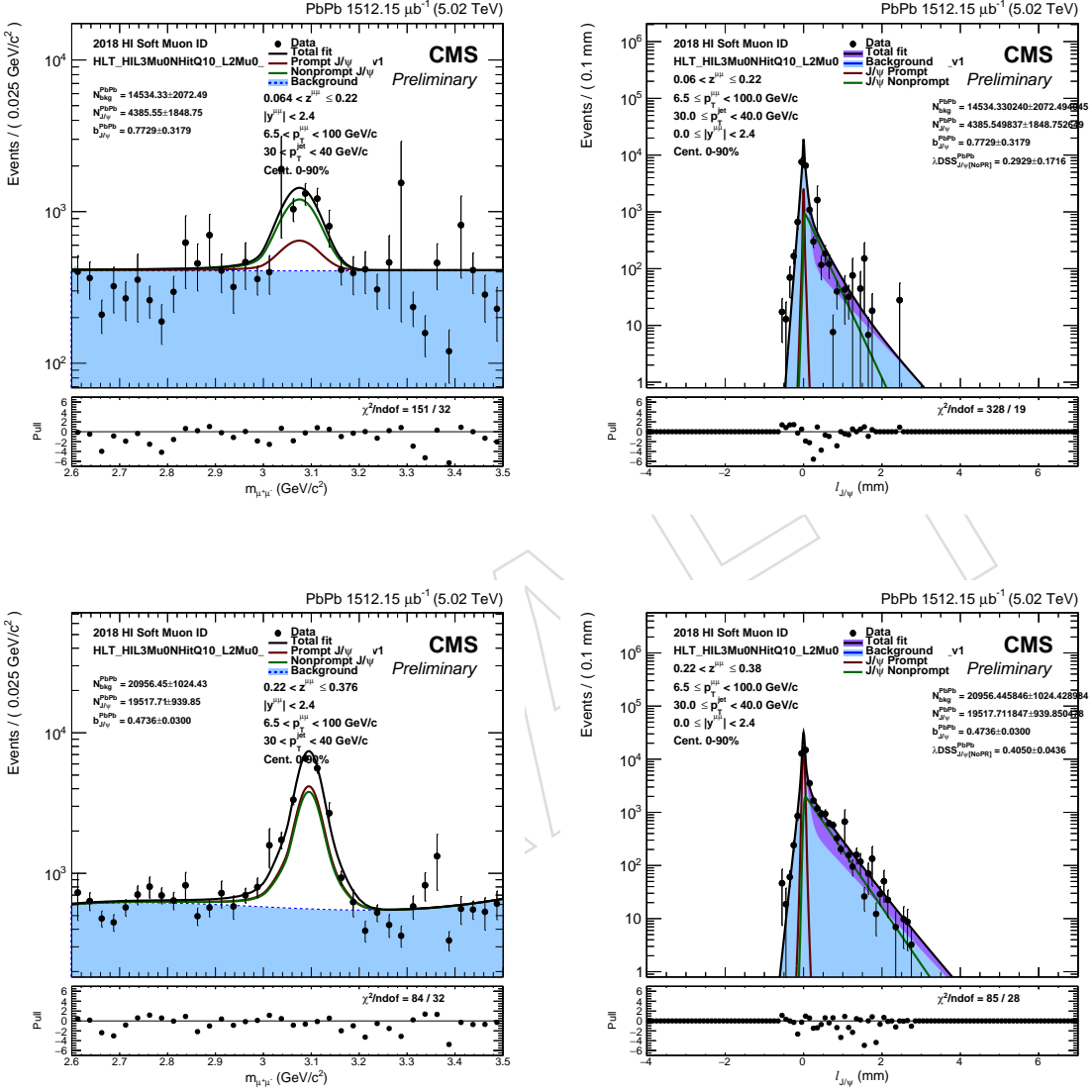
Figure 68: Results of the order chosen for the nominal (p -value $< 5\%$) fits using the log likelihood ratio test performed in each of the analysis bins as a function of z in 0-20% (left) and 20-90% centrality (right) for J/ψ in jets with $50 < p_T < 60 \text{ GeV}$.

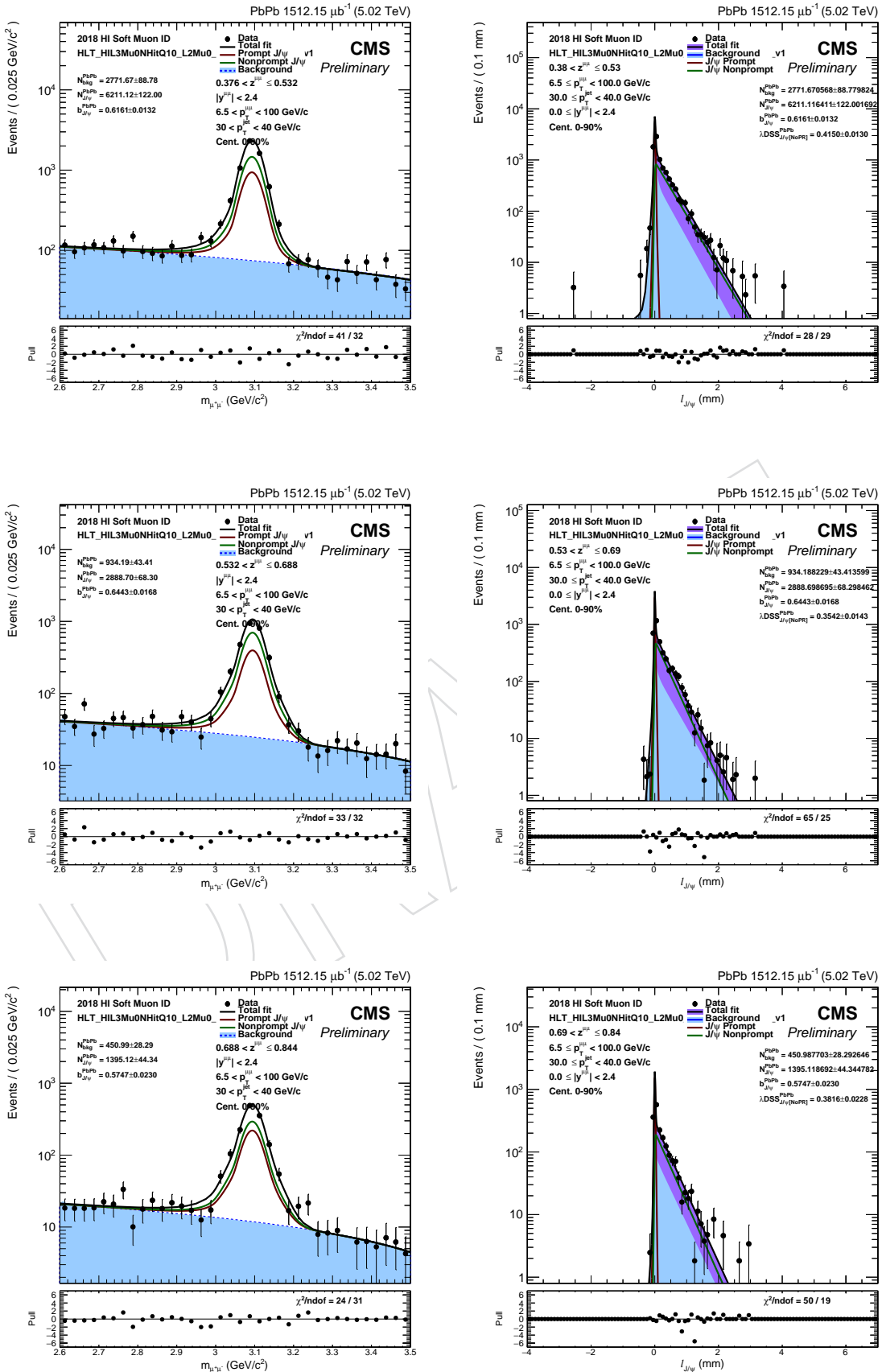
B The 2D fit projections in all analysis bins

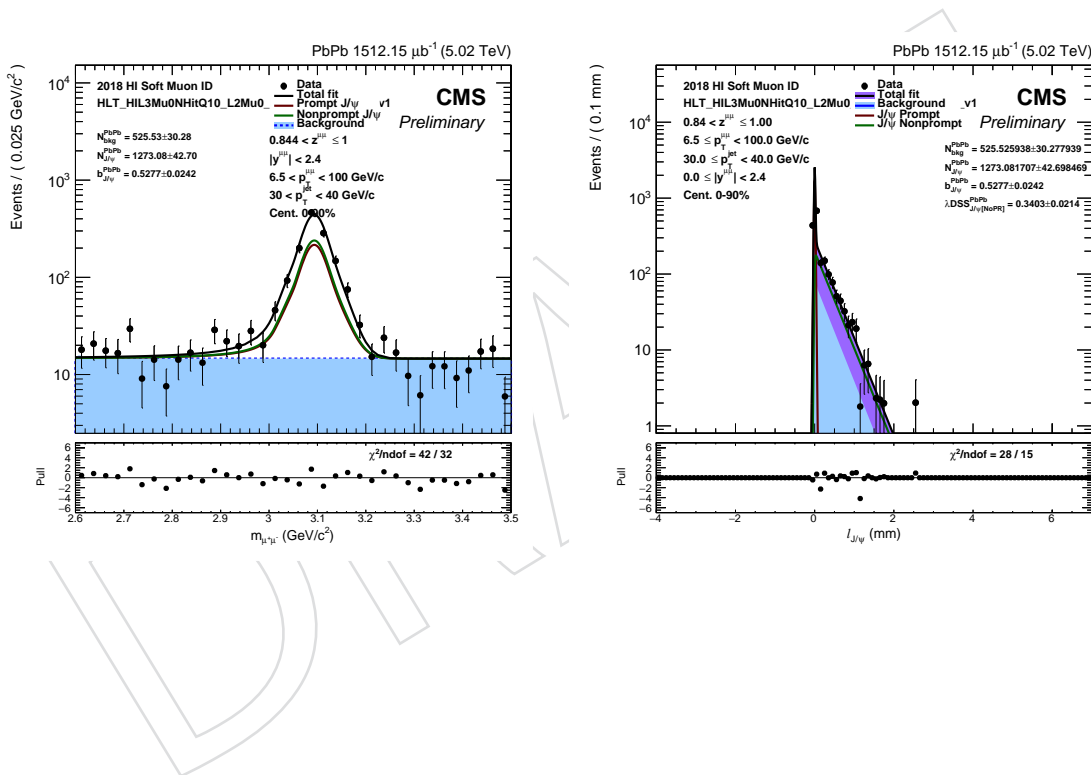
Fits for jets with $30 < p_T < 40 \text{ GeV}$

B.0.1 PbPb

The projections of the 2D fits in all z bins in PbPb collisions for $30 < p_T(\text{jet}) < 40 \text{ GeV}$, for the 0-90% centrality selection.

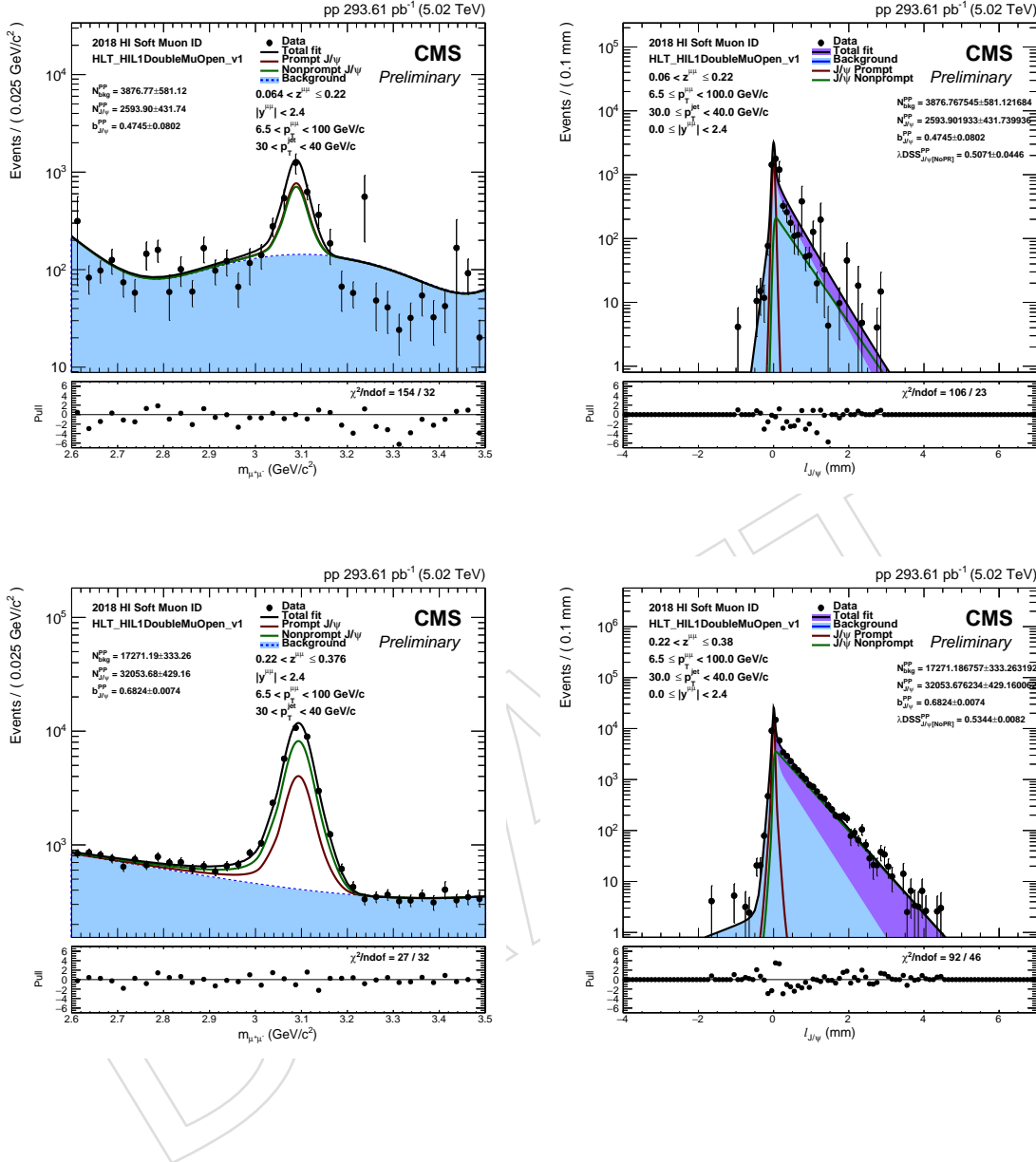


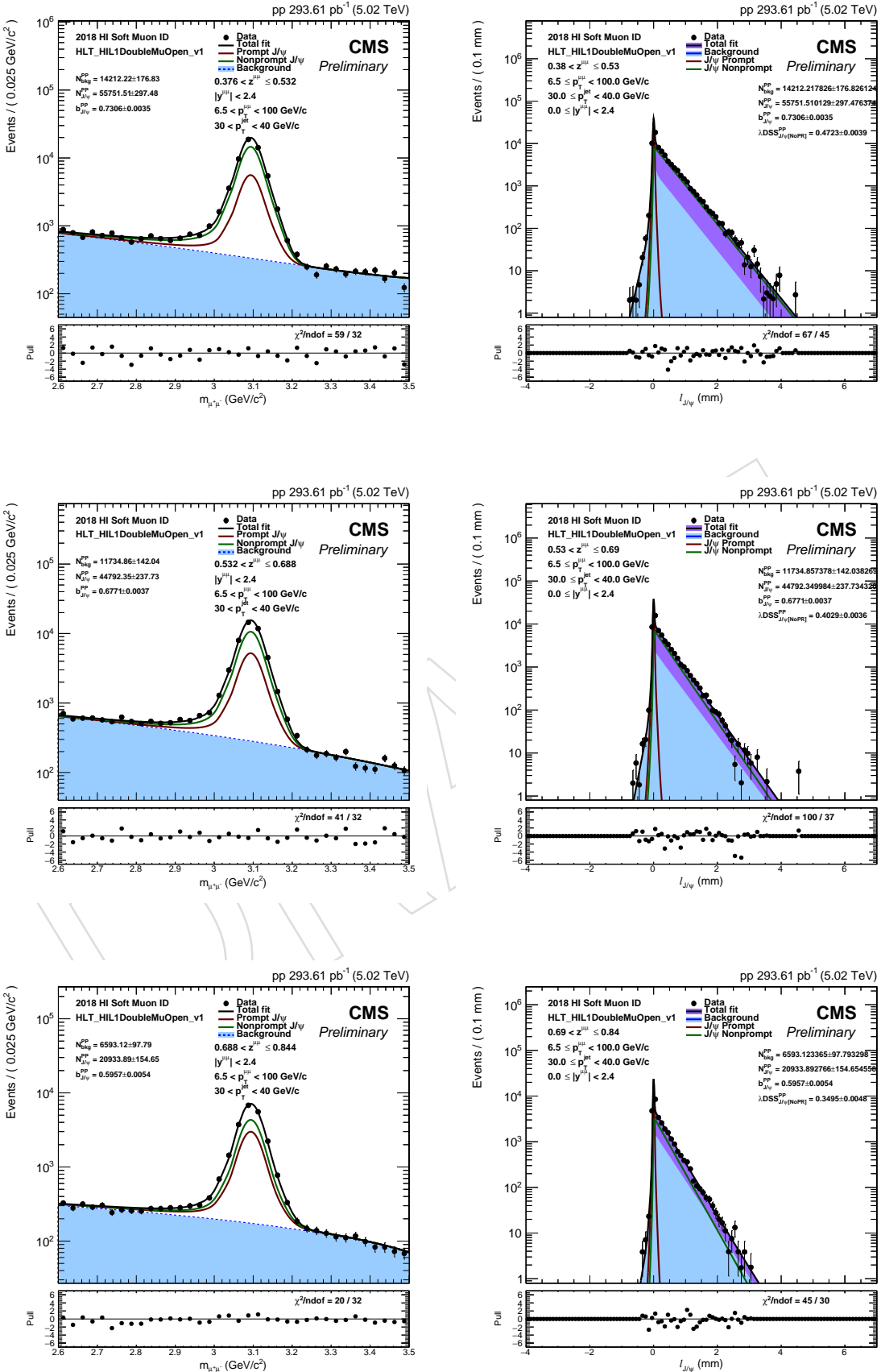


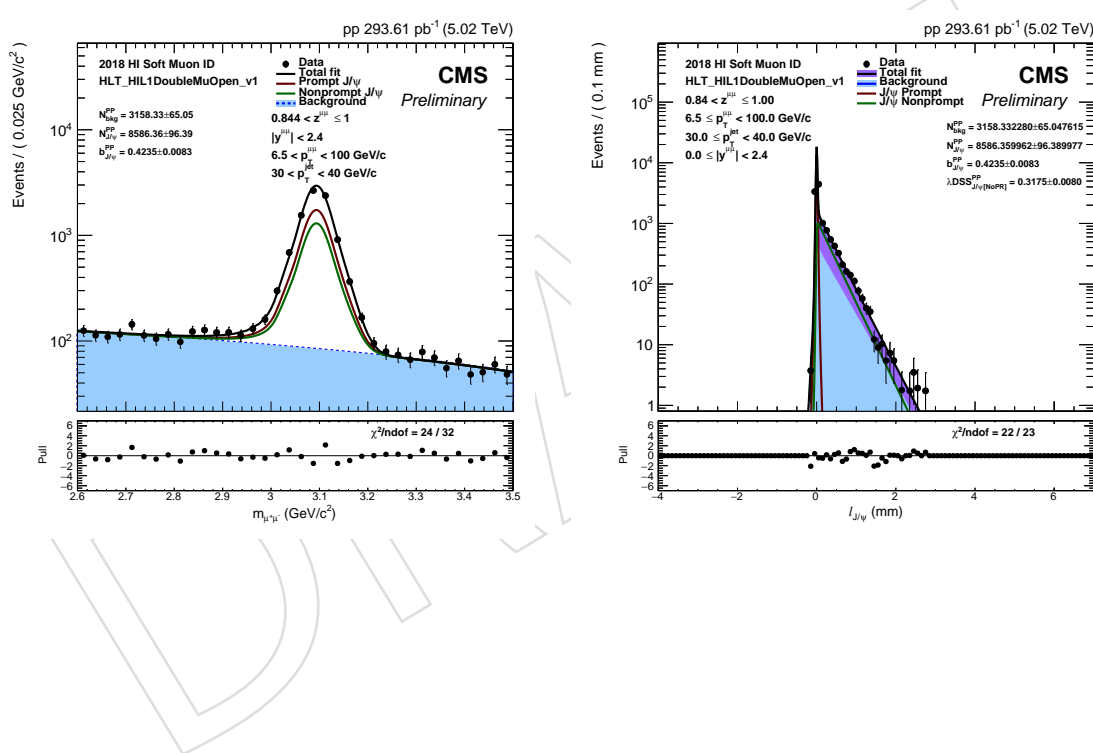


1018 **B.0.2 pp**

1019 The projections of the 2D fits in all z bins in pp collisions for $30 < p_T(\text{jet}) < 40 \text{ GeV}$.



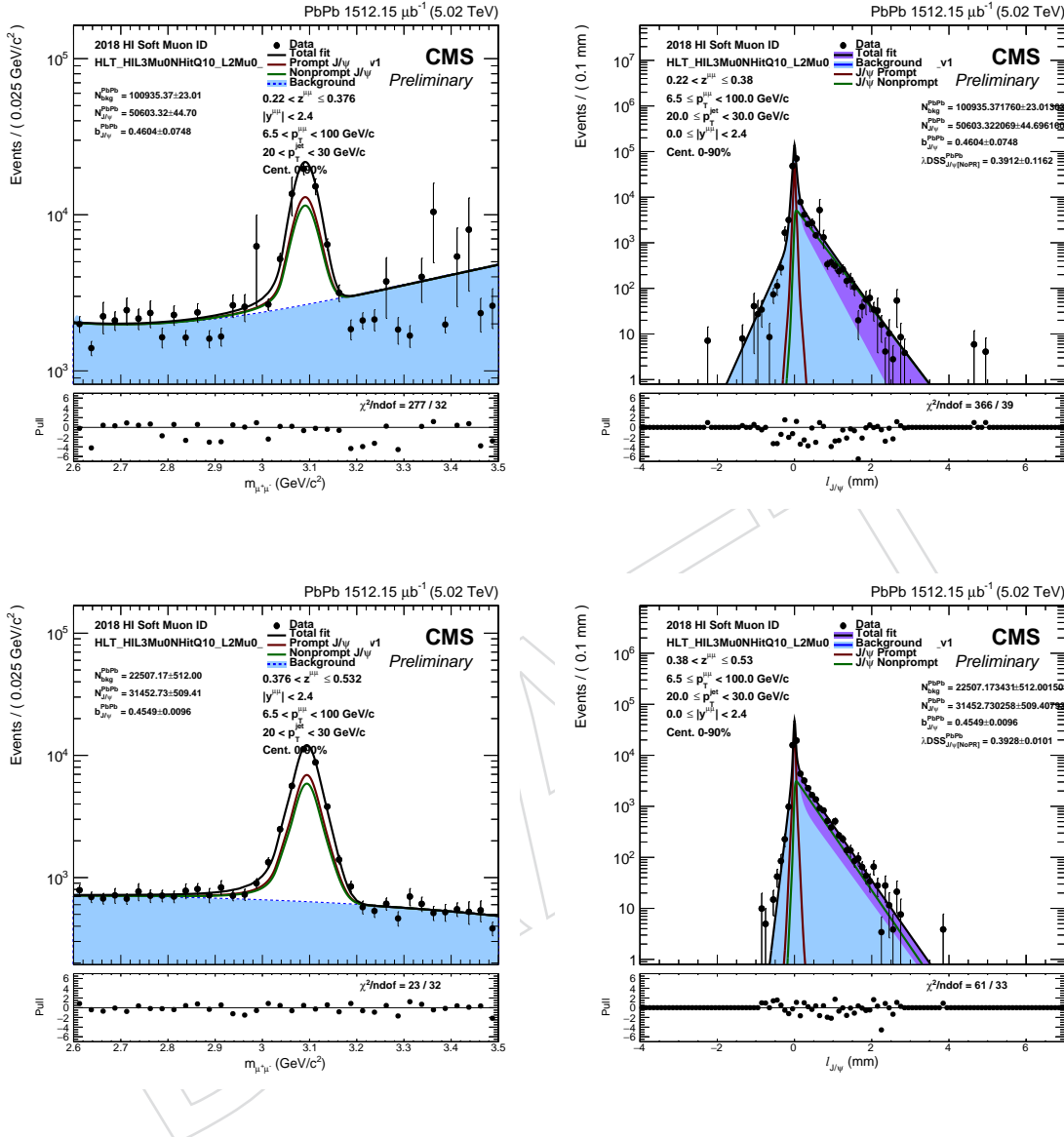


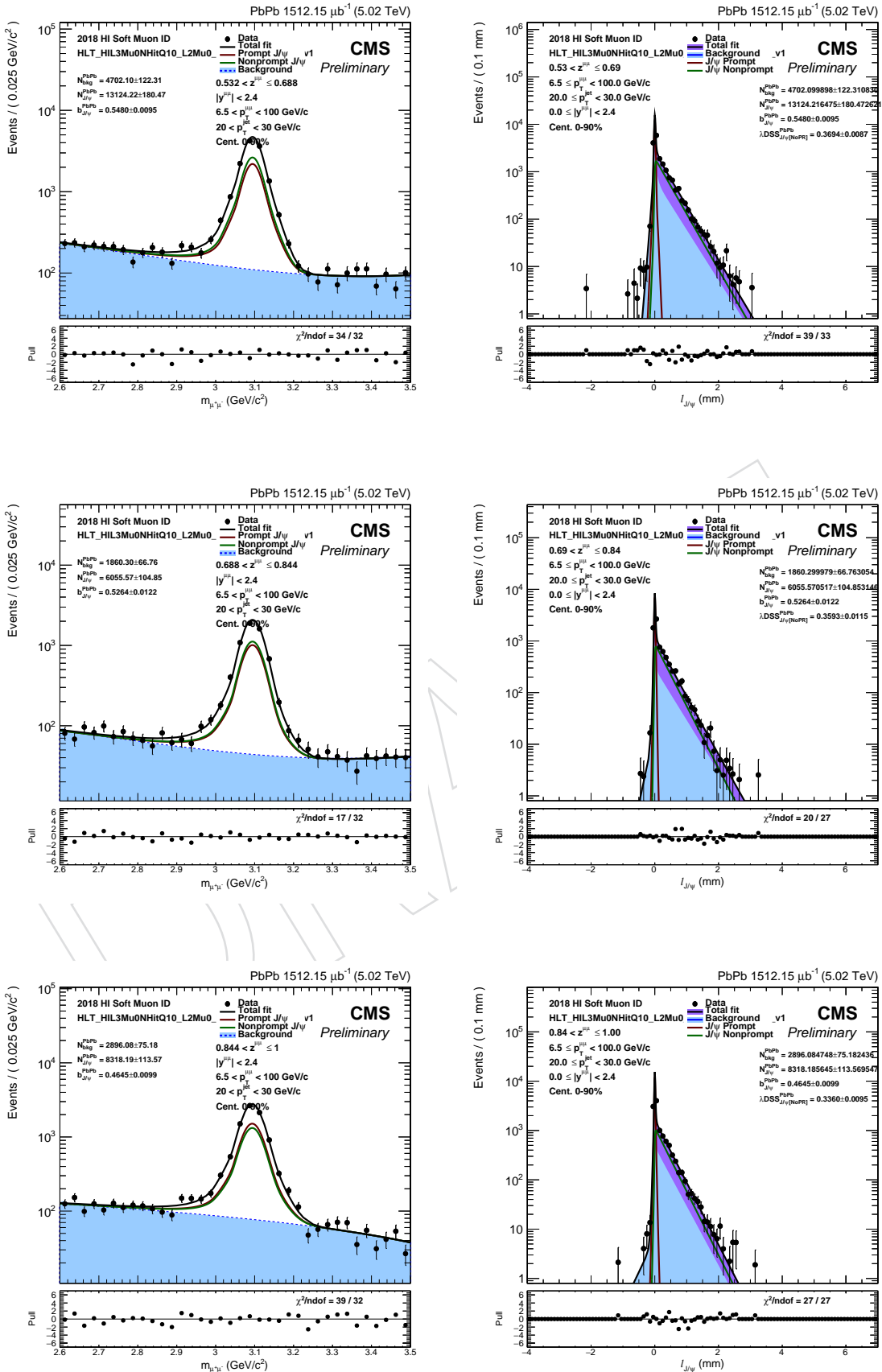


Fits for jets with $20 < p_T < 30 \text{ GeV}$

B.0.3 PbPb

The projections of the 2D fits in all z bins in PbPb collisions for $20 < p_T(\text{jet}) < 30 \text{ GeV}$.



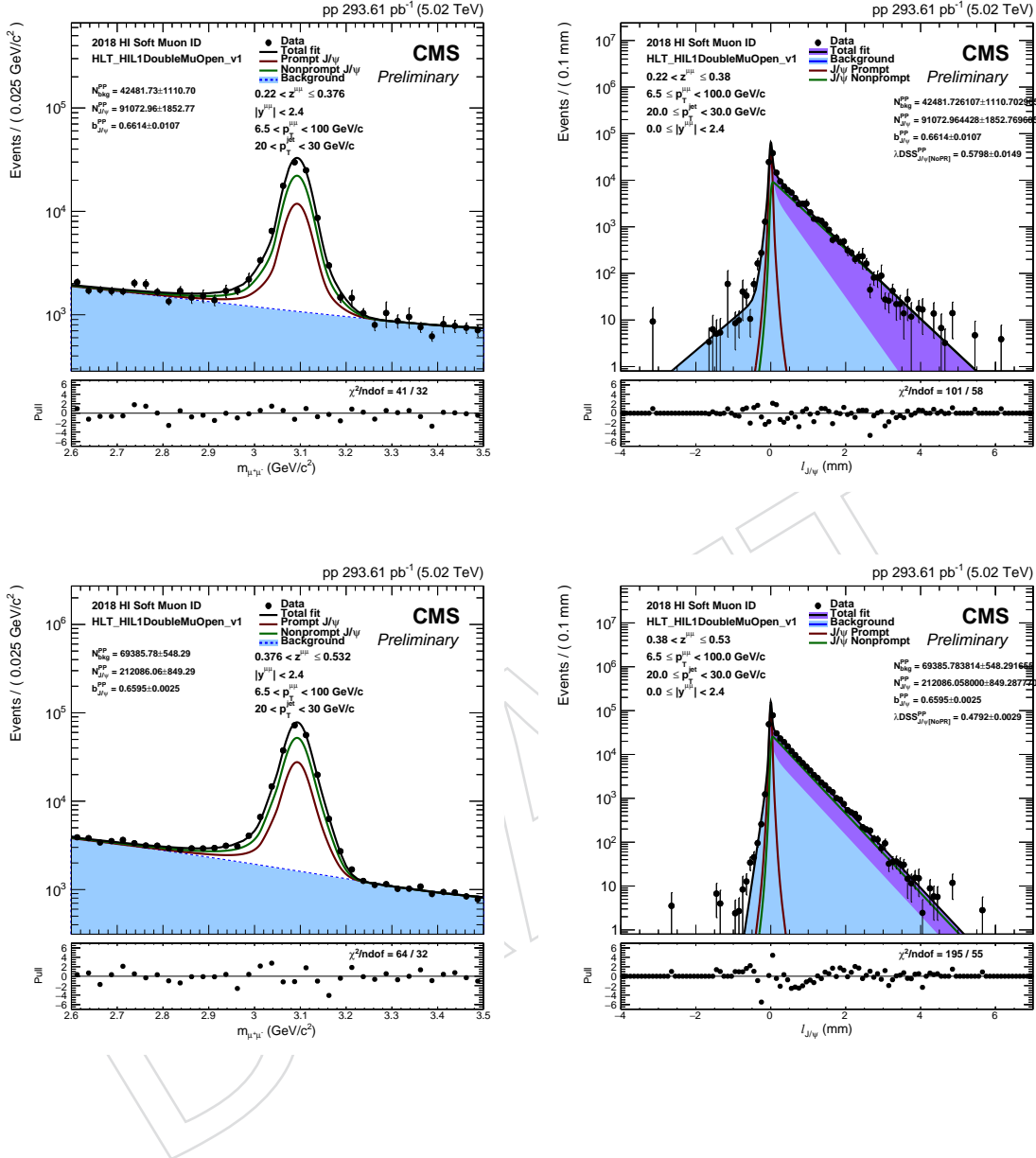


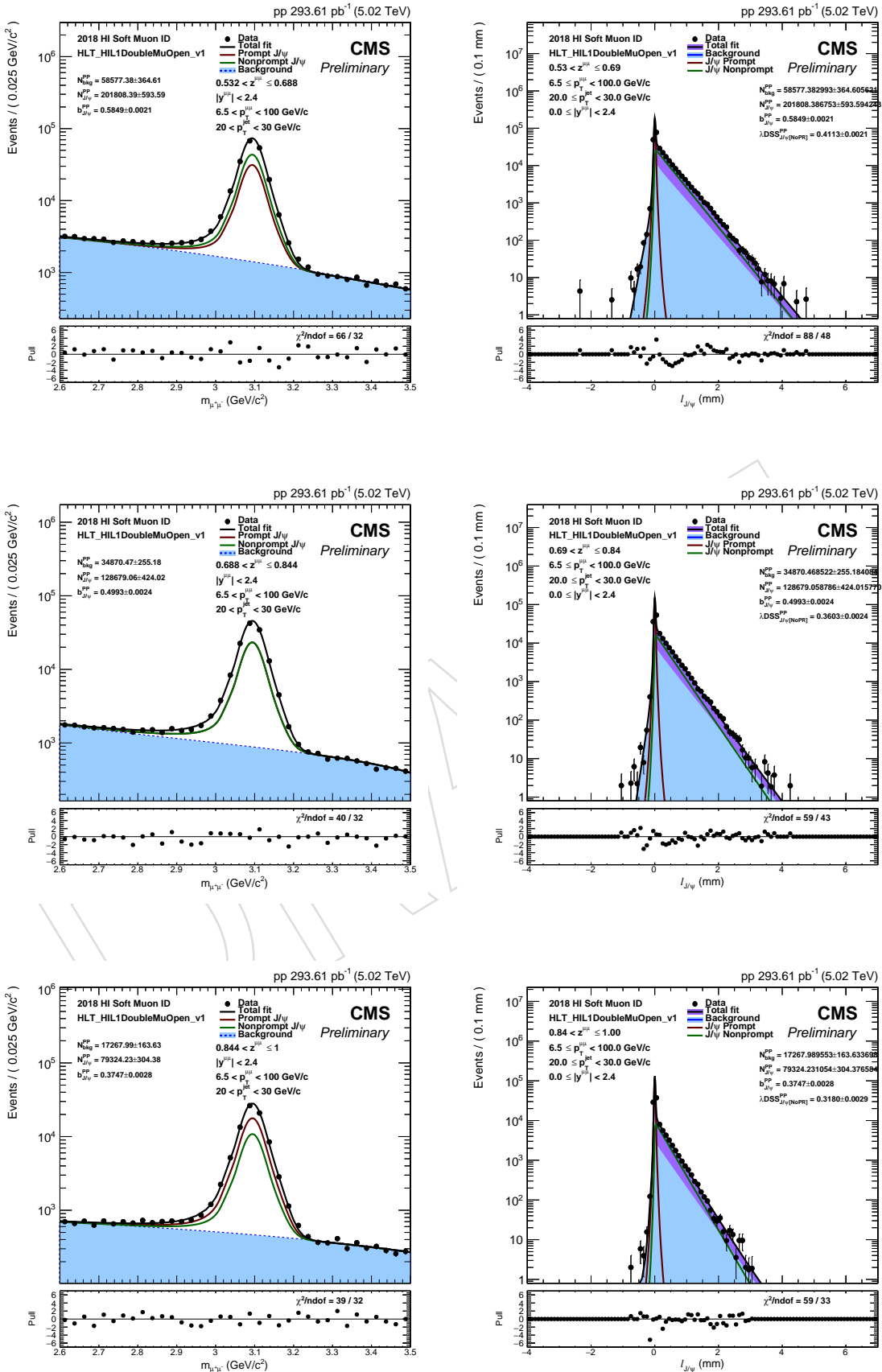
B. The 2D fit projections in all analysis bins

87

1023 B.0.4 pp

1024 The projections of the 2D fits in all z bins in pp collisions for $20 < p_T(\text{jet}) < 30 \text{ GeV}$.

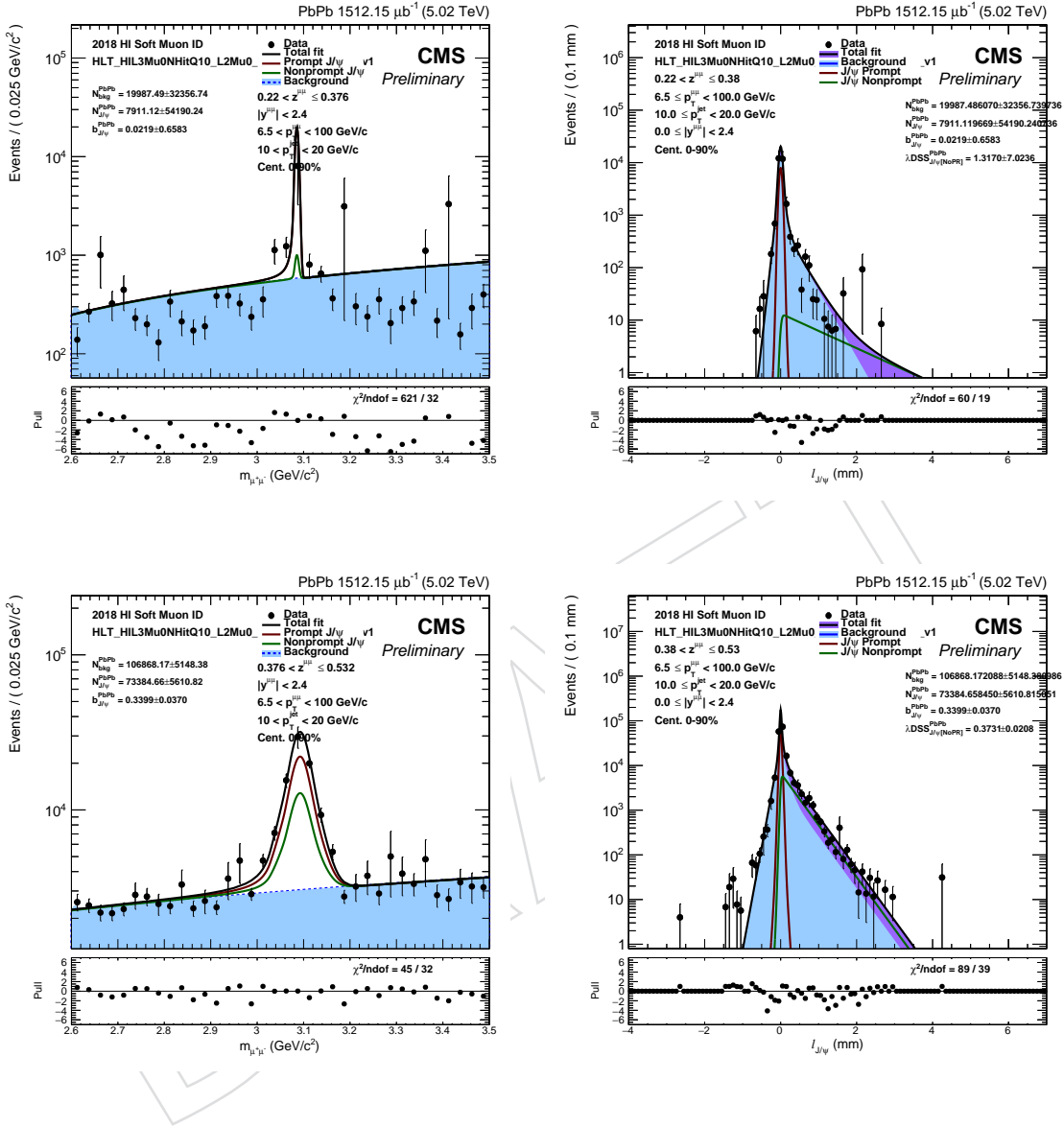


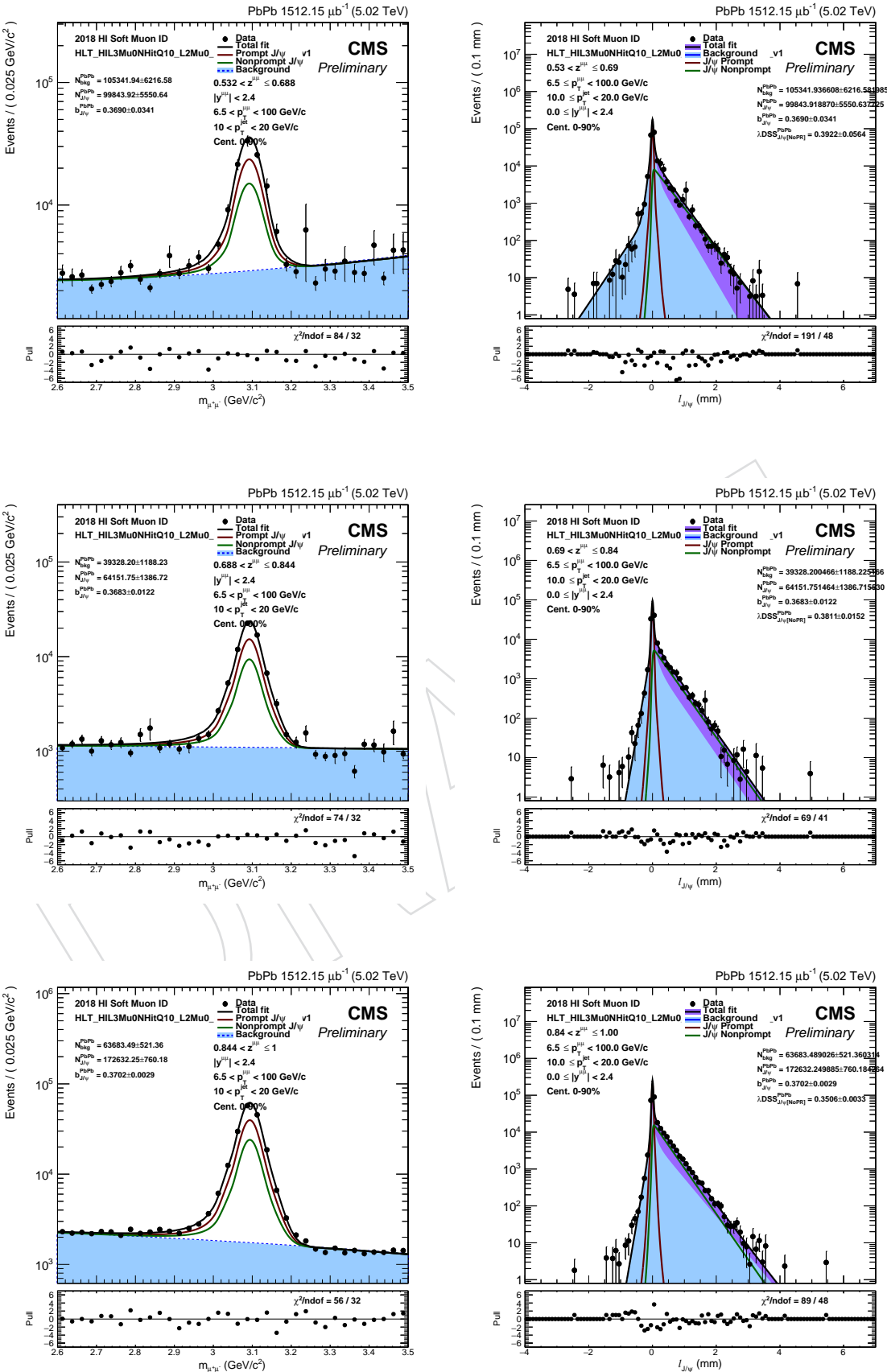


1025 **Fits for jets with $10 < p_T < 20 \text{ GeV}$**

1026 **B.0.5 PbPb**

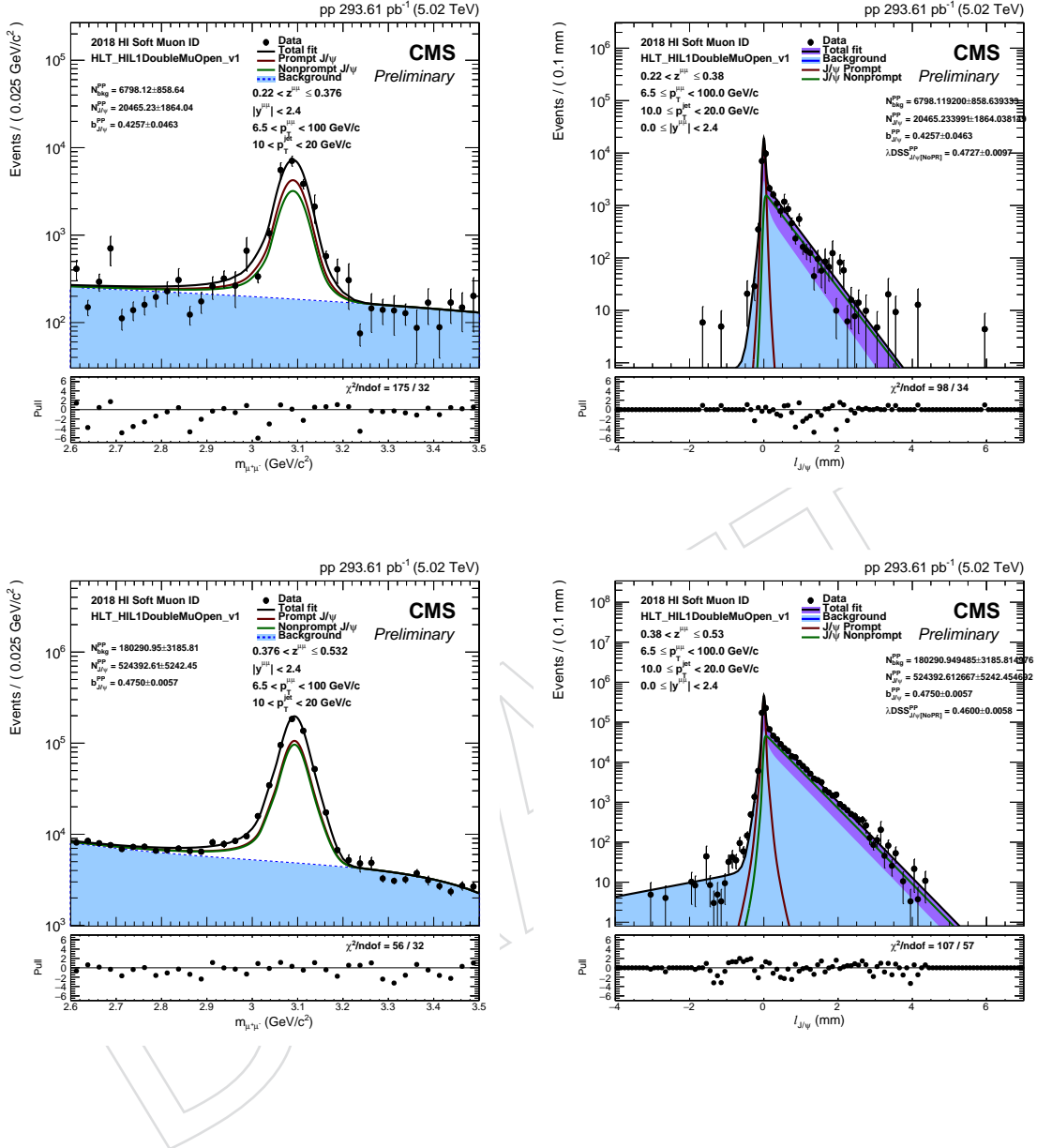
1027 The projections of the 2D fits in all z bins in PbPb collisions for $10 < p_T(\text{jet}) < 20 \text{ GeV}$.

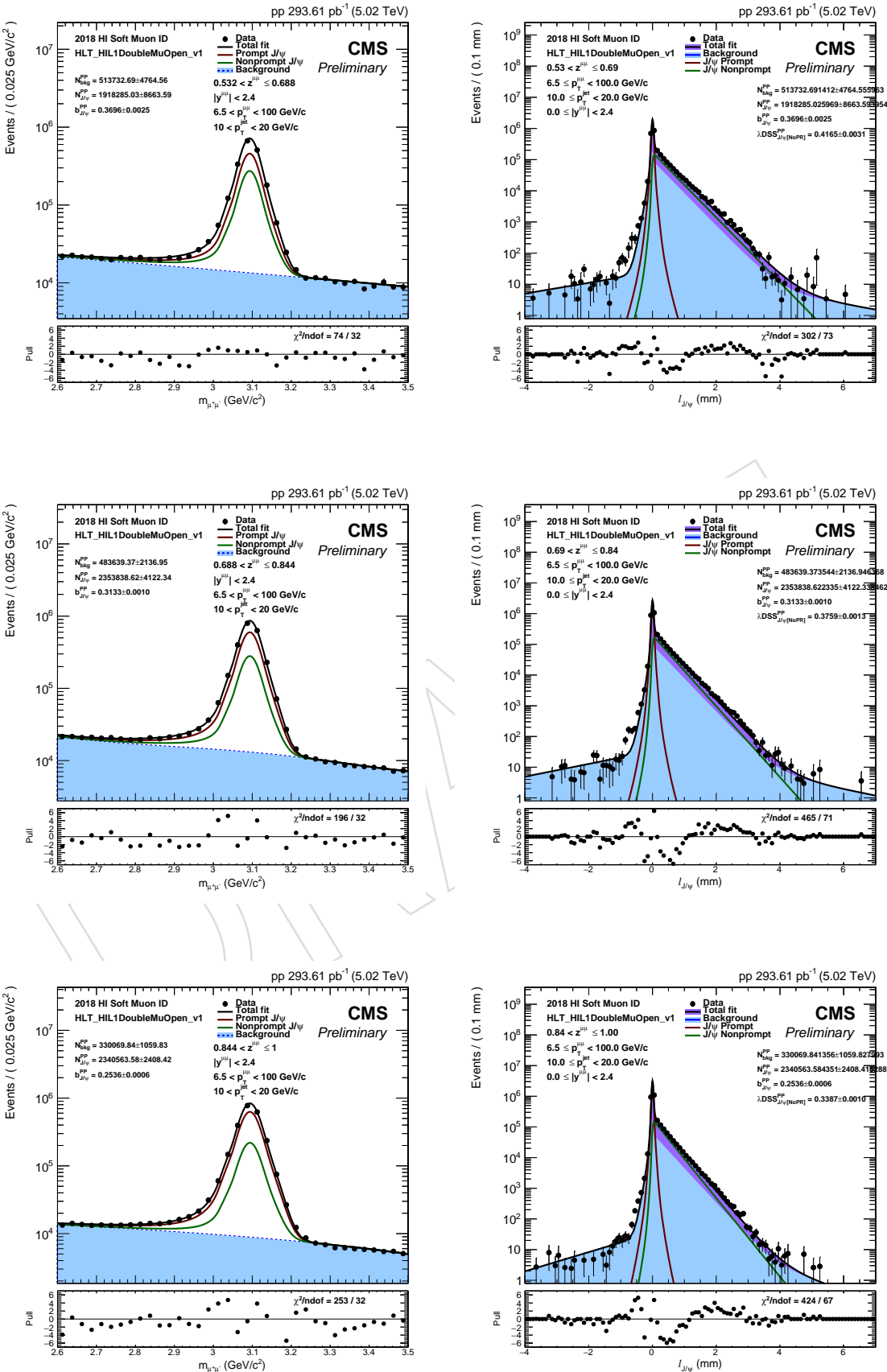




1028 **B.0.6 pp**

1029 The projections of the 2D fits in all z bins in pp collisions for $10 < p_T(\text{jet}) < 20 \text{ GeV}$.

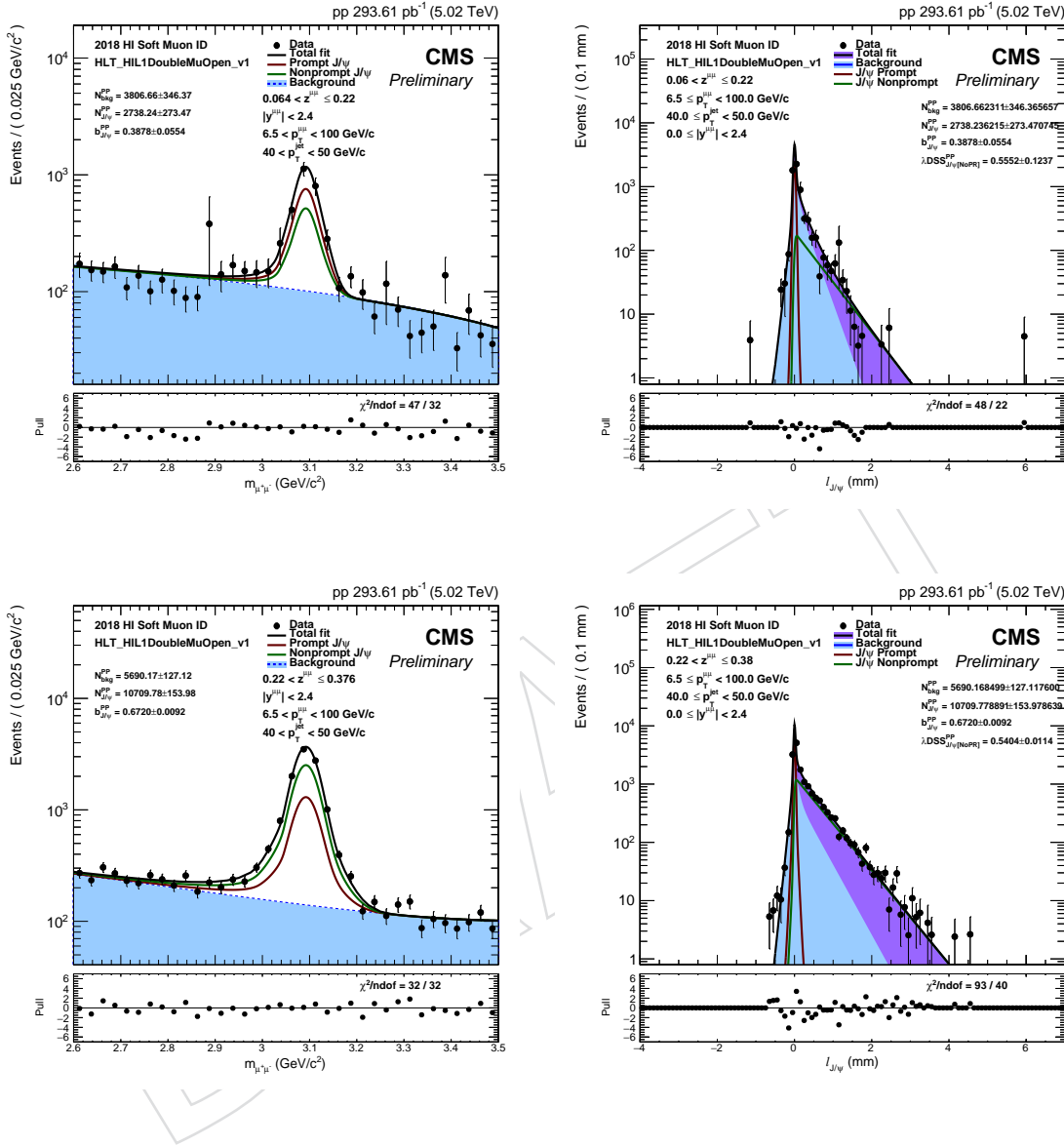


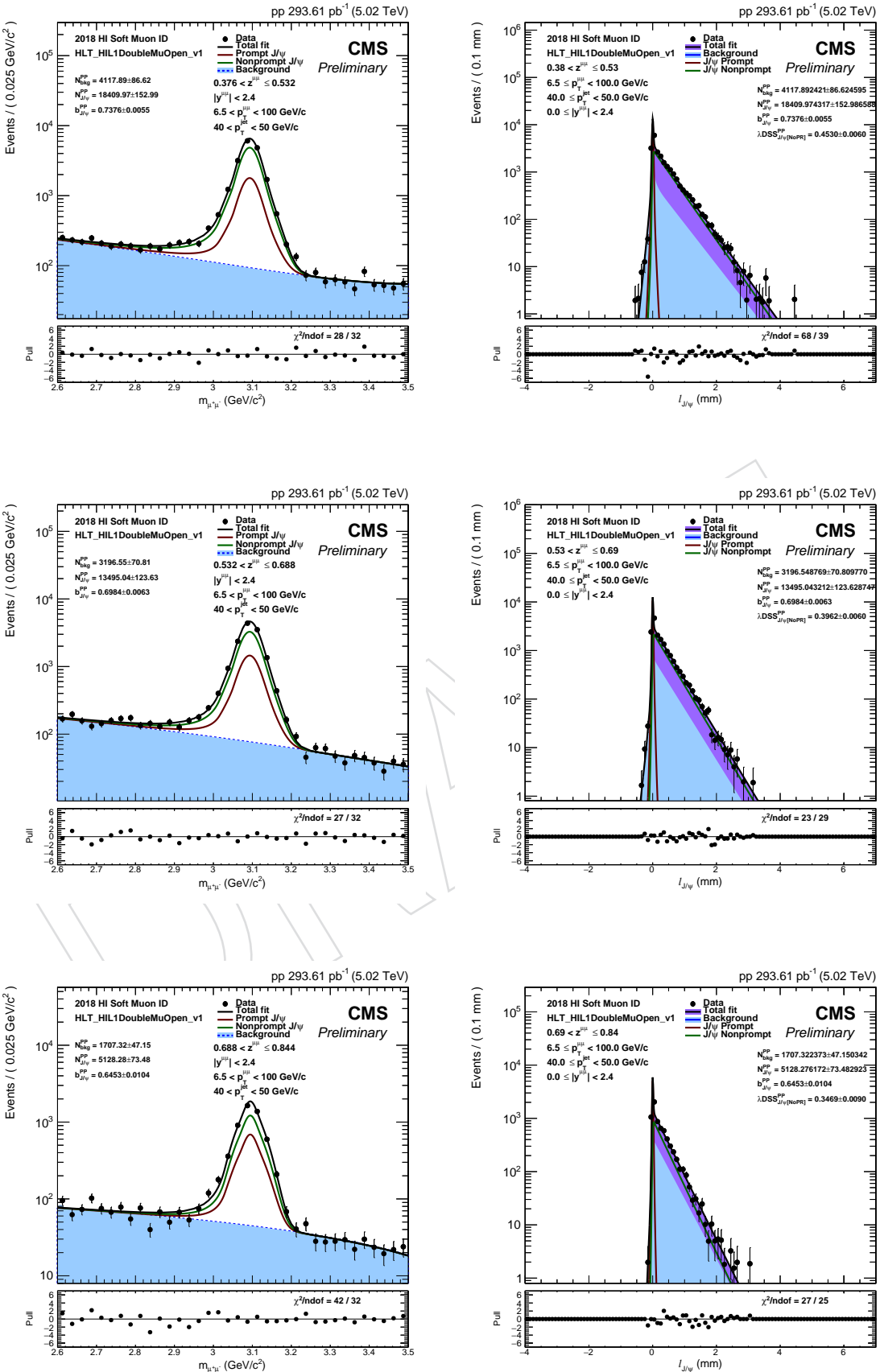


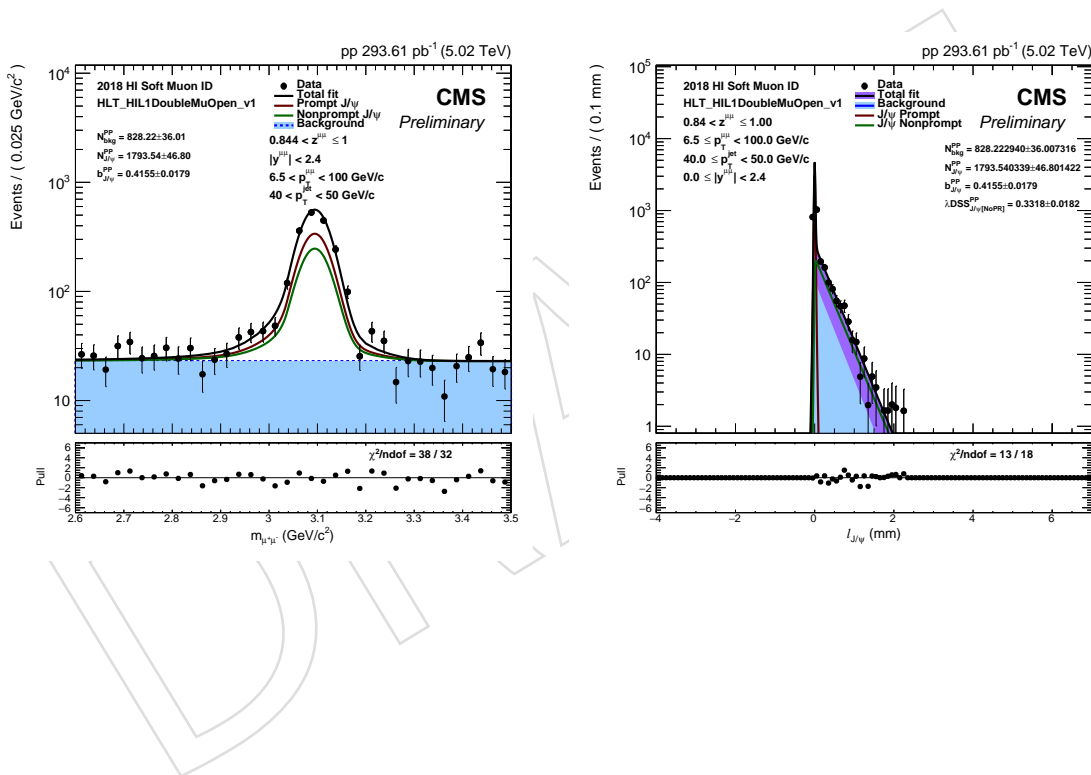
1030 **Fits for jets with $40 < p_T < 50 \text{ GeV}$**

1031 **B.0.7 pp**

1032 The projections of the 2D fits in all z bins in pp collisions for $40 < p_T(\text{jet}) < 50 \text{ GeV}$.

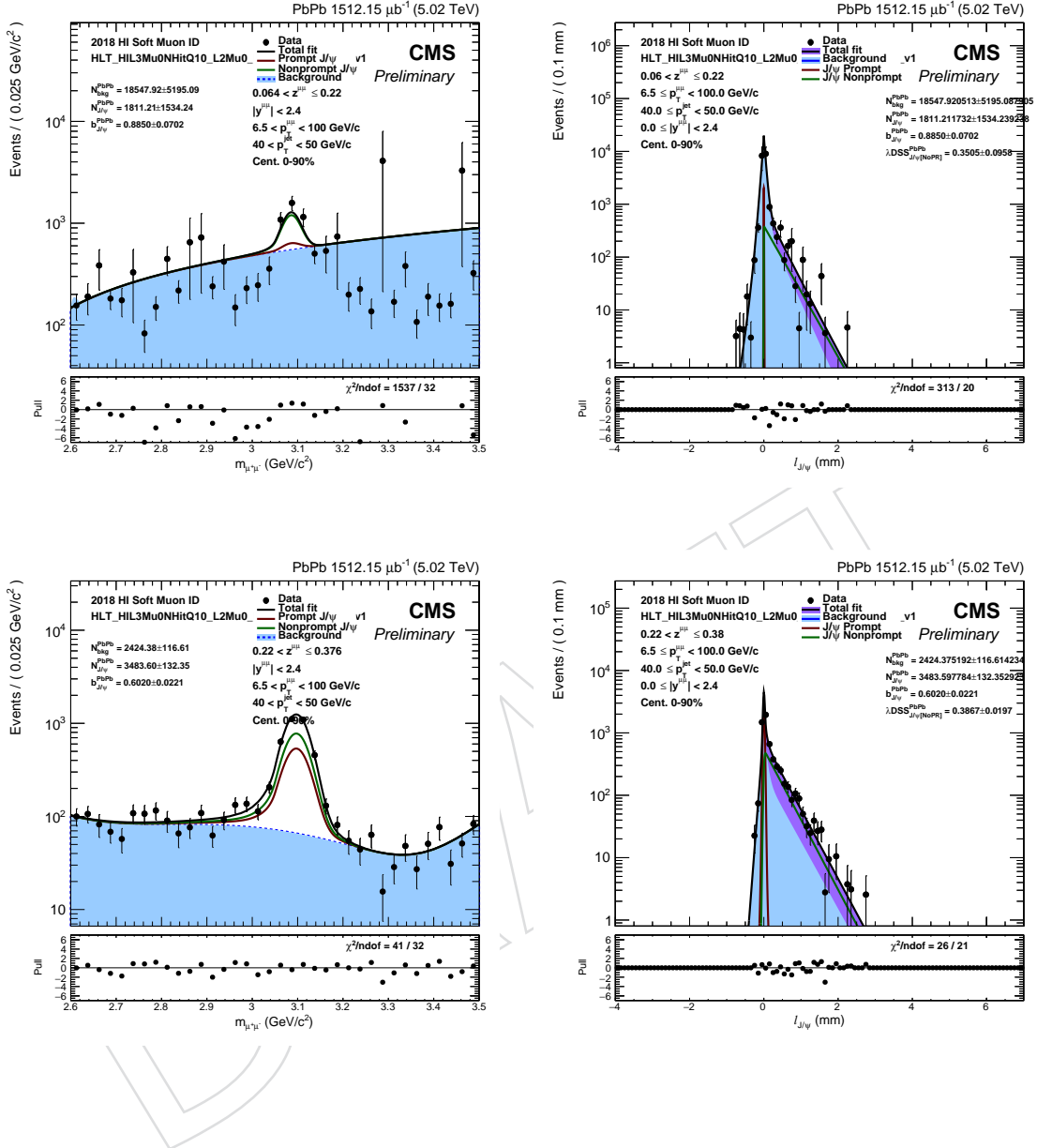






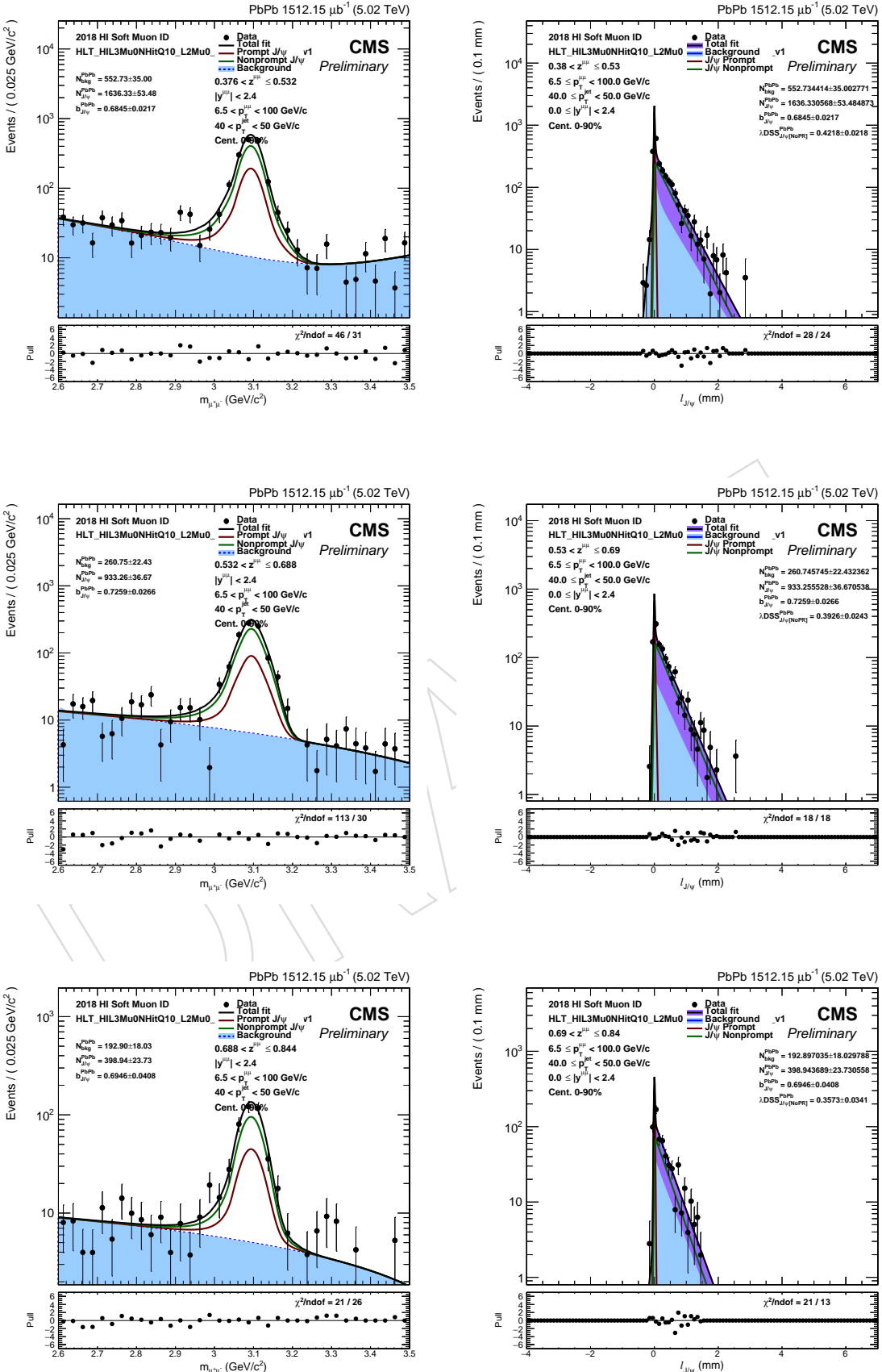
1033 **B.0.8 PbPb**

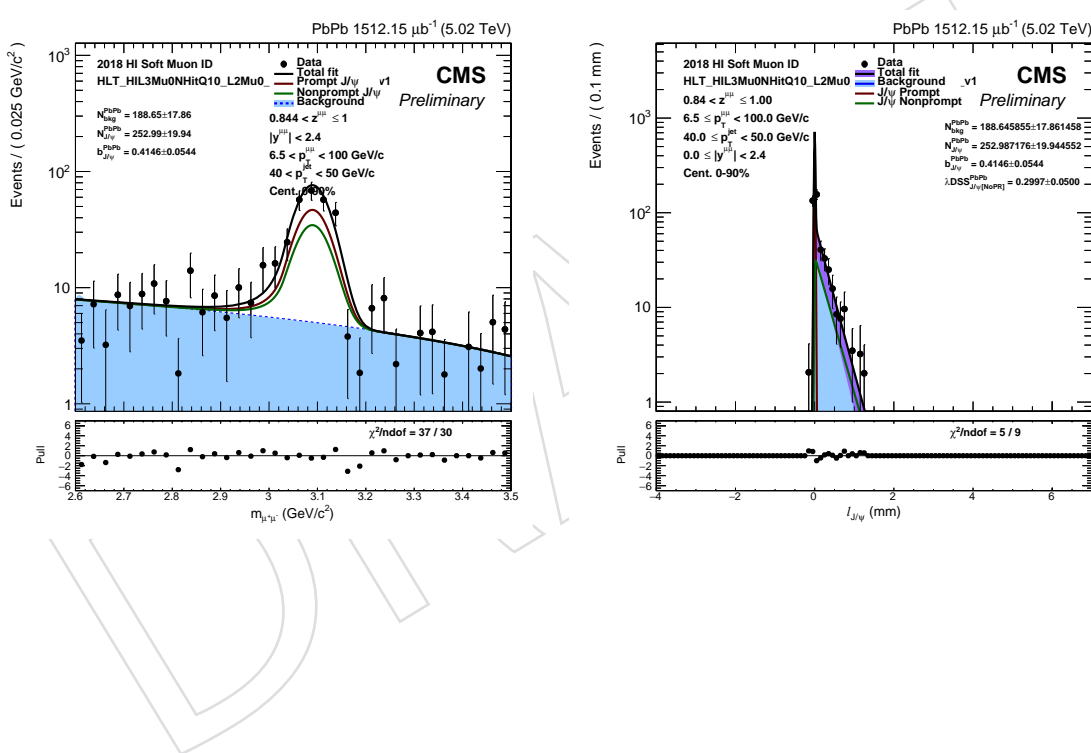
1034 The projections of the 2D fits in all z bins in PbPb collisions for $40 < p_T(jet) < 50$ GeV.



B. The 2D fit projections in all analysis bins

97



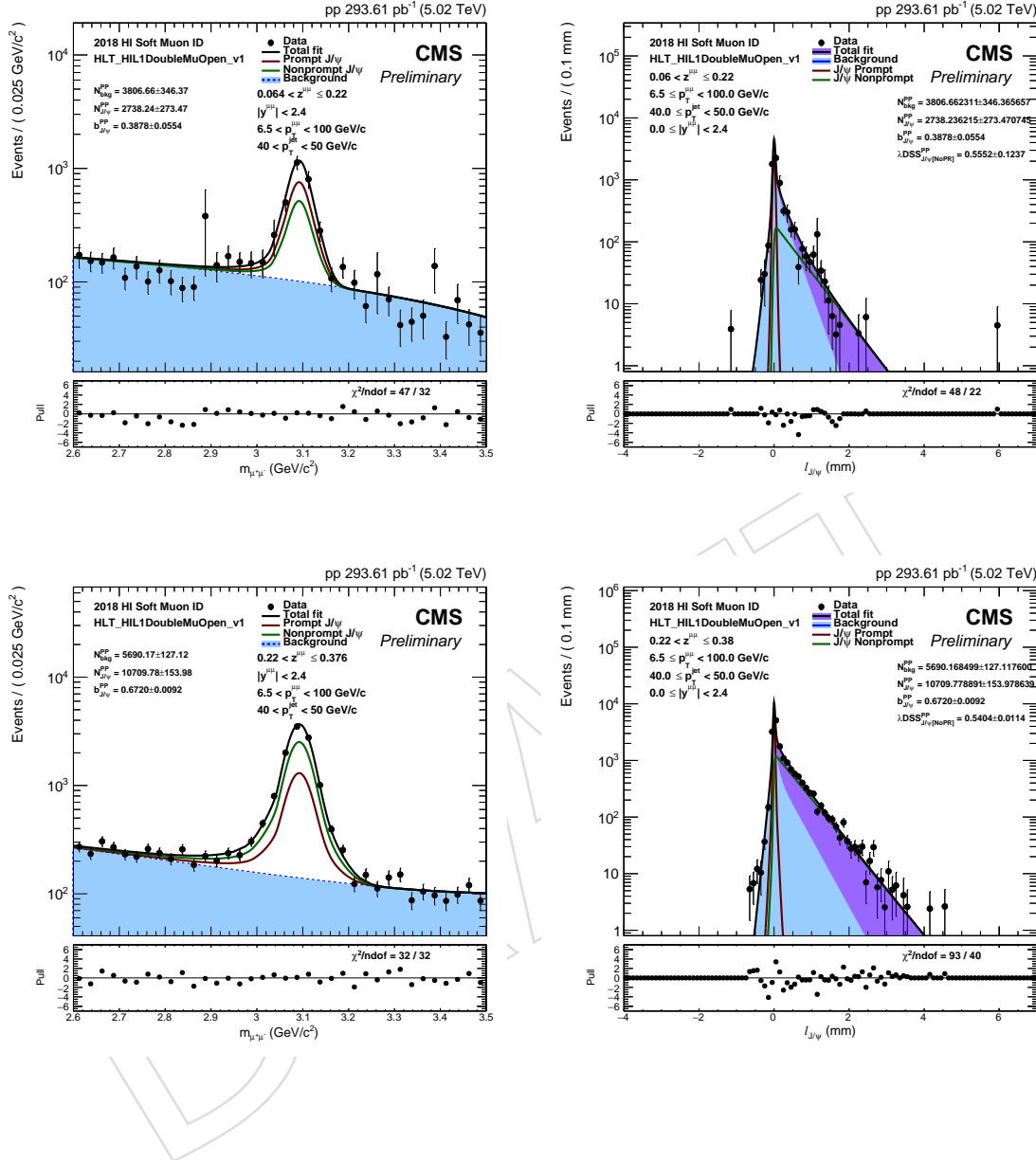


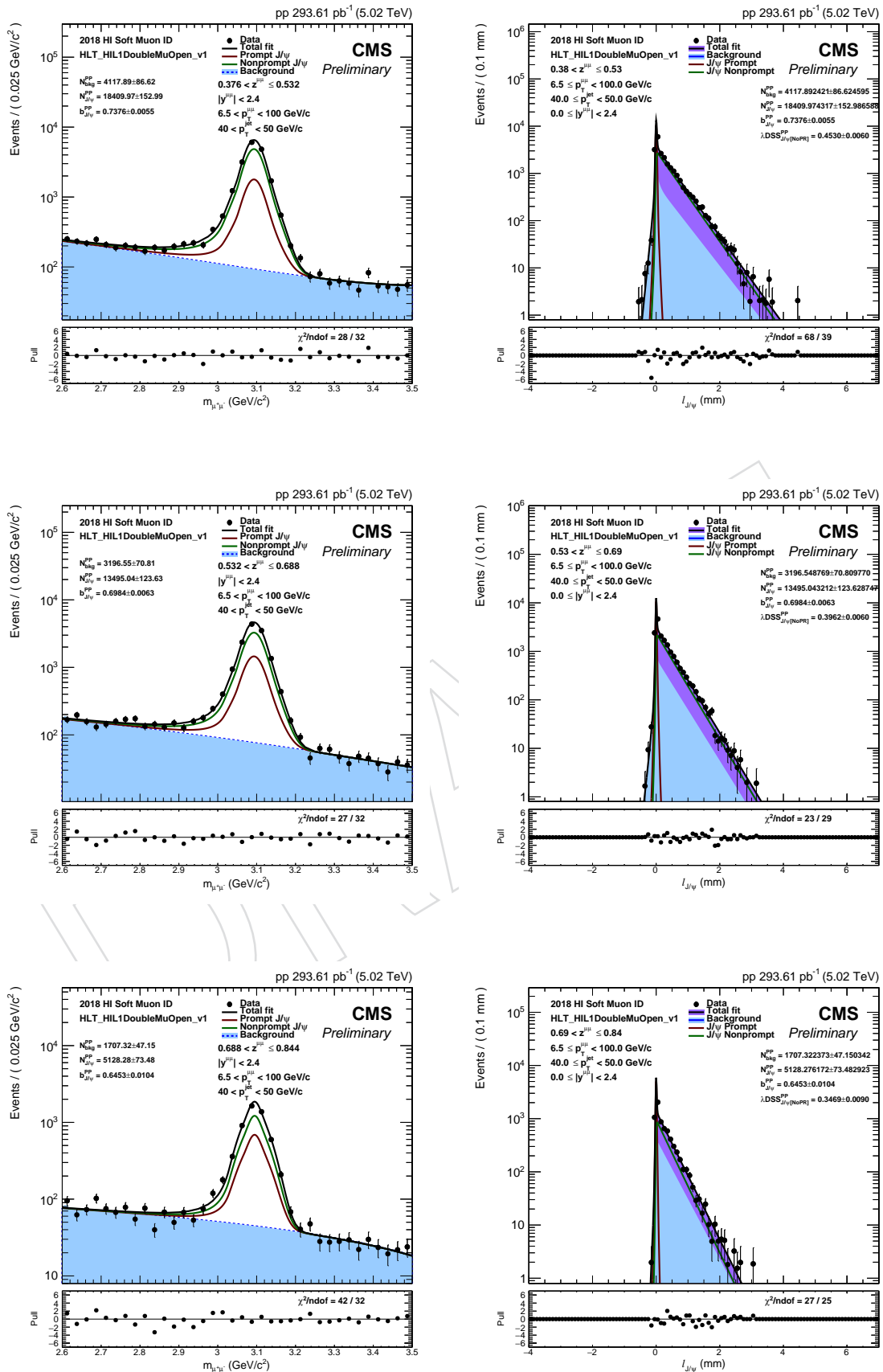
B. The 2D fit projections in all analysis bins

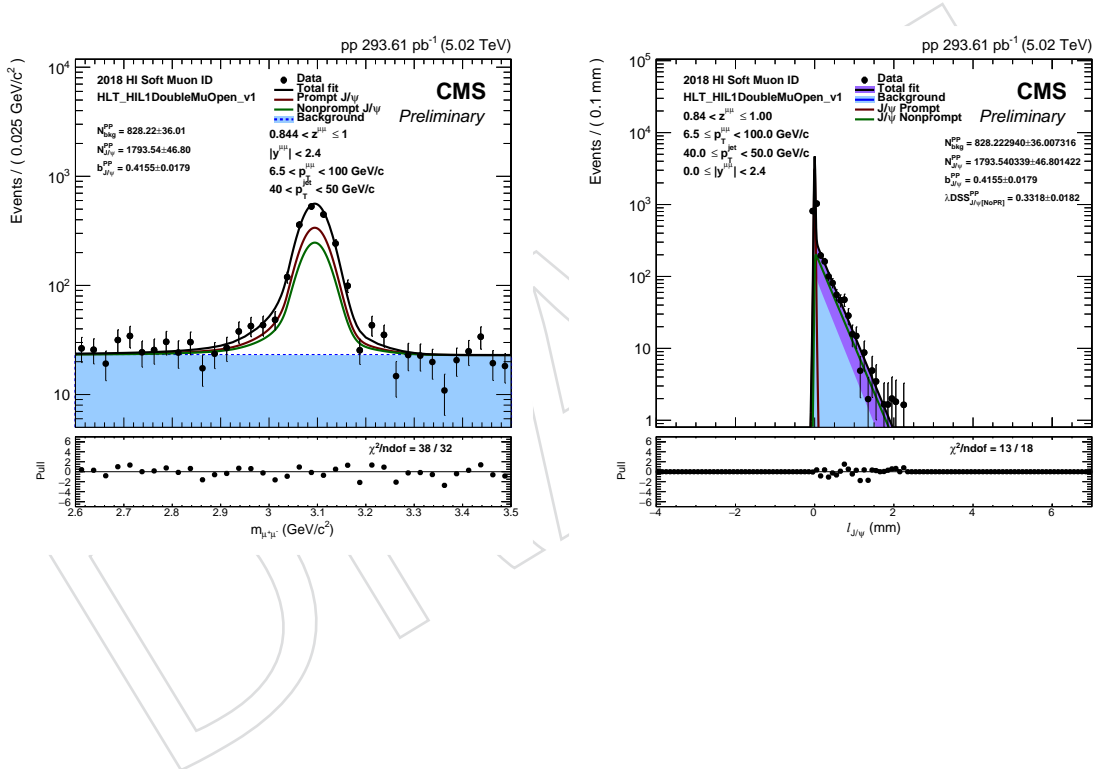
99

1035 B.0.9 pp

1036 The projections of the 2D fits in all z bins in pp collisions for $40 < p_T(\text{jet}) < 50 \text{ GeV}$.



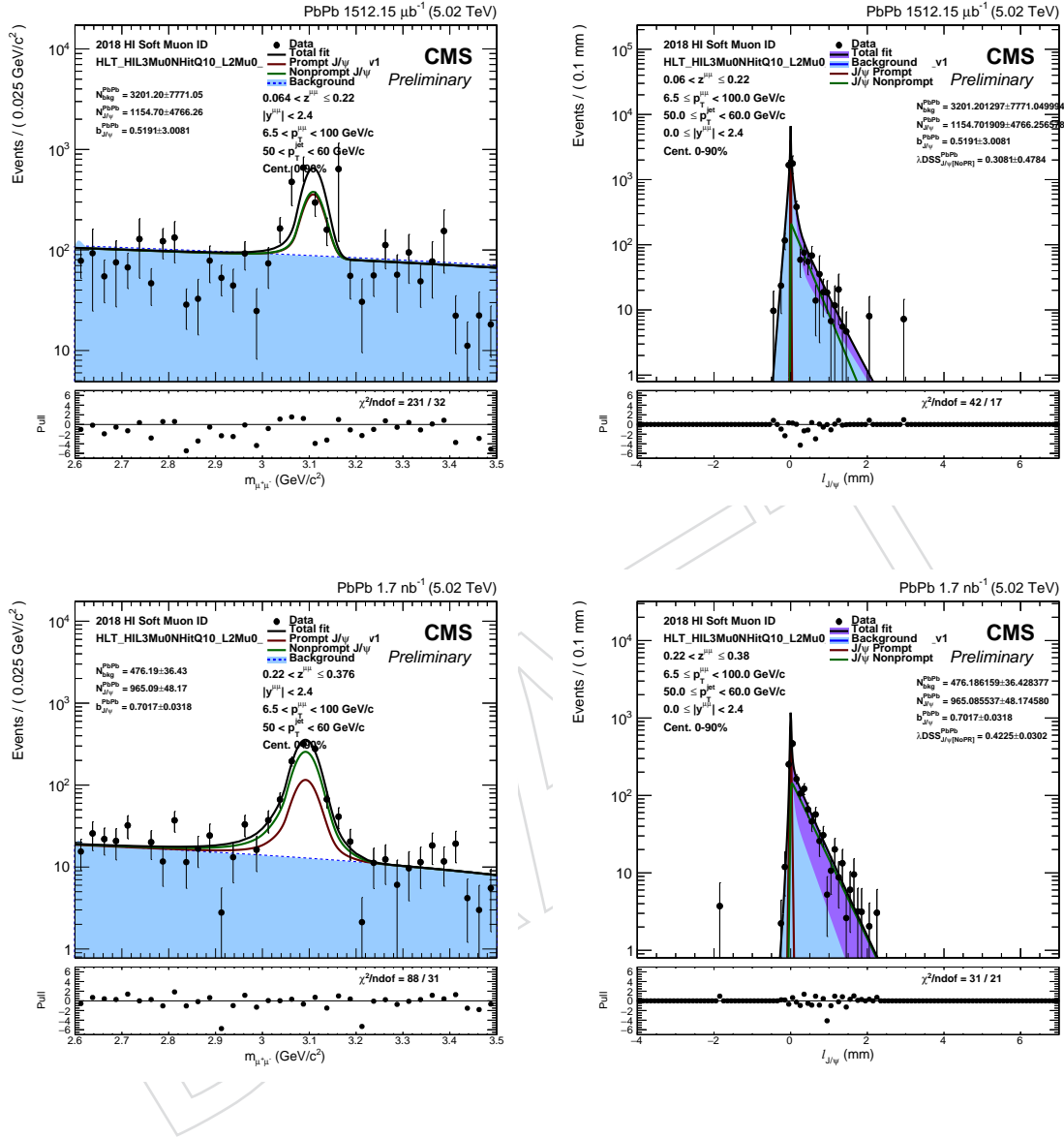


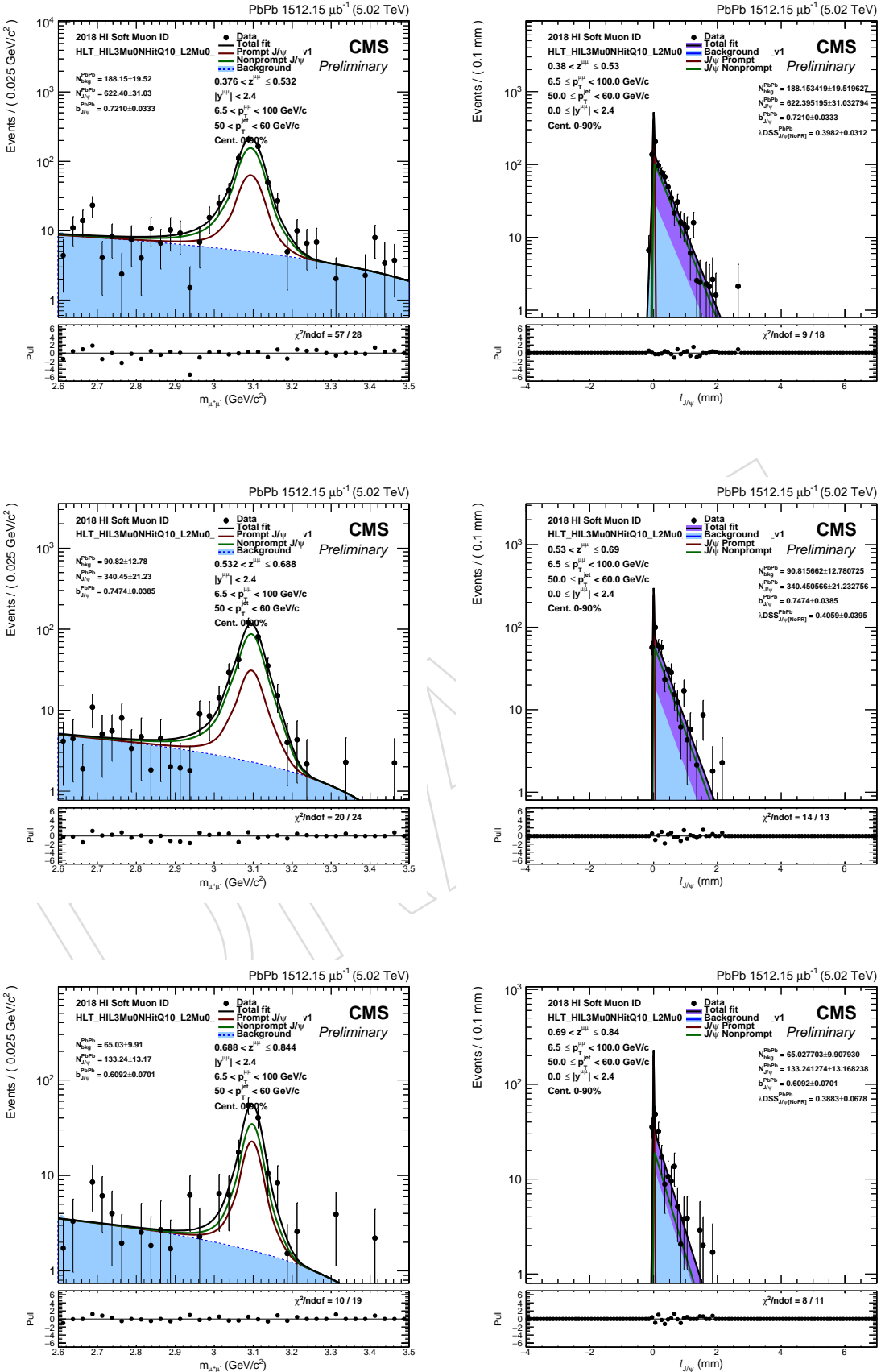


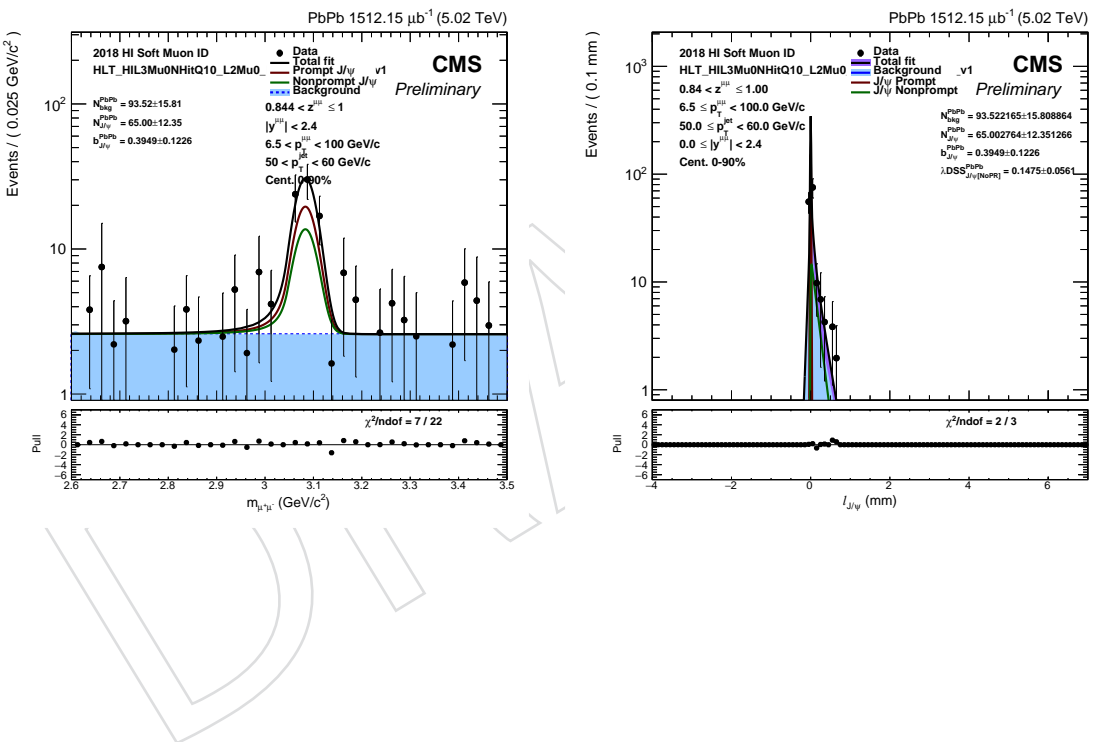
1037 **Fits for jets with $50 < p_T < 60 \text{ GeV}$**

1038 **B.0.10 PbPb**

1039 The projections of the 2D fits in all z bins in PbPb collisions for $50 < p_T(\text{jet}) < 60 \text{ GeV}$.

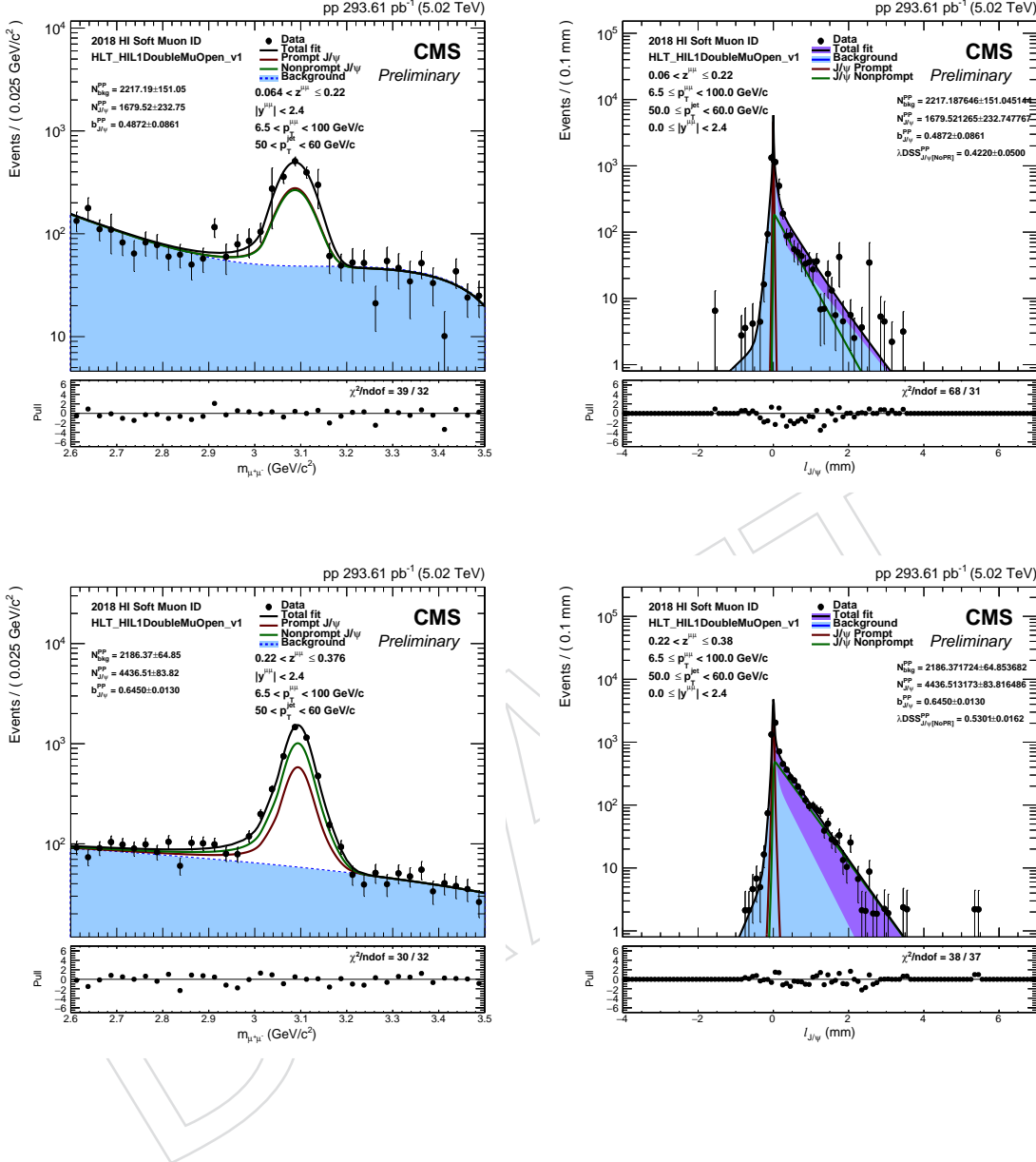


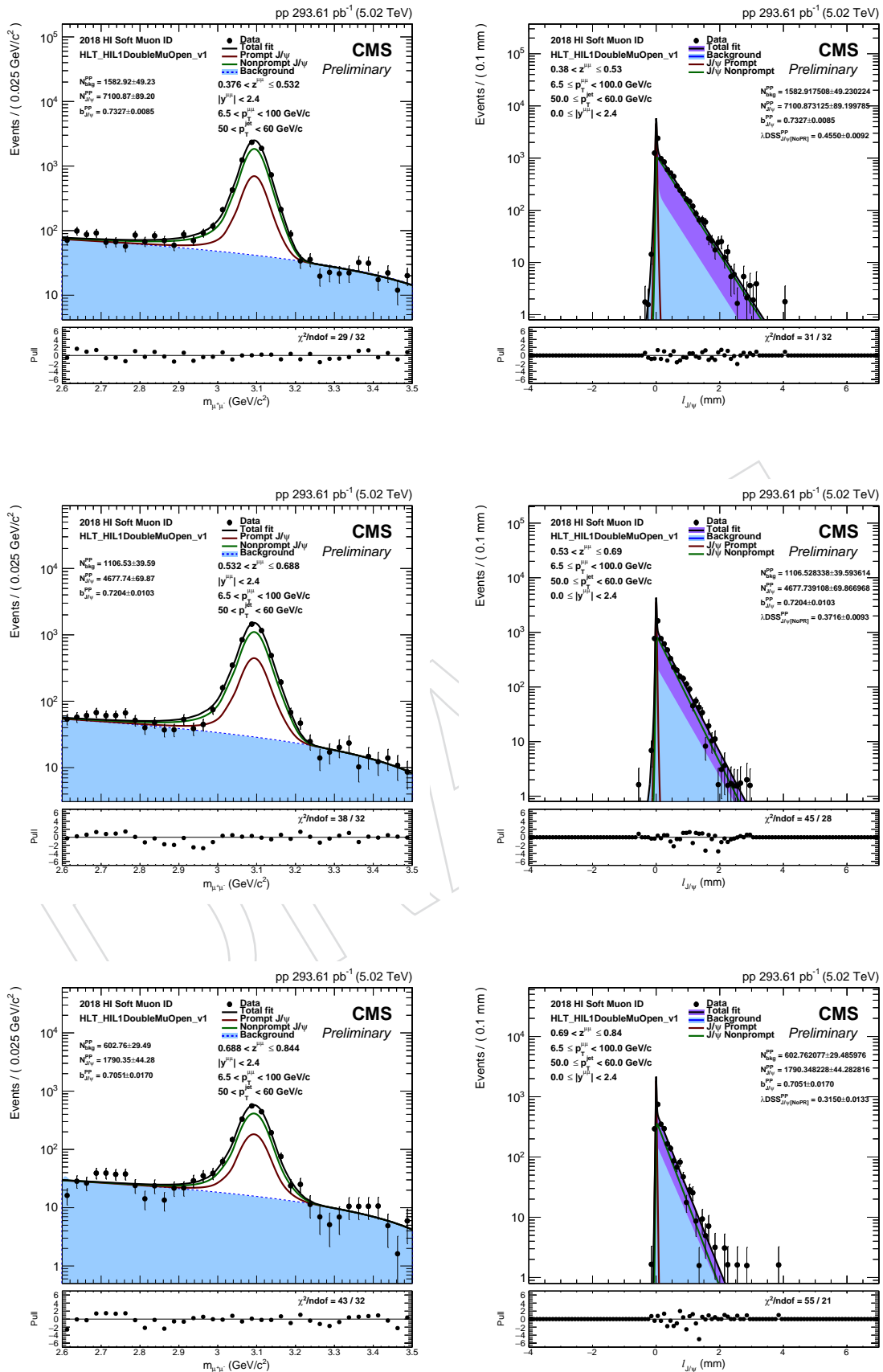


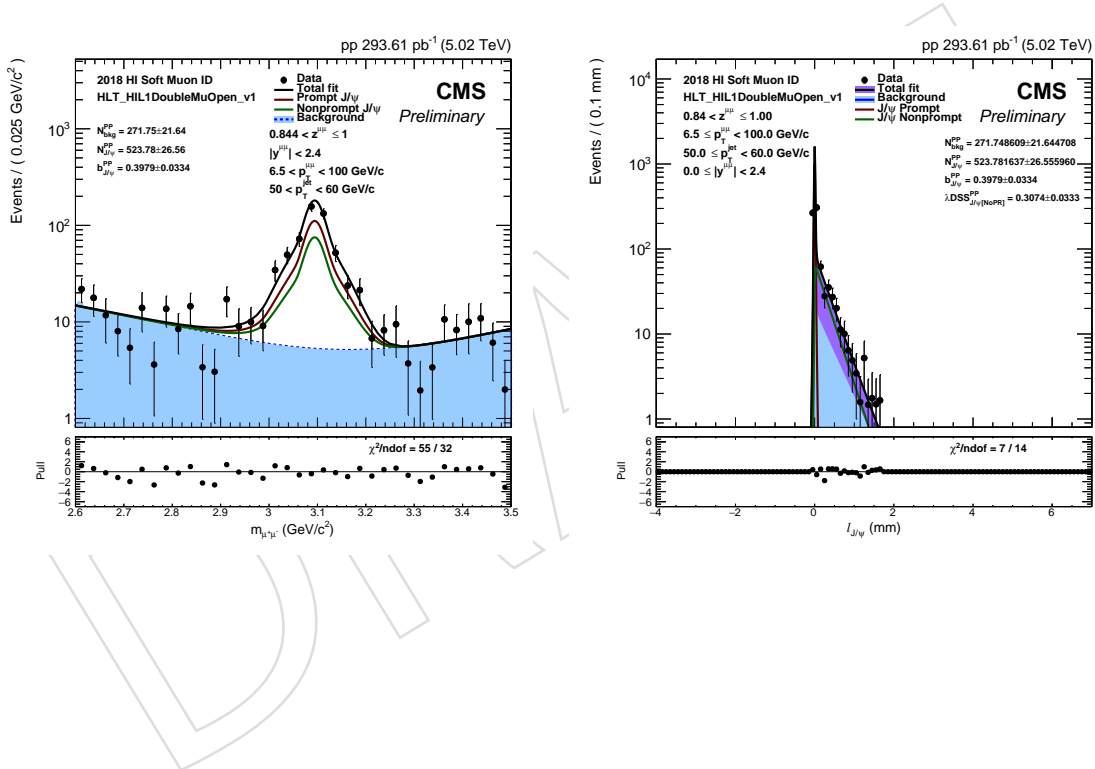


1040 **B.0.11 pp**

1041 The projections of the 2D fits in all z bins in pp collisions for $50 < p_T(\text{jet}) < 60 \text{ GeV}$.



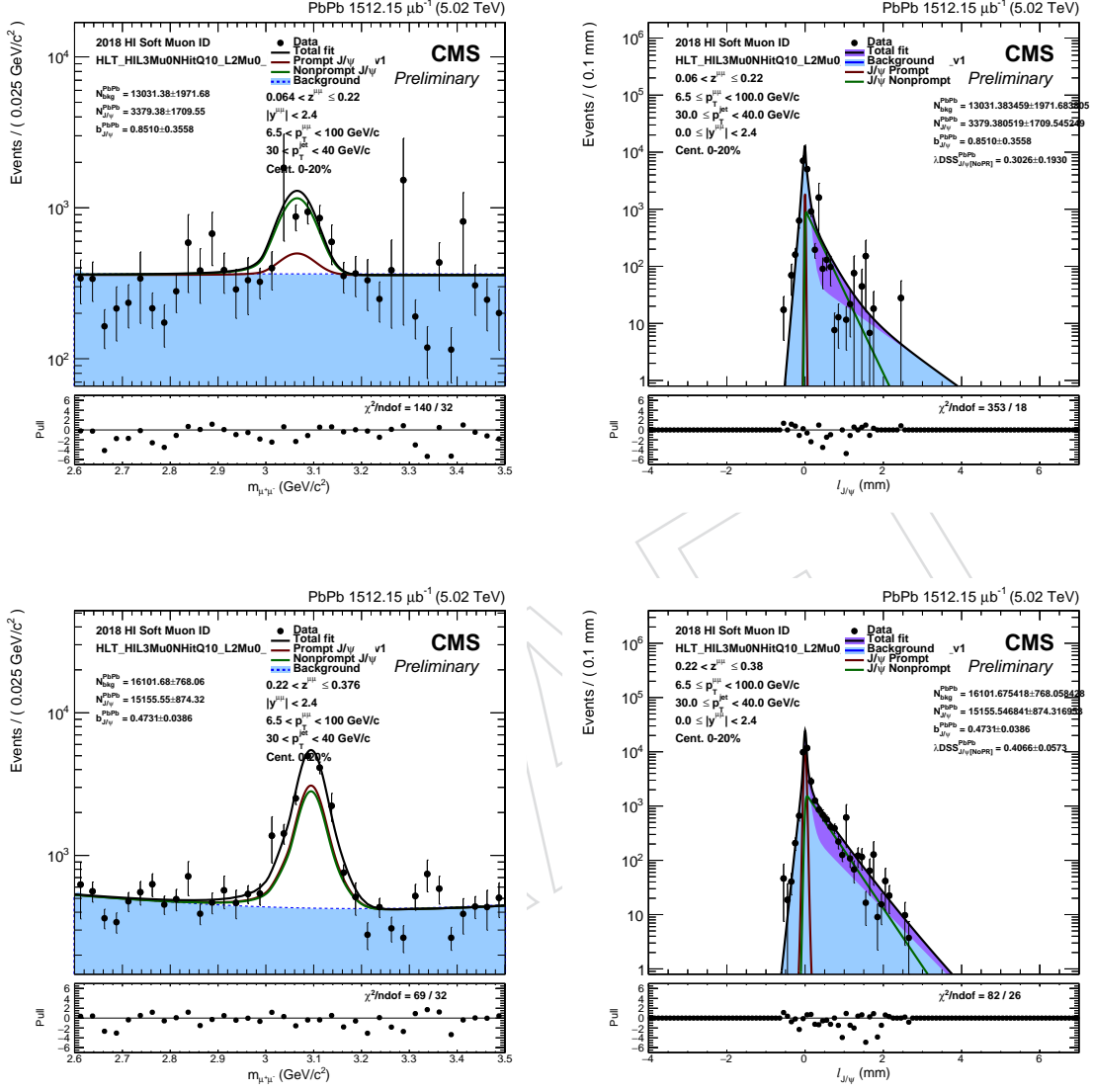


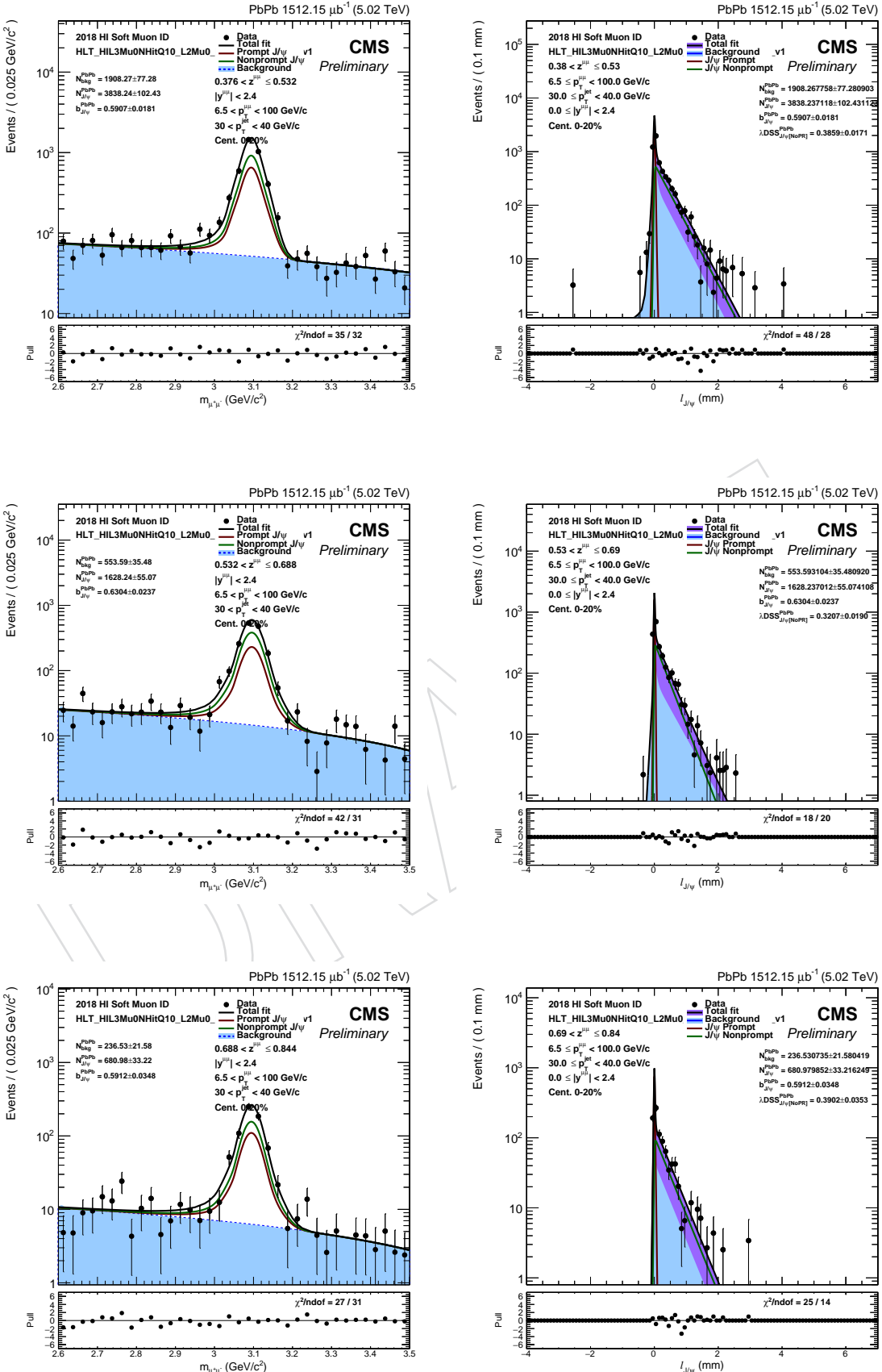


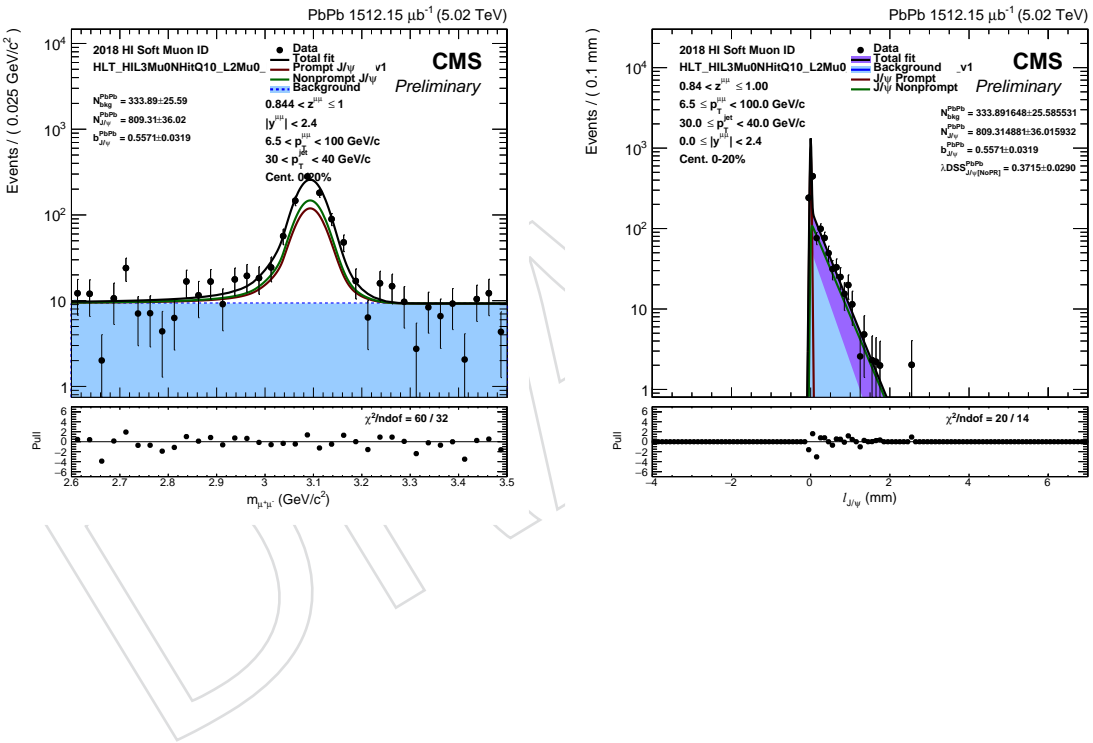
1042 **Fits for jets with $30 < p_T < 40 \text{ GeV}$**

1043 **B.0.12 PbPb**

1044 The projections of the 2D fits in all z bins in PbPb collisions for $30 < p_T(\text{jet}) < 40 \text{ GeV}$, for the
1045 0-20% centrality selection.



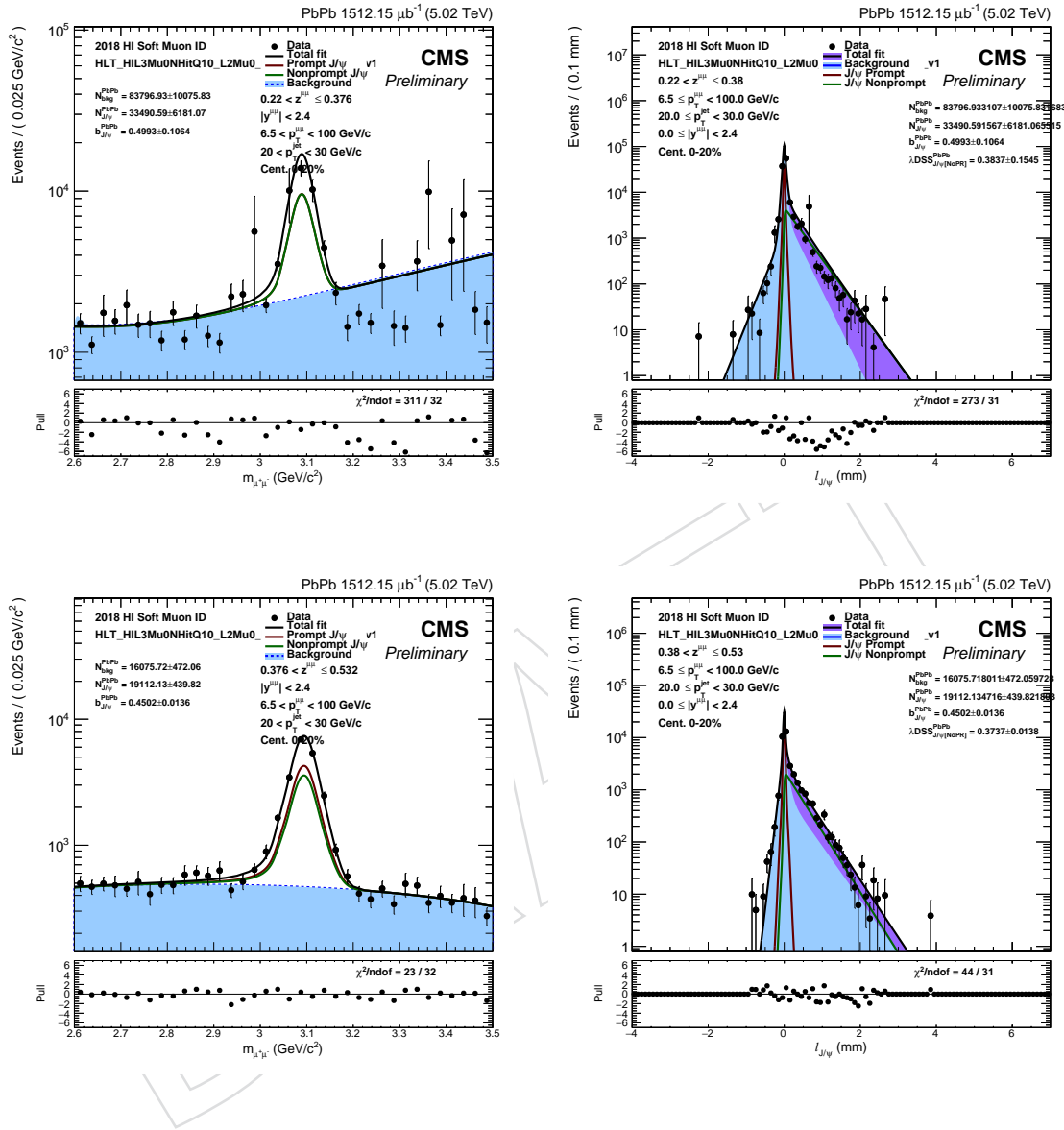


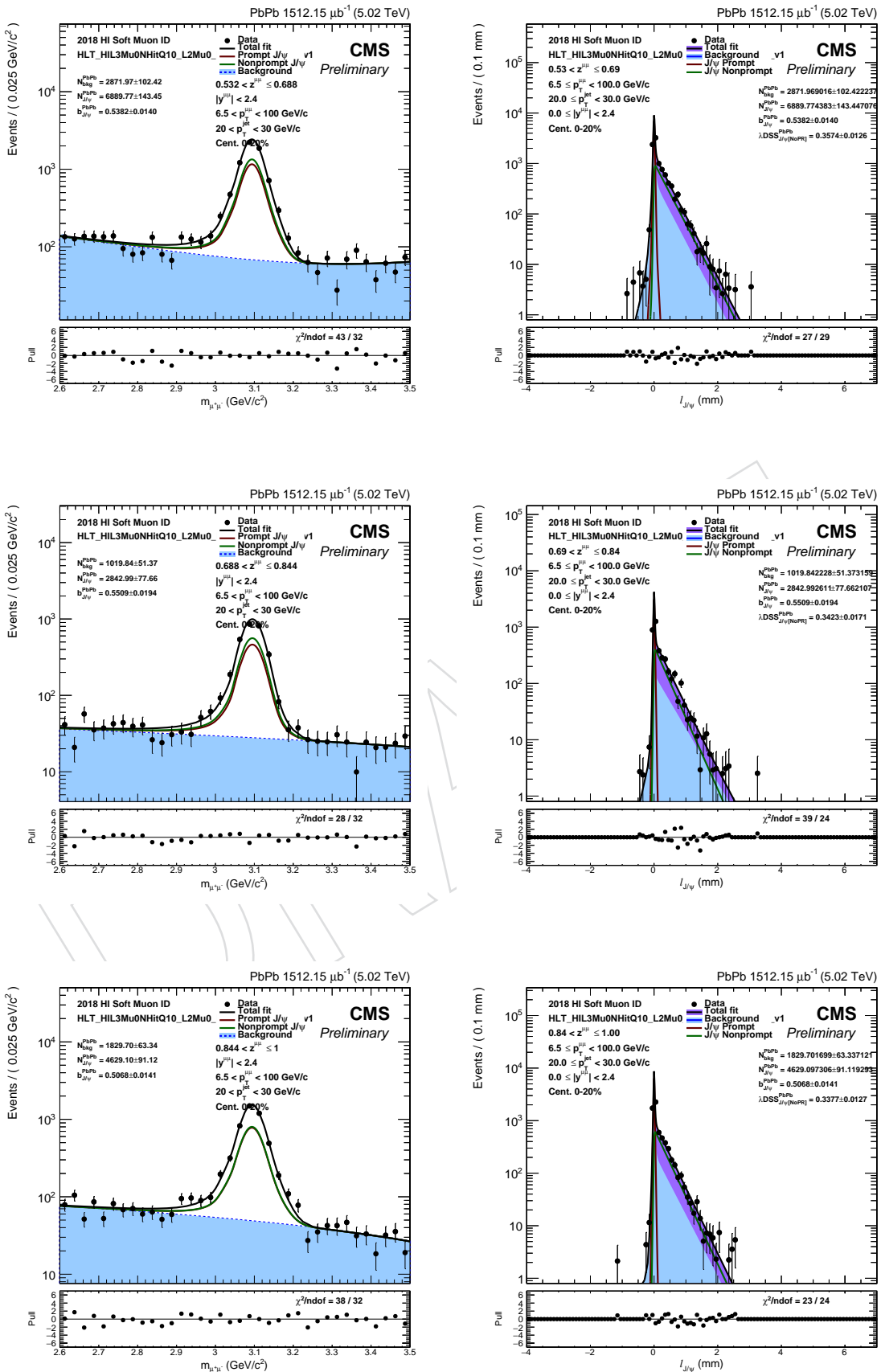


1046 **Fits for jets with $20 < p_T < 30 \text{ GeV}$**

1047 **B.0.13 PbPb**

1048 The projections of the 2D fits in all z bins in PbPb collisions for $20 < p_T(\text{jet}) < 30 \text{ GeV}$.

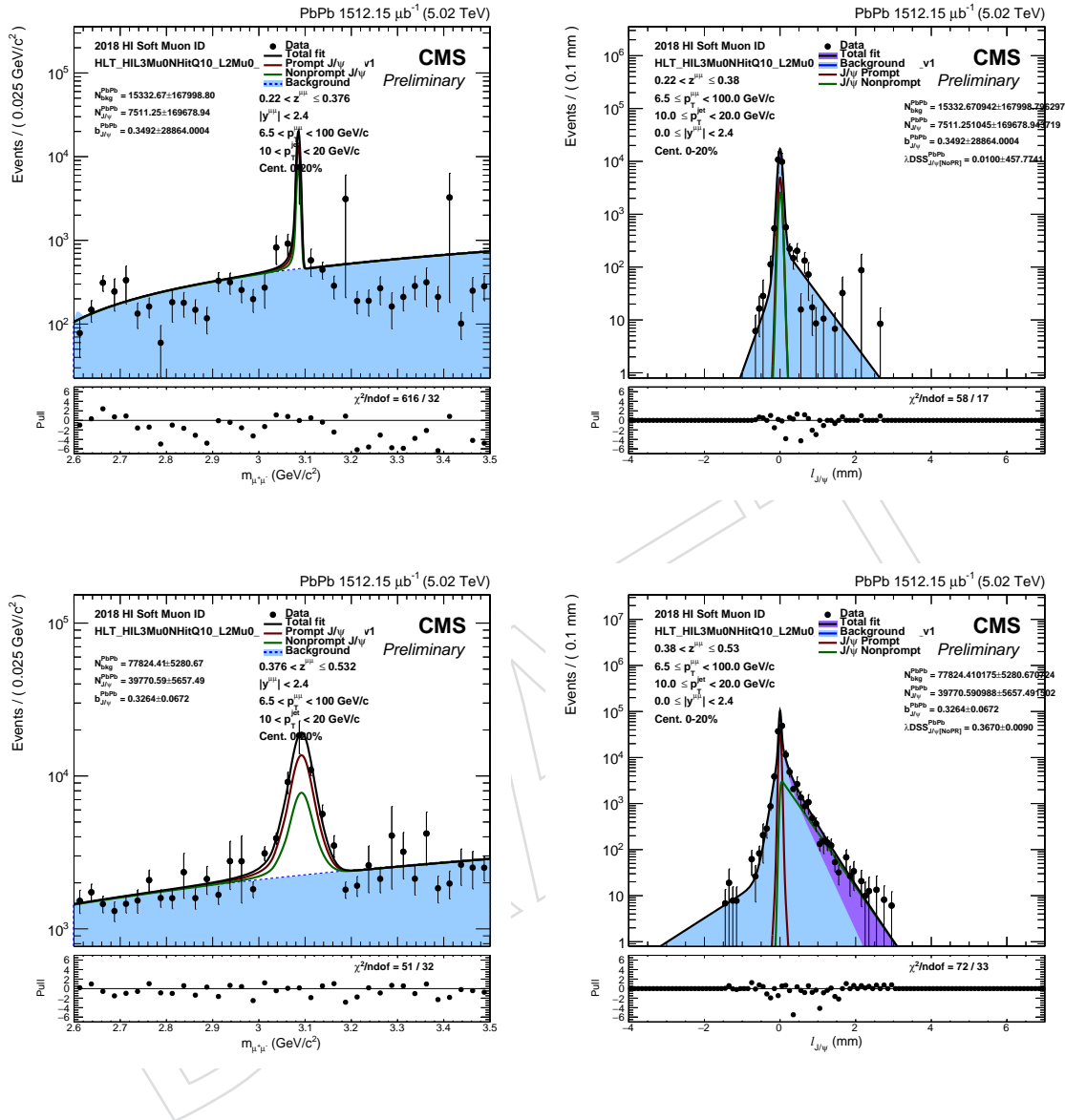


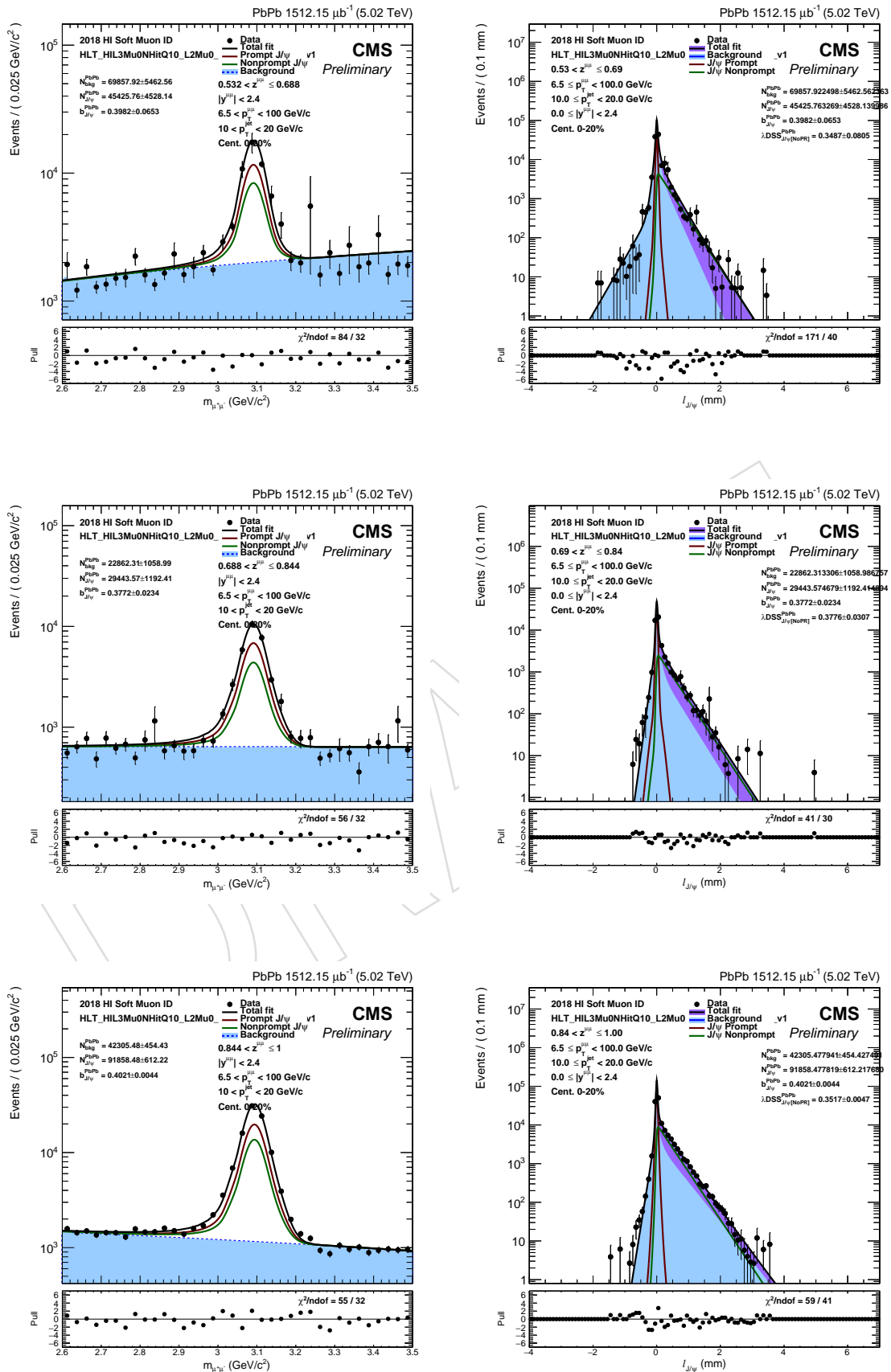


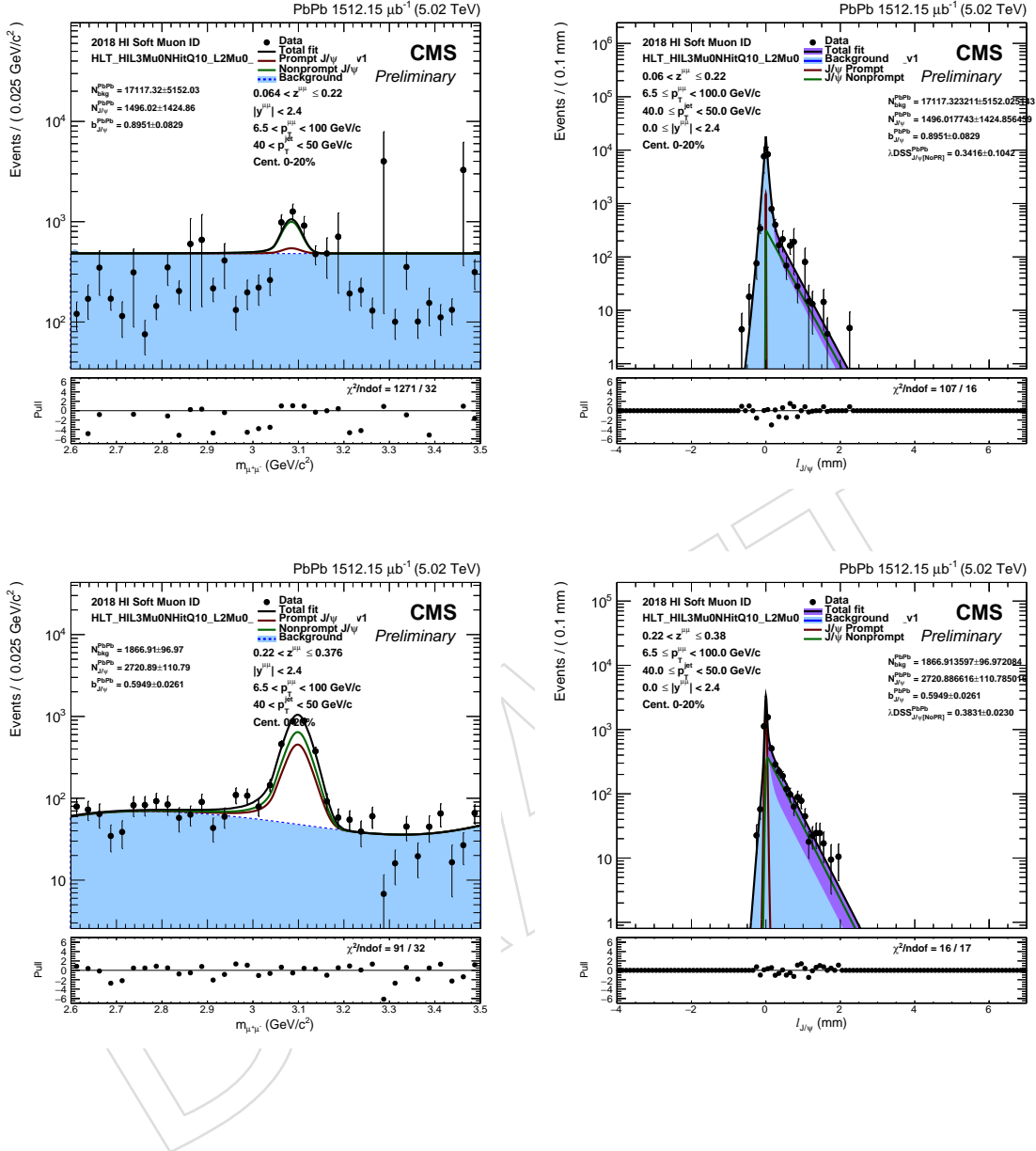
1049 **Fits for jets with $10 < p_T < 20 \text{ GeV}$**

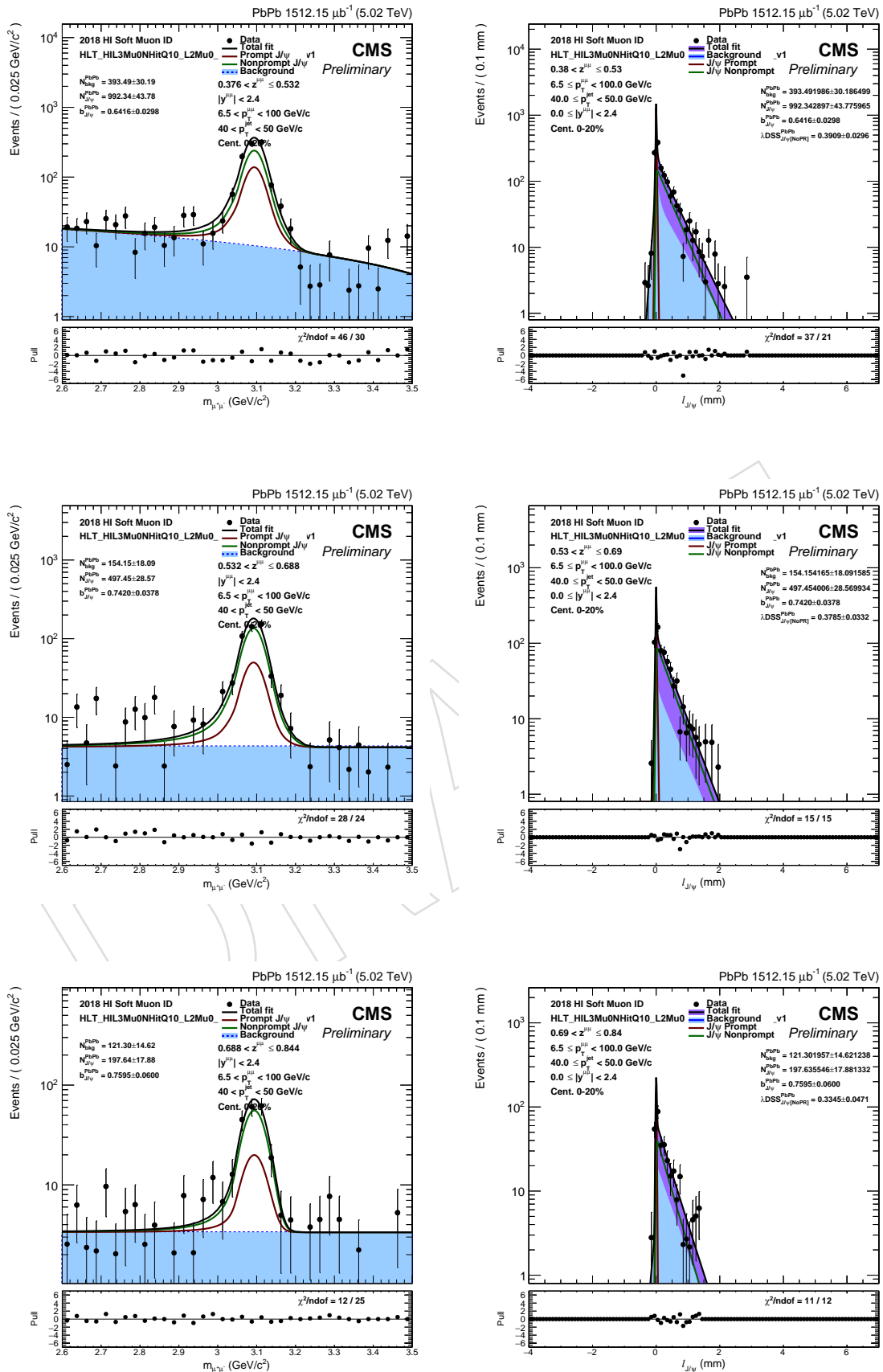
1050 **B.0.14 PbPb**

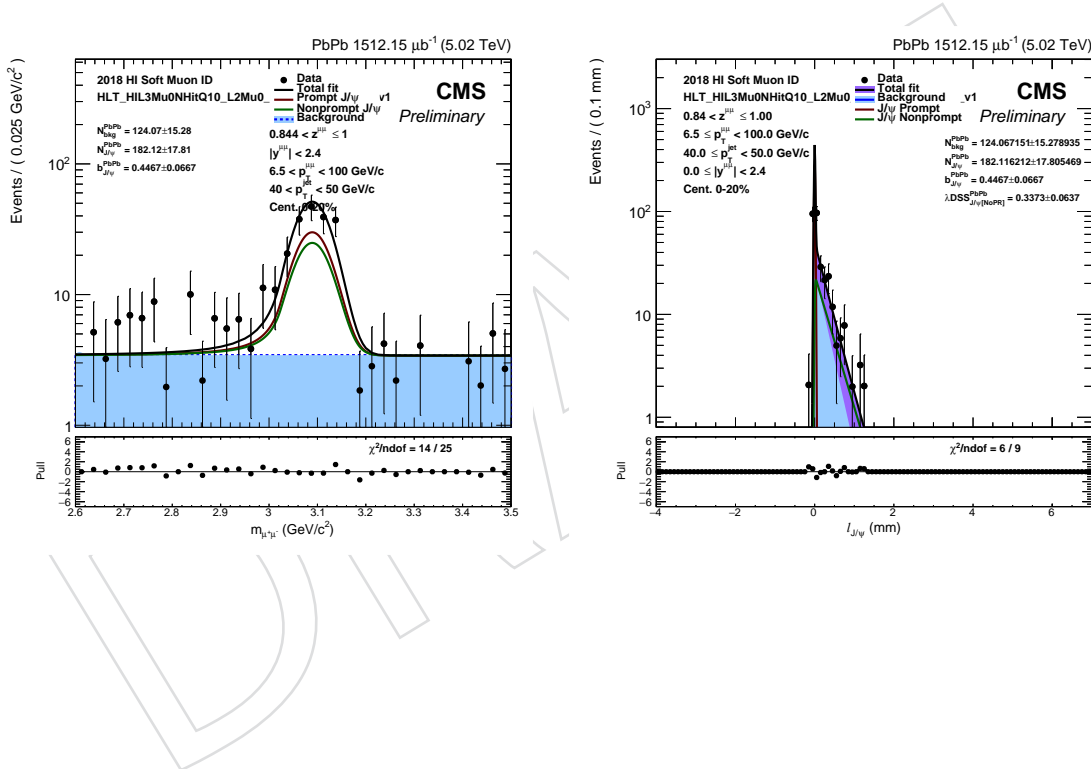
1051 The projections of the 2D fits in all z bins in PbPb collisions for $10 < p_T(\text{jet}) < 20 \text{ GeV}$.





1052 **B.0.15 PbPb**1053 The projections of the 2D fits in all z bins in PbPb collisions for $40 < p_T(\text{jet}) < 50 \text{ GeV}$.

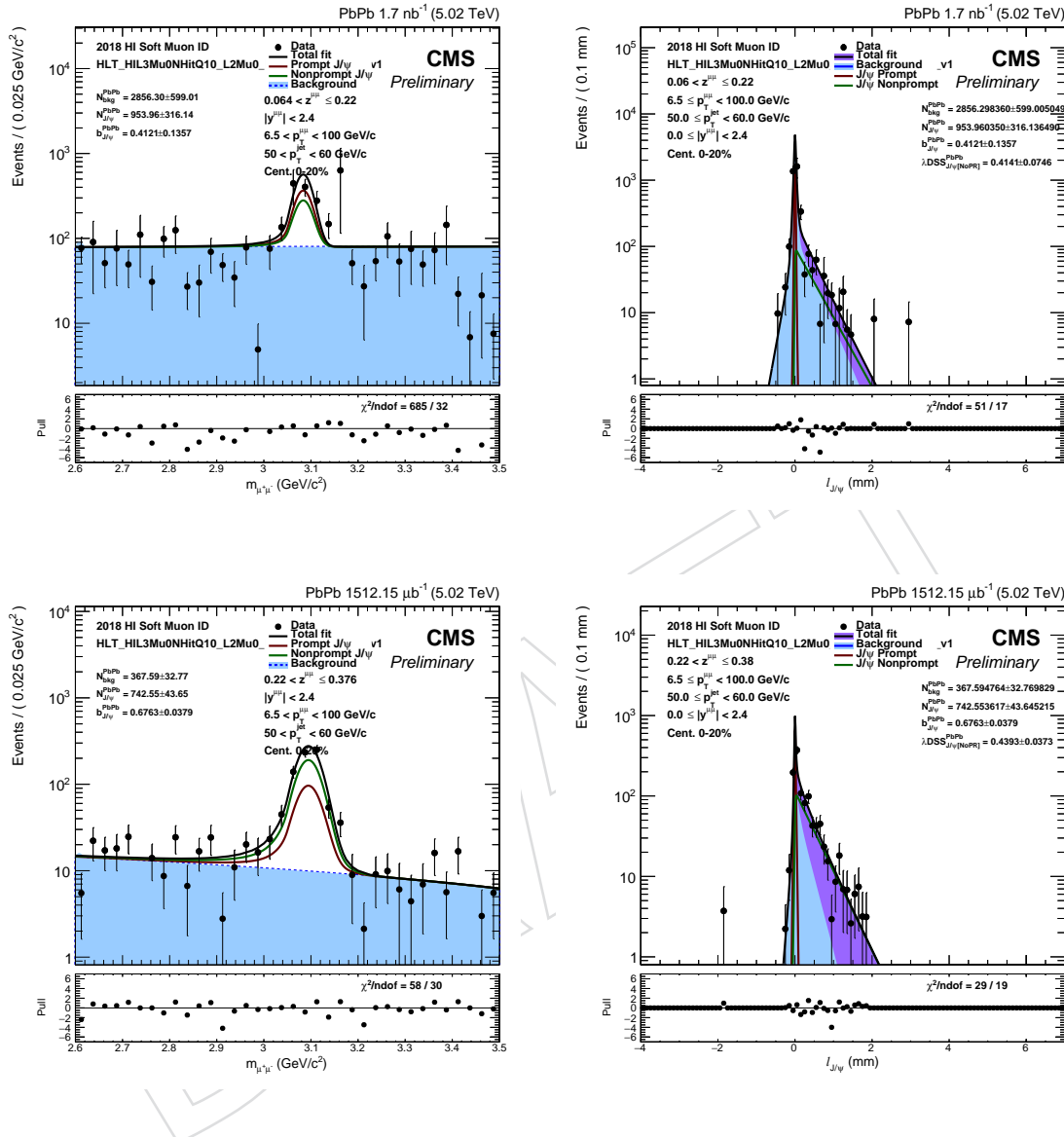


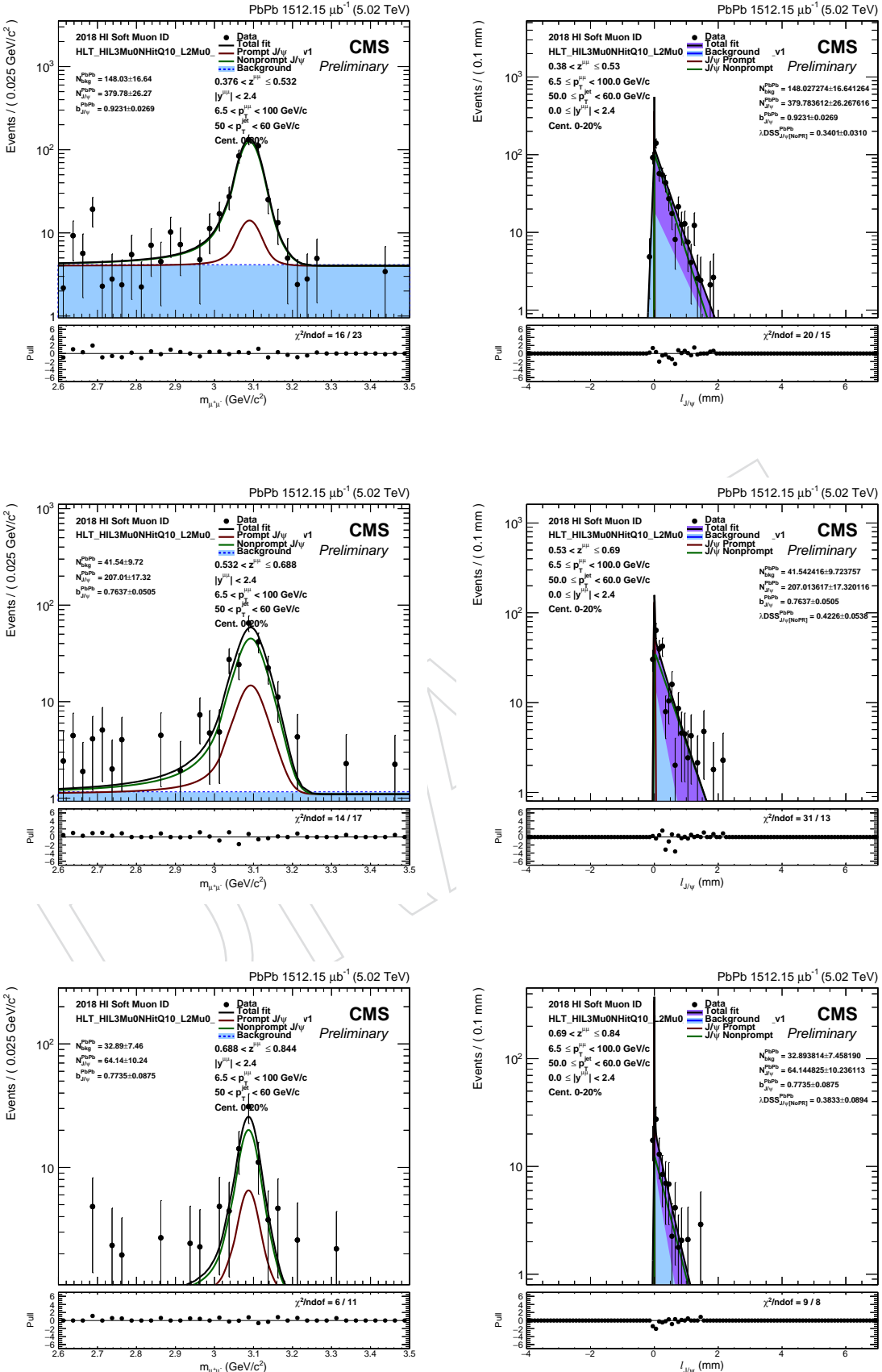


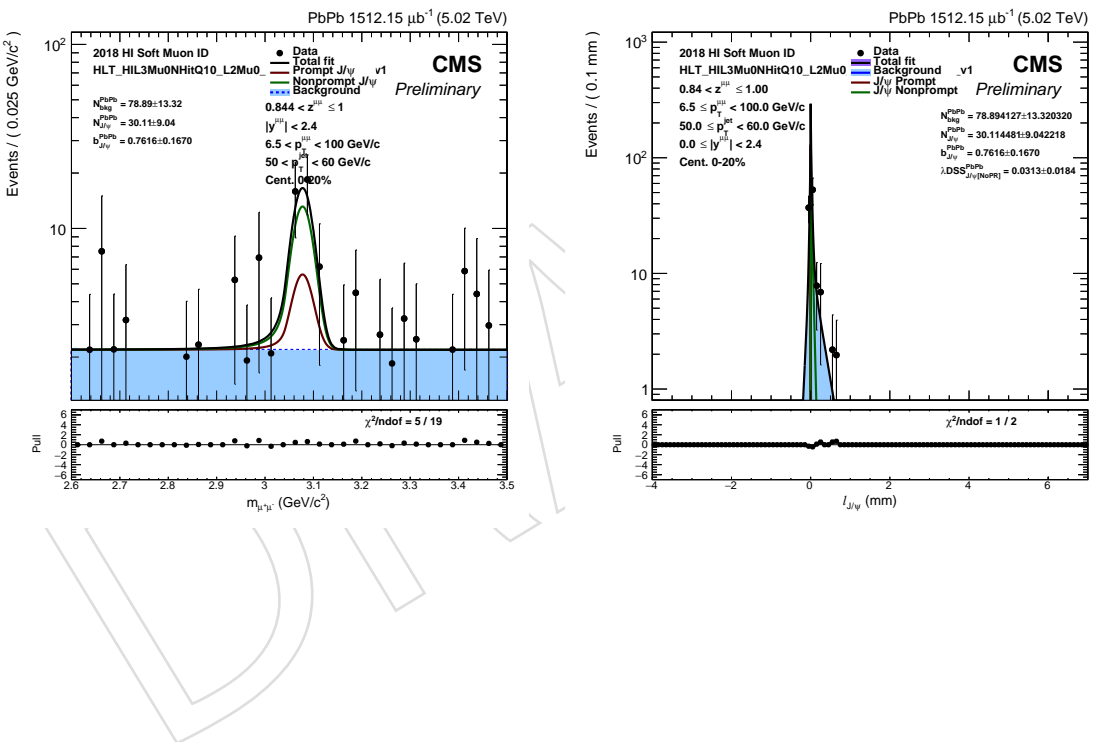
1054 **Fits for jets with $50 < p_T < 60 \text{ GeV}$**

1055 **B.0.16 PbPb**

1056 The projections of the 2D fits in all z bins in PbPb collisions for $50 < p_T(\text{jet}) < 60 \text{ GeV}$.



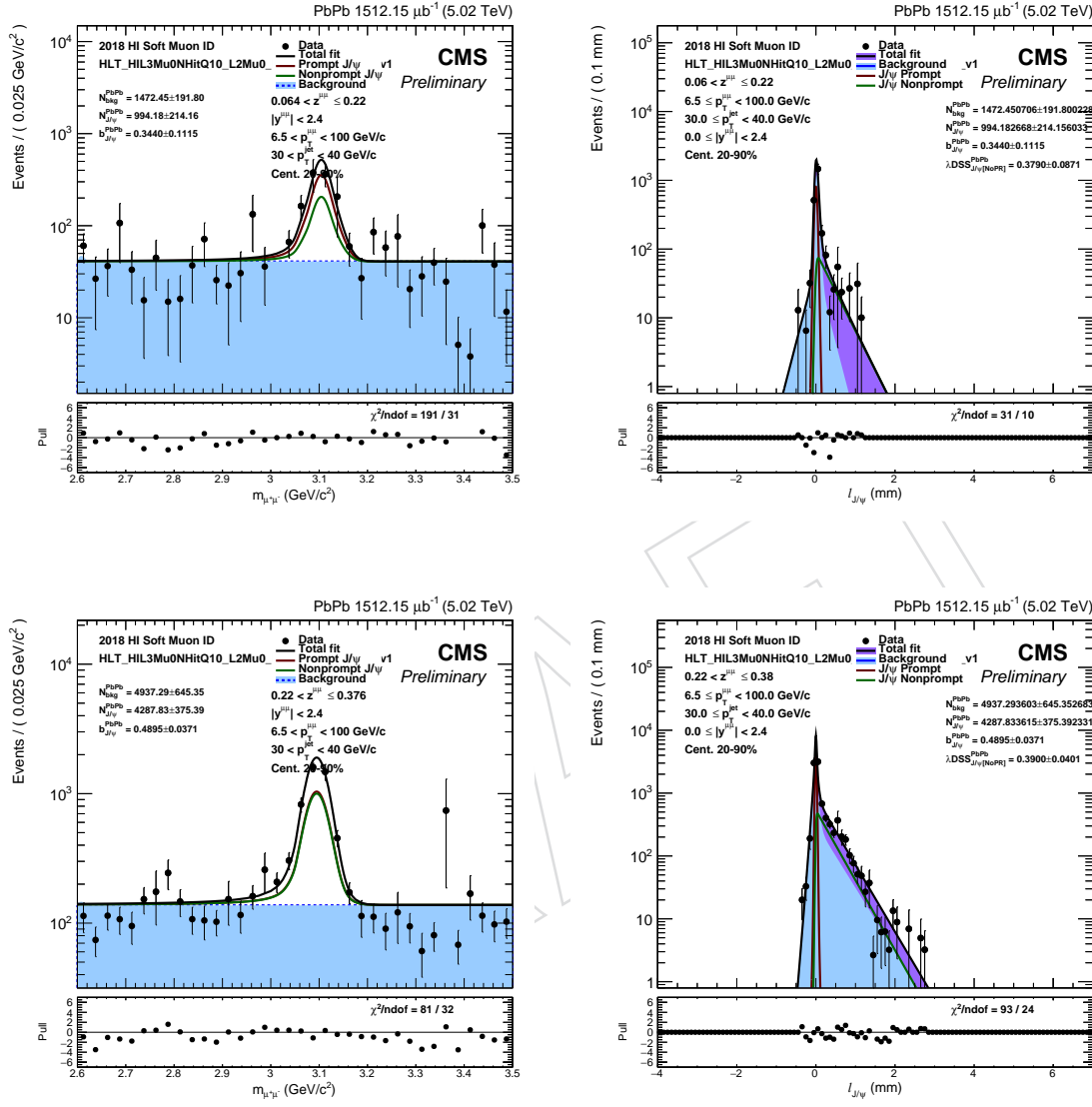


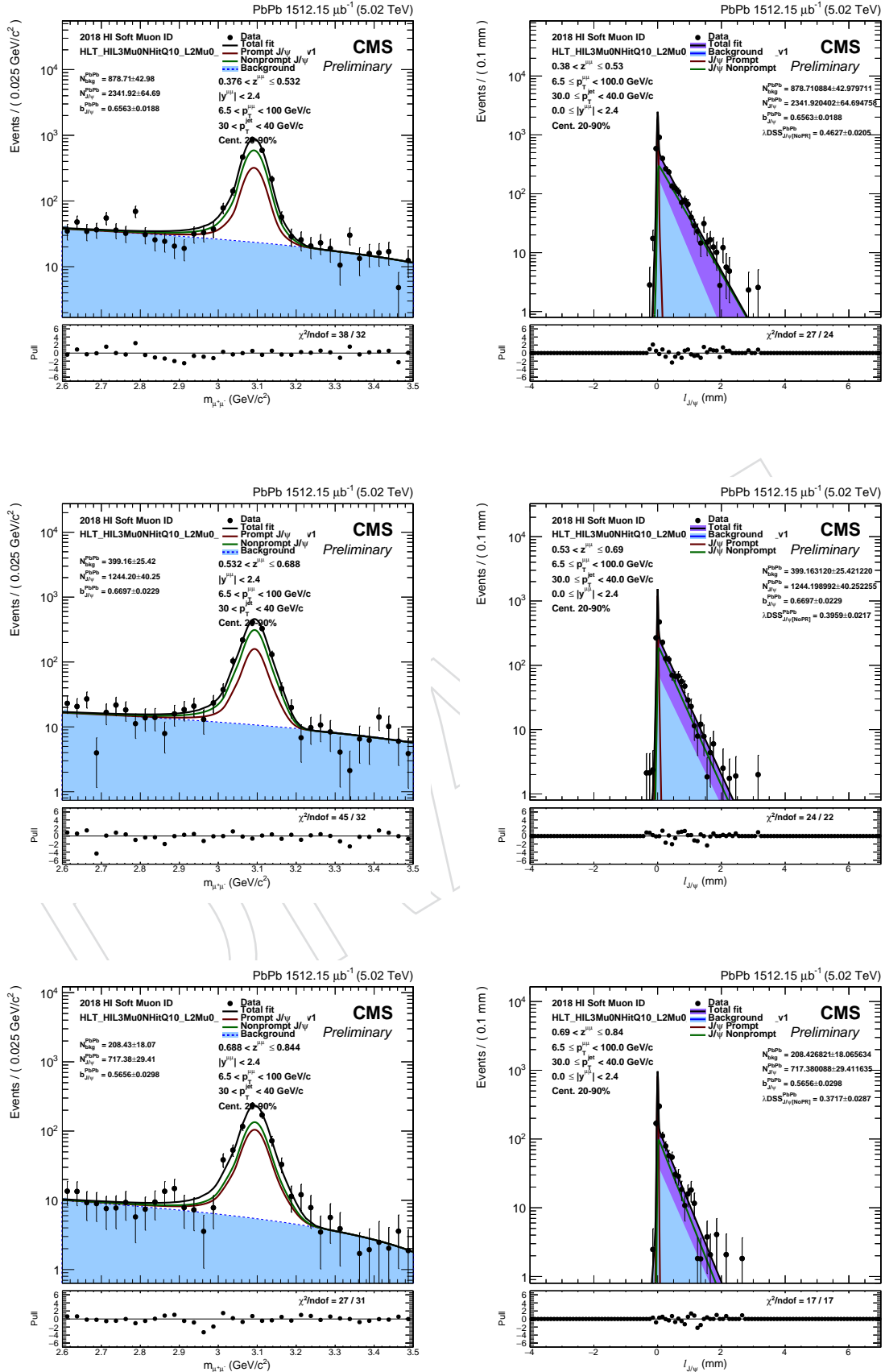


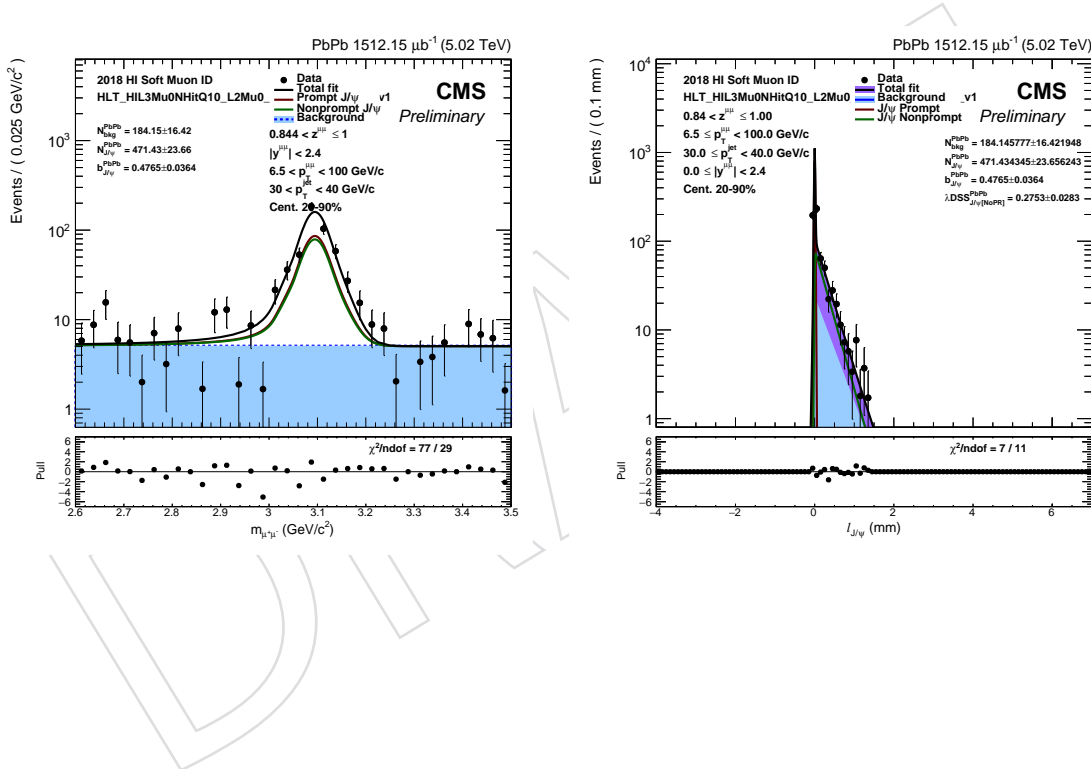
1057 **Fits for jets with $30 < p_T < 40 \text{ GeV}$**

1058 **B.0.17 PbPb**

1059 The projections of the 2D fits in all z bins in PbPb collisions for $30 < p_T(\text{jet}) < 40 \text{ GeV}$, for the
1060 20-90% centrality selection.



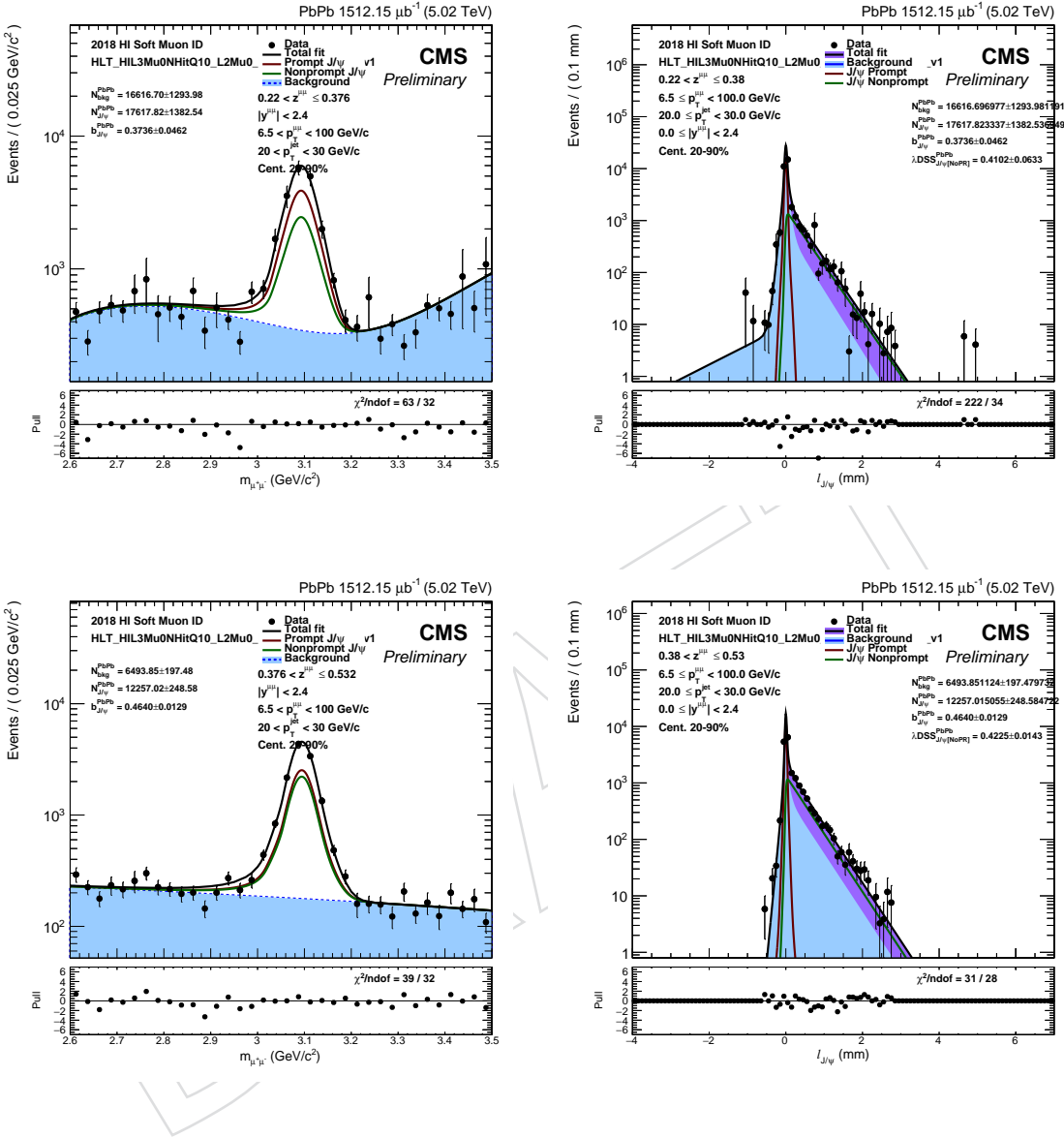


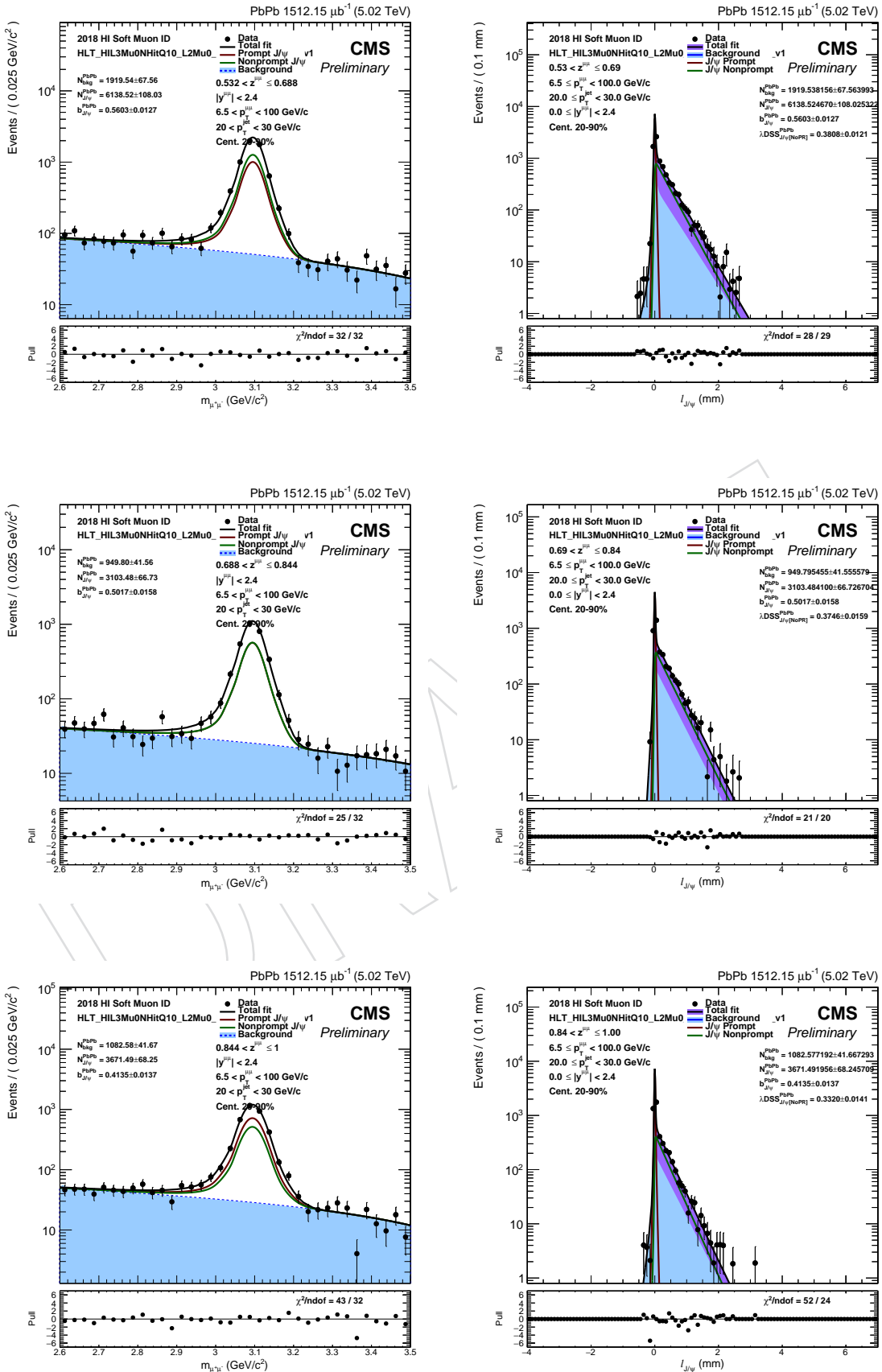


1061 **Fits for jets with $20 < p_T < 30 \text{ GeV}$**

1062 **B.0.18 PbPb**

1063 The projections of the 2D fits in all z bins in PbPb collisions for $20 < p_T(\text{jet}) < 30 \text{ GeV}$.

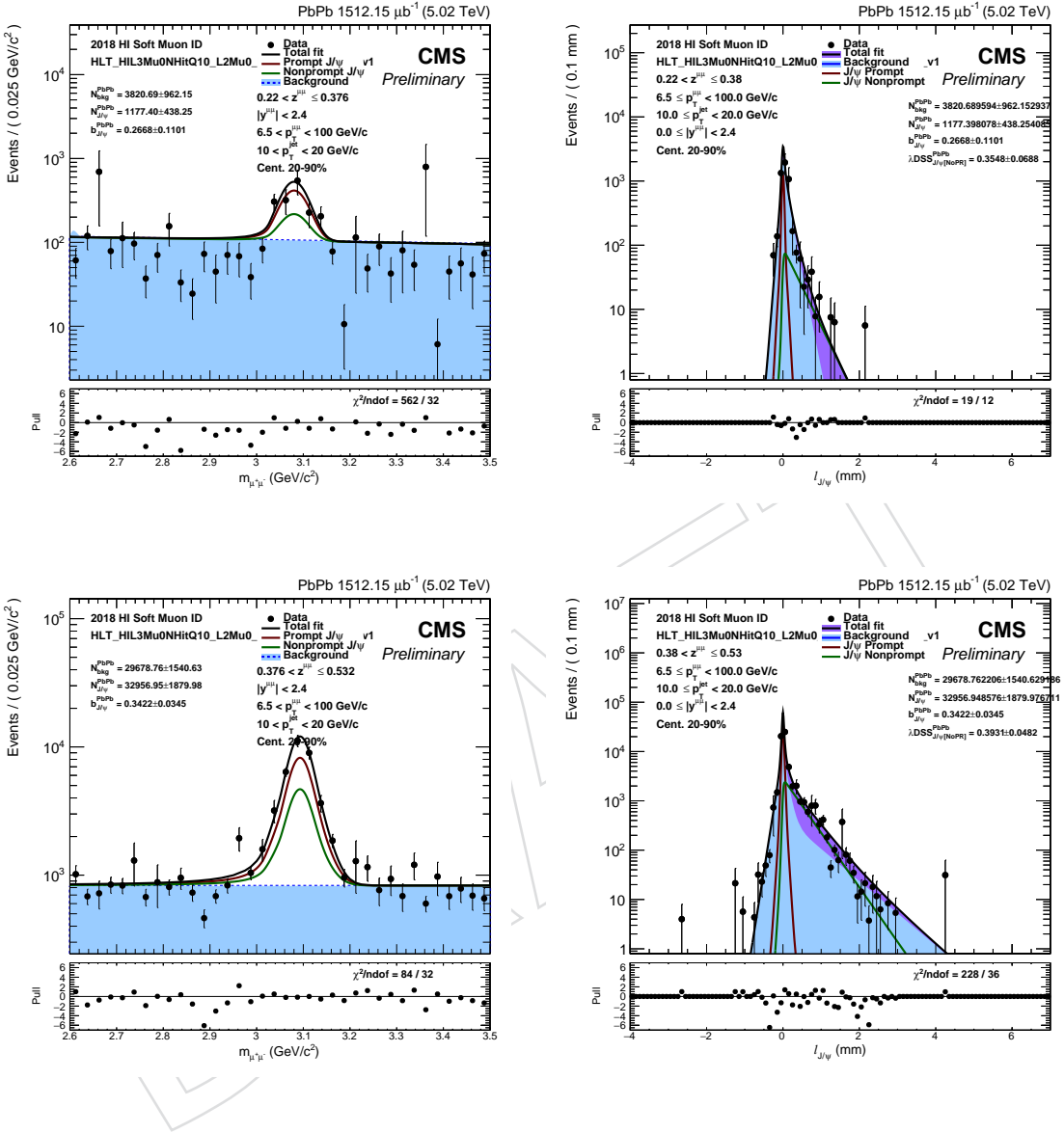


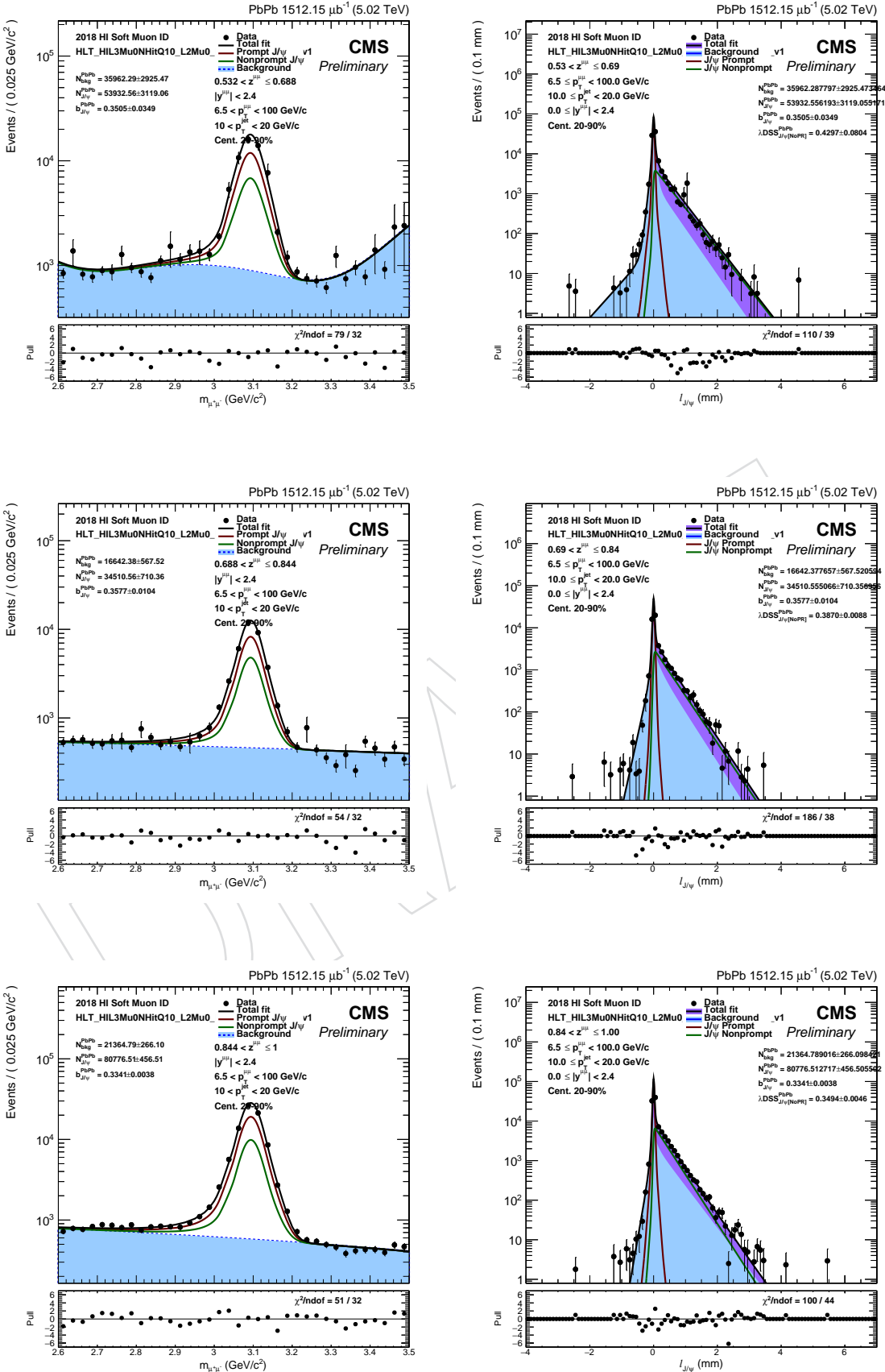


1064 **Fits for jets with $10 < p_T < 20 \text{ GeV}$**

1065 **B.0.19 PbPb**

1066 The projections of the 2D fits in all z bins in PbPb collisions for $10 < p_T(\text{jet}) < 20 \text{ GeV}$.

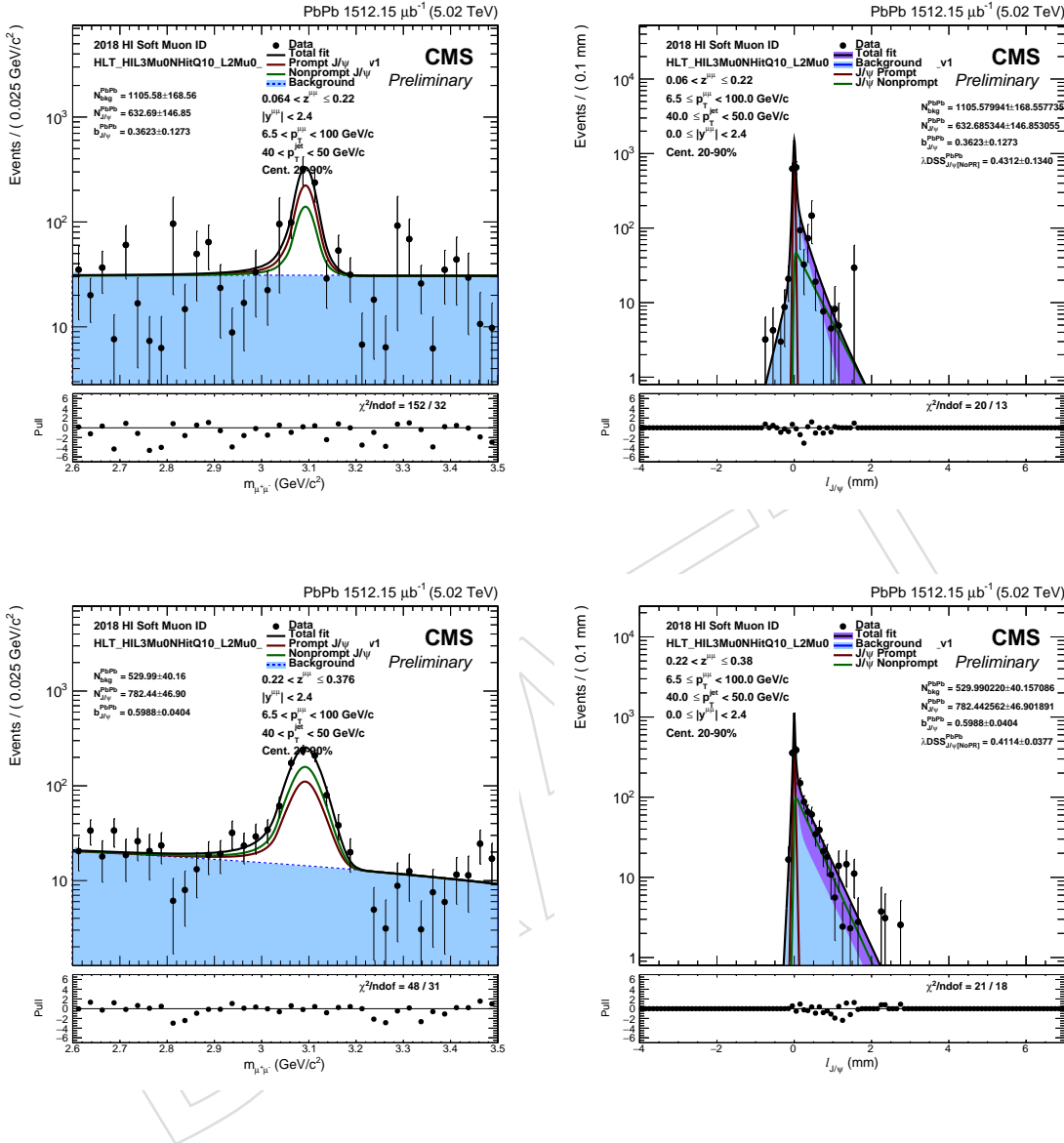


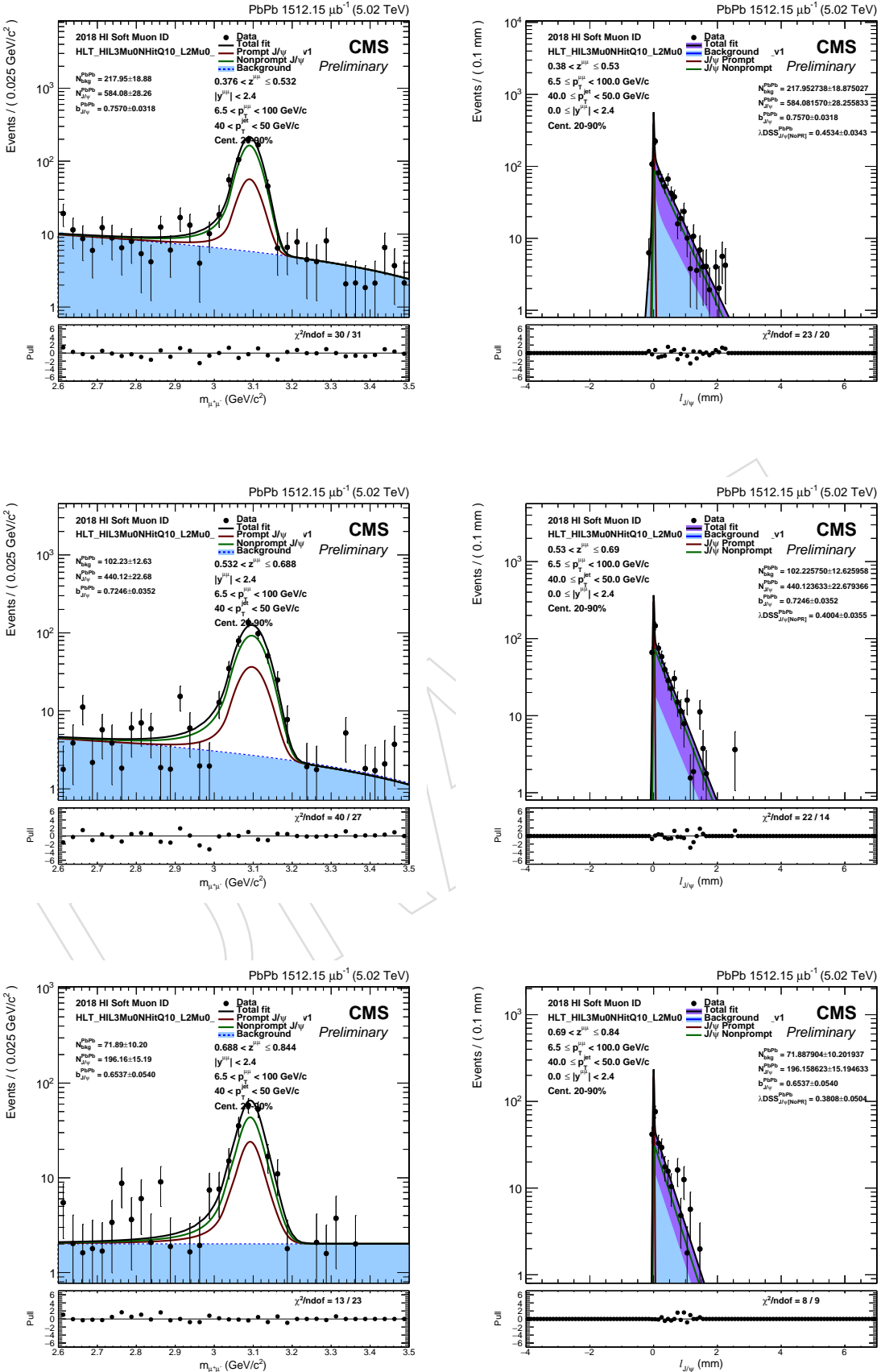


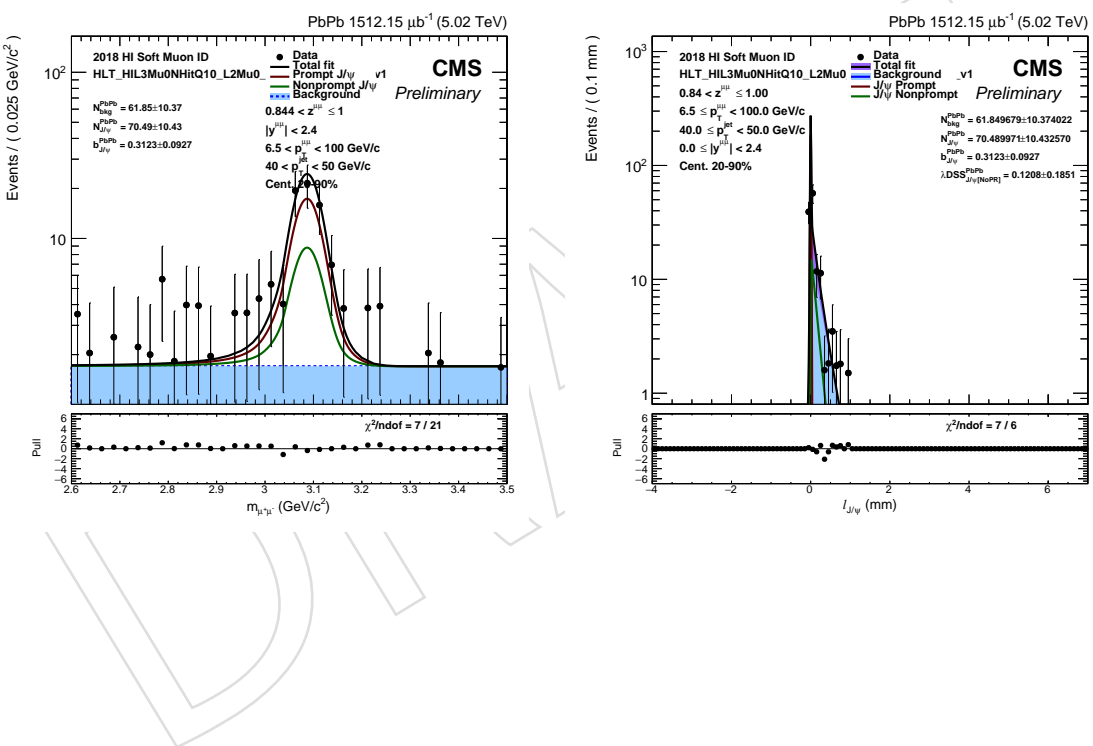
1067 **Fits for jets with $40 < p_T < 50 \text{ GeV}$**

1068 **B.0.20 PbPb**

1069 The projections of the 2D fits in all z bins in PbPb collisions for $40 < p_T(\text{jet}) < 50 \text{ GeV}$.







1070 **Fits for jets with $50 < p_T < 60 \text{ GeV}$**

1071 **B.0.21 PbPb**

1072 The projections of the 2D fits in all z bins in PbPb collisions for $50 < p_T(\text{jet}) < 60 \text{ GeV}$.

